

QUANTIFICATION OF PICOMETER- TO
ÅNGSTRÖM-SCALE ATOMIC DISPLACEMENTS
IN CRYSTALS, FROM QUANTUM DOTS TO BULK
SOLIDS

A Dissertation

Presented to the Faculty of the Graduate School
of Cornell University

in Partial Fulfillment of the Requirements for the Degree of
Doctor of Philosophy

by

Michelle Anne Smeaton

December 2022

© 2022 Michelle Anne Smeaton
ALL RIGHTS RESERVED

QUANTIFICATION OF PICOMETER- TO ÅNGSTRÖM-SCALE ATOMIC
DISPLACEMENTS IN CRYSTALS, FROM QUANTUM DOTS TO BULK
SOLIDS

Michelle Anne Smeaton, Ph.D.

Cornell University 2022

Highly localized structural and spectroscopic measurements using scanning transmission electron microscopy (STEM) enable the exploration of atomic displacements in systems with nanoscale heterogeneity across a wide variety of materials. Further, they allow for the investigation of connections between charge, spin, lattice, and orbital degrees of freedom. These insights can have significant implications for materials design and performance. In this work, precise atomic position measurements are used in combination with diffraction- and spectroscopy-based STEM modalities to investigate atomic displacements in materials from quantum dots to thin films and bulk crystals.

First, strain defects in epitaxially connected quantum dot superlattices are elucidated using a newly developed strain mapping technique. These measurements reveal distinct defect types present in inter-dot connections. The strain defects are then tracked as they evolve during *in situ* annealing in the STEM, providing insights into the relative energetics of the strain defects and suggesting design rules for improving the processing and final electronic properties of the superlattices.

The precise measurement of atomic column positions by atom tracking in high-angle annular dark-field (HAADF)-STEM imaging is becoming more common due to the availability and effectiveness of aberration correction. This tech-

nique holds enormous potential with respect to the study of the physics underlying quantum phenomena. However, the strong channeling behavior of the STEM probe as it propagates along atomic columns can lead to unexpected contrast that influences atomic position measurements. One of these effects, produced by coherently displaced anions in shared cation-anion columns, is shown experimentally to cause measured cation positions to appear displaced by several picometers from their true positions. The origins of this effect and its dependence on experimental parameters are examined through multislice simulations, and strategies for avoiding or minimizing the effect are discussed.

Oxygen deficient $\text{LaNiO}_{3-\delta}$ is presented as a case study for quantifying atomic displacements in a sample containing coherently displaced anions with the potential to induce anomalous atomic position measurements. First, vacancy-ordered oxygen deficient domains are mapped in a bulk crystal using 4D-STEM. The displacement patterns associated with two distinct vacancy-ordered phases are then extracted through careful Fourier analysis, confirming a previously reported structure model for one phase and identifying the lattice distortions in the second phase for the first time.

Finally, a new Jahn-Teller distorted infinite-layer structure is discussed for which careful atomic position measurements were instrumental in determining the structure. Here, the low sample volume and large available phase space prevented a traditional structure refinement by x-ray scattering. Instead, HAADF- and annular bright-field (ABF)-STEM imaging of multiple zone axes were used to first reduce the phase space for an x-ray refinement and then to deduce the true structure from multiple possible refinements. These measurements reveal a complex and highly distorted structure dictated by competition between the two-dimensional Jahn-Teller effect and geometric frustration induced by cou-

pling between atomic layers. Electron energy loss spectroscopy is used to further probe the electronic structure of the material.

BIOGRAPHICAL SKETCH

Michelle A. Smeaton was born to Lynda and Scott Smeaton and has two younger brothers, Steve and Dan. She grew up in the suburbs of Minneapolis, Minnesota, where her parents fostered in her a love of science and learning. Michelle followed in her parents footsteps and attended the University of Minnesota, where she studied materials science and engineering. During her first semester, she was introduced to the study of nanomaterials and subsequently joined the research group of Professor Eray Aydil, where she studied the synthesis and properties of nanocrystal thin films for renewable energy applications. She received her Bachelor of Science *summa cum laude* with distinction in 2017. That fall she moved to Cornell University to begin her graduate work in the Department of Materials Science and Engineering and joined Professor Lena Kourkoutis' electron microscopy group. She earned her Master of Science in 2020 and her PhD in the fall of 2022.

ACKNOWLEDGEMENTS

There are many people without whom this work would not have been possible. First of all, I want to thank my advisor, Lena Kourkoutis for supporting me through the years of my PhD. With her guidance I was able to explore a wide variety of compelling material systems and find a place for myself in the exciting field of electron microscopy. I would also like to thank Tobias Hanrath and Andrej Singer for serving on my special committee.

Along with the variety of material systems, I've had the pleasure of working with the many excellent collaborators who grew them. Thank you to Tobias Hanrath and his group members Jessica Cimada daSilva, Daniel Balazs, and Tyler Dunbar for their patience and willingness to prepare so many quantum dot samples. Thank you to John Mitchell and Hong Zheng at Argonne National Lab for providing excellent bulk crystalline samples of lanthanum nickelates. Thank you to Harold Hwang and his group member Woojin Kim at Stanford University for the many beautiful cobaltate films and for their willingness to coordinate on logistically difficult experiments. Though their work is not discussed at length in this thesis, thank you also to Darrell Scholm and his group members Felix Hensling and Jake Sun, Rich Robinson and his group member Anuj Bhargava, and Bharat Jalan and his group member Fengdeng Liu.

Many thanks go to John Grazul, Mariena Silvestry-Ramos, Katie Spoth, and Mick Thomas who kept all the microscopes in top working condition and who were so responsive to my many troubleshooting questions. Their guidance and insights were invaluable.

I also want to thank all the members of the KEM group past and current for their fruitful discussions, advice and camaraderie: David Baek, Michael Zachman, Ben Savitzky, Jade Noble, Katie Spoth, Ismail El Baggari, Berit Goodge,

Yue Yu, Noah Schnitzer, Mike Colletta, Danielle Markovich, and Lopa Bhatt. Thank you also to the wonderful members of my MSE cohort. My time at Cornell was much more joyful and warm thanks to you friendship and support.

Finally, I want to thank my parents for their unconditional love and support. Although they were skeptical when I first told them I wanted to stay in school to pursue a PhD, they supported me every step of the way. I'm forever grateful to them. And to Nick: I can't wait to see what our next adventure holds.

TABLE OF CONTENTS

Biographical Sketch	iii
Acknowledgements	iv
Table of Contents	vi
List of Tables	viii
List of Figures	ix
1 Introduction	1
1.1 Scanning Transmission Electron Microscopy: Principles and Selected Techniques	1
1.1.1 HAADF- and ABF-STEM imaging	4
1.1.2 4D-STEM	6
1.1.3 Spectroscopy	9
1.1.4 <i>In situ</i> temperature control	17
1.2 Thesis outline	19
2 Mapping Defect Relaxation in Quantum Dot Solids upon <i>In Situ</i> Heating	21
2.1 Background	21
2.2 Results and discussion	23
2.3 Conclusions	40
2.4 Methods	41
2.4.1 Strain mapping	42
3 Influence of light atoms on atom tracking of cations in distorted perovskites with ADF-STEM	47
3.1 Background and theory	47
3.2 Results and discussion	48
3.3 Methods	60
3.3.1 Atomic displacement mapping	60
3.3.2 Multislice simulations	61
4 Disentangling the Structure of Oxygen Vacancy Ordered Domains in $\text{LaNiO}_{3-\delta}$	63
4.1 Background	63
4.2 Results and discussion	64
4.3 Methods	70
4.3.1 EWPC filtering	71
5 Structure determination of a new, highly distorted infinite-layer phase	73
5.1 Background	73
5.2 Results and discussion	74
5.3 Methods	88
5.3.1 Thin film synthesis and characterization	88

5.3.2	Cross-section and plan-view FIB lamella preparation . . .	88
5.3.3	STEM and EELS measurements	90
5.3.4	Estimation of oxygen positions	92
5.3.5	Multislice simulations	92
	Bibliography	93

LIST OF TABLES

5.1	Atomic coordinates for cations in CaCoO_2 measured from cross-sectional HAADF-STEM imaging.	79
5.2	Atomic coordinates for the initial (symmetry-based) structure model and final refined structure of CaCoO_2	84

LIST OF FIGURES

1.1	STEM schematic and atomic-resolution imaging of heavy and light atoms using HAADF and ABF detectors.	3
1.2	4D-STEM analysis of a monolayer PbSe quantum dot superlattice. A 4D-STEM detector collects a 2D diffraction pattern for every scan position in a 2D array, leading to incredibly information-rich datasets.	7
1.3	STEM-EELS elemental mapping of an Fe ₃ O ₄ /MnFe ₂ O ₄ core/shell nanocrystal.	10
1.4	Atomic-resolution elemental STEM-EDX mapping of a Sn-doped Ba ₃ In ₂ O ₆ thin film.	11
1.5	EEL spectra and atomic-resolution elemental maps of a CaSnO ₃ /GdScO ₃ interface.	13
1.6	O-K edge ELNES analysis of CaCoO _{2.5} and CaCoO ₂ thin films and a SrTiO ₃ substrate.	15
2.1	Examples of local heating effects in an epitaxially connected square superlattice of PbSe QDs.	24
2.2	Examples of tensile, shear, and bending strain states in necks between QDs.	27
2.3	Evolution of tensile, shear, and bending strain states upon <i>in situ</i> heating.	30
2.4	Evolution of strain states upon <i>in situ</i> heating in the orthogonal lattice vector over the same field of view.	32
2.5	Strain states and heating effects tracked over a large field of view.	33
2.6	Strain states and heating effects tracked over a large field of view in the orthogonal lattice vector.	34
2.7	Examples of dislocation formation upon <i>in situ</i> heating.	35
2.8	Companion to Fig. 2.7 showing strain maps for the orthogonal lattice vector.	37
2.9	Tracking the out-of-plane orientation of QDs in a QDS film upon <i>in situ</i> heating.	38
2.10	Workflow for the sine wave fitting method for strain mapping.	43
2.11	Representative examples of error in amplitude, tensile strain, and lattice rotation values extracted using the sine wave fitting method.	45
3.1	Atom tracking in HAADF-STEM imaging of the [110] _{pc} zone axis of LaNiO ₃ , showing a consistent displacement patterning with ~ 3.7 pm displacements.	49
3.2	Probe intensity and HAADF-STEM image simulations for the [110] _{pc} zone axis of LaNiO ₃	51
3.3	Probe intensity simulations for three probe positions around the shared lanthanum-oxygen columns.	52

3.4	Examples of $a^0a^0c^+$ and $a^0a^0c^-$ tilt systems in perspective view as well as projected down their $[001]_{pc}$ and $[101]_{pc}$ zone axes.	55
3.5	Experimental and simulated HAADF-STEM data showing the magnitude of the channeling artifact is less severe at an accelerating voltage of 300 kV.	56
3.6	Probe intensity simulations for a 60 kV probe showing anomalous behaviour for thick samples due to multiple scattering effects.	58
4.1	Vacancy ordering and summed NBED patterns for the $\delta = 0.5$ and 0.25 phases of $\text{LaNiO}_{3-\delta}$	65
4.2	Domain mapping of the $\delta = 0.5$ and 0.25 phases of $\text{LaNiO}_{3-\delta}$ with 4D-STEM.	67
4.3	Atomic column displacements mapped for lanthanum sites along the $[\bar{1}10]_{pc}$ projection of $\text{LaNiO}_{3-\delta}$	68
5.1	Synthesis and XRD of CaCoO_2 and $\text{CaCoO}_{2.5}$ thin films.	76
5.2	Estimation of the Co valence states in CaCoO_2 and $\text{CaCoO}_{2.5}$ thin films from the Co- $L_{2,3}$ EELS edge using the white line ratio.	77
5.3	Cross-sectional HAADF-STEM imaging and measured cation model of CaCoO_2 thin films.	78
5.4	Prospective structure models for CaCoO_2	80
5.5	Experimental and simulated cross-sectional ABF-STEM imaging of $[110]_t$ -oriented CaCoO_2	81
5.6	Plan-view HAADF- and ABF-STEM imaging of CaCoO_2 films and final refined structure model.	82
5.7	Larger field-of-view plan-view HAADF-STEM image of CaCoO_2	83
5.8	Jahn-Teller effect and geometric frustration in the CaCoO_2 lattice.	85
5.9	EELS analysis of the O-K and Ca- $L_{2,3}$ edges of $\text{CaCoO}_{2.5}$ and CaCoO_2 thin films.	86
5.10	Unfiltered O-K edge EEL spectra.	87
5.11	Plan-view FIB lamella preparation.	90

CHAPTER 1

INTRODUCTION

1.1 Scanning Transmission Electron Microscopy: Principles and Selected Techniques

Scanning transmission electron microscopy (STEM) has become an enormously useful tool in the field of materials science. It can provide an abundance of information relating not only to structure and symmetry, but also to elemental composition, chemical bonding and magnetic structure. STEM works analogously to traditional light microscopes, but while the resolution of light microscopes is diffraction-limited to a couple hundred nanometers by the wavelength of light, the diffraction-limited resolution of electron microscopes is tunable by the electron energy and can therefore theoretically reach the picometer length-scale. Unfortunately for scientists, a number of other limitations come into play before that limit can be reached. Nonetheless, modern STEM instruments can routinely reach sub-ångström resolution [11, 107, 92] and near-picometer precision [160].

STEM enables unique measurements of materials due not only to its high spatial resolution, but also its flexible sample preparation techniques and moderately high energy resolution for spectroscopy. In comparison to other state-of-the-art microscopy techniques such as scanning tunneling microscopy and atomic force microscopy, which require an extremely clean sample surface and are only sensitive to a thin surface layer, STEM specimens can be prepared in multiple geometries including plan-view and cross-section for analysis of

buried interfaces and defect structures. It is also a projection technique, meaning that the electron beam interacts with the full thickness of the sample as it is transmitted through. While the latter point can be beneficial for extracting information from the full volume of a sample, for example in studying buried planar defects in thin film heterostructures [5] or core/shell structures in nanoparticles [16], it can also obfuscate results and necessitates judicious interpretation. The ability of STEM to probe the full sample volume without sacrificing atomic-scale spatial resolution is also a significant benefit over other sensitive spectroscopic techniques such as x-ray absorption spectroscopy (XAS), x-ray photoelectron spectroscopy (XPS), and angle-resolved photoemission spectroscopy (ARPES).

As mentioned above, a transmission electron microscope functions analogously to a light microscope: the beam is produced by an electron gun and subsequently focused by a series of lenses (now electromagnetic lenses as opposed to glass lenses) onto a sample. It is transmitted through the sample, undergoing several elastic and inelastic scattering processes, and is collected by detectors on the other side. This basic principle of STEM is illustrated schematically in Figure 1.1a. While electromagnetic lenses have come a long way from their first demonstration in an electron microscope in the 1930s, they function imperfectly, leading to the introduction of aberrations to the electron beam. These aberrations, including spherical aberration, astigmatism, coma, etc., limit the spatial resolution of the microscope. Aberration correctors seek to compensate for the inherent beam aberrations through careful tuning of a series of quadrupolar, hexapolar and/or octupolar lenses. In STEM, the tuned beam is focused to a point on the sample and rastered across the sample surface, and the transmitted electrons are collected for each scan position.

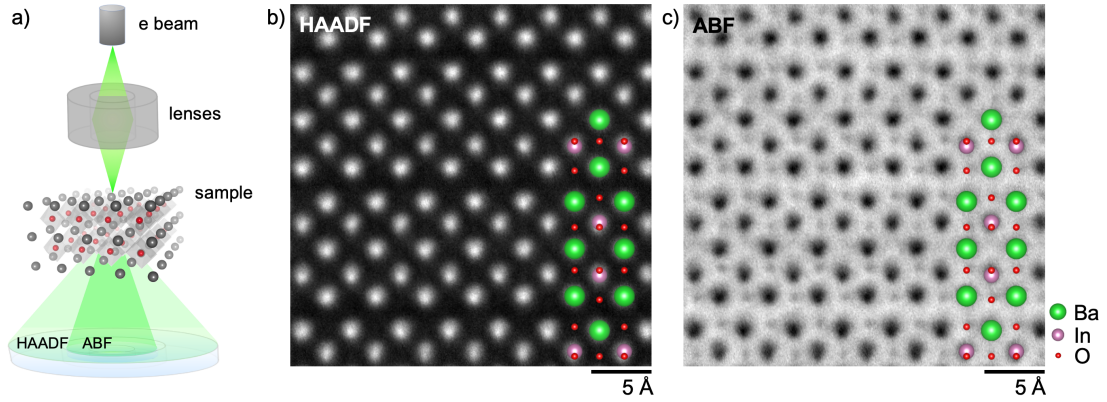


Figure 1.1: STEM schematic and atomic-resolution imaging of heavy and light atoms using HAADF and ABF detectors. (a) Schematic illustration of a STEM probe used to image a thin crystalline sample. Two annular detectors are depicted below the sample. (b) HAADF- and (c) ABF-STEM image of a Ruddlesden-Popper $\text{Ba}_3\text{In}_2\text{O}_6$ thin film. HAADF imaging produces directly interpretable atomic number (Z) contrast, while ABF imaging is more sensitive to light elements such as the oxygen atoms visible in c.

The incident beam interacts with the sample by two main classes of scattering mechanisms: elastic and inelastic. Elastically scattered electrons are primarily used to extract structure and symmetry information, while inelastically scattered electrons provide chemical and bonding information about the sample. Several different geometries and types of detectors are available, which are sensitive to distinct scattering mechanisms and therefore allow for different types of quantitative measurements. Often, multiple signals can be detected simultaneously, increasing the efficiency of measurements. The following sections will discuss the function and applications of the detectors and associated techniques that are used throughout the work presented here.

1.1.1 HAADF- and ABF-STEM imaging

Most commonly, STEM imaging is performed with annular detectors. These detectors integrate transmitted electrons over a user-defined range of collection angles at each scan position. The chosen collection angle range dictates the contrast mechanisms in the resulting image and the associated sensitivity to different elements. High-angle annular dark-field (HAADF) imaging, as its name suggests, integrates over high scattering angles (usually $> 3\times$ the convergence angle of the incident probe), and produces image contrast that scales with atomic number (Z) as $Z^{\sim 1.7}$ [78, 143]. It is therefore most sensitive to heavy elements. An example HAADF-STEM image of a $\text{Ba}_3\text{In}_2\text{O}_6$ thin film is presented in Figure 1.1b. Since Ba ($Z = 56$) and In ($Z = 49$) are fairly close in atomic number, there is very little difference in contrast between atomic columns in this case. It is clear, however, that the light, oxygen atomic columns are not visible. Since HAADF imaging is dominated by Z contrast, it can be used to precisely quantify the positions of atomic columns in a crystal down to the picometer scale [9, 132]. This is especially useful in the study of quantum materials, where subtle, local heterogeneity in atomic structure can dictate materials properties.

Figure 1.1c shows an image acquired simultaneously to that in Figure 1.1b by integrating over a different range of collection angles to produce an annular bright-field (ABF) image. In this imaging modality the contrast is inverted, with atomic columns appearing dark on a light background. To form an ABF image, the transmitted electrons are integrated over an annular detector that sits within the limits of the bright disk (i.e., it is integrated from approximately one half the incident beam convergence angle up to, but not exceeding, the convergence angle). The resulting images display both heavy and light elements, as shown

in Figure 1.1c. While ABF contrast is more sensitive to variations in thickness, sample tilt, and probe defocus than HAADF contrast, it is more directly interpretable than traditional bright-field imaging with a solid disk detector [40]. It can therefore be used, for example, to measure the evolution of oxygen octahedral tilts across perovskite oxide heterointerfaces, which have important implications for the properties of oxide heterostructures [6]. More detailed discussion of the effects of various imaging parameters on ABF contrast can be found in the following references [62, 110].

Regardless of the detector and collection angles chosen, any STEM image may be affected by scan artifacts. These could be caused by thermal drift of the stage, mechanical vibrations, electrical noise in the scan coils, etc. To minimize artifacts due to stage instability, it is often useful to acquire many frames of the same field of view at a fast scan rate and subsequently align and sum the frames to obtain a high signal-to-noise ratio (SNR) image. The Kourkoutis group has previously developed a method for rigid registration of low SNR image frames by cross correlation of every frame with every other frame in an image stack. This strategy minimizes the risk of so-called unit cell hops during cross correlation of low SNR frames of periodic lattices. More information on the technique can be found in the original publication [133] and in the doctoral thesis of Savitzky [131]. Minimizing artifacts caused by thermal instability is particularly important for *in situ* temperature-controlled experiments as will be discussed briefly in Section 1.1.4.

1.1.2 4D-STEM

While the conventional STEM detectors discussed up to this point record a single intensity value for each scan position, a relatively new technique, referred to as 4D-STEM, collects the entire 2D convergent beam electron diffraction pattern for each scan position. It can therefore be used to extract a wide range of sample characteristics including local phase [136, 20], orientation [30, 41], strain [57, 116], medium range order [66], and electromagnetic fields [54, 73]. It can even be used to reconstruct the full complex sample potential in a technique called ptychography [121, 154, 36, 91]. This technique was recently used to achieve the record spatial resolution of < 20 pm in a PrScO_3 crystal, limited by the thermal vibrations of the atoms [26].

The rise in popularity of 4D-STEM has been linked to the development of high-efficiency direct electron detectors that enable the technique. These detectors are advantageous for 4D-STEM experiments due to their high detective quantum efficiency (DQE) and high SNR compared to scintillator-based detectors. More conventional CCD cameras are relatively ill-suited as they have limited readout speed and low dynamic range. There are currently two types of 4D-STEM detectors on the market, each with distinct benefits and drawbacks. Hybrid pixelated detectors (PADs) exhibit fast readout speeds and high dynamic range, which allows features within the bright disk of the scattered beam to be resolved at the same time as dim features at high scattering angles [24, 141]. These detectors currently contain limited numbers of pixels, however. Monolithic active pixel sensor (MAPS) detectors are able to accommodate a larger number of pixels with good readout time, but have low dynamic range due to the lower per-pixel saturation value [96, 39, 34].

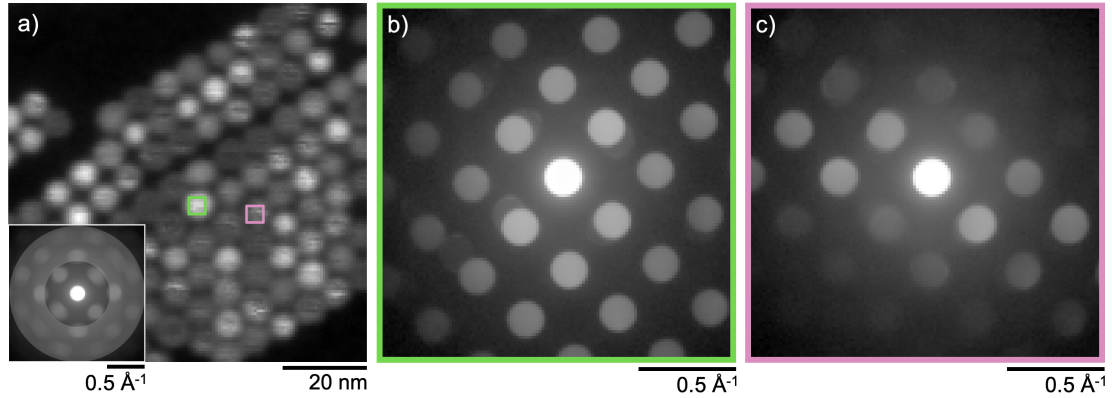


Figure 1.2: 4D-STEM analysis of a monolayer PbSe quantum dot superlattice. A 4D-STEM detector collects a 2D diffraction pattern for every scan position in a 2D array, leading to incredibly information-rich datasets. (a) A "virtual" ADF image calculated by summing the intensity at each scan position over a virtual annular detector in diffraction space. The diffraction pattern summed over all scan positions is shown in the inset with the virtual detector overlaid. (b,c) Diffraction patterns summed over the regions indicated by green (b) and pink (c) boxes in a. The summed diffraction patterns for each quantum dot (QD) were used to identify their out-of-plane orientations [30].

Figure 1.2 shows an example of a 4D-STEM dataset used to identify the out-of-plane orientation of each quantum dot (QD) in a monolayer assembly [30]. Panel a of Figure 1.2 shows a "virtual" ADF image calculated by summing the collected intensity over an annular detector overlaid on the 2D diffraction pattern for each scan position. This method can be used to form "virtual" images for any arbitrarily defined detector geometry, including traditional STEM detector geometries like bright field (BF), ABF, and ADF. The diffraction pattern summed over all scan pixels is inlaid in Figure 1.2a. Figure 1.2 b and c show the diffraction patterns summed over 7×7 pixels for each of two QDs noted by green and pink boxes in panel a. In order to extract the orientation of each QD, their diffraction patterns were matched to a library of simulated diffraction patterns covering a wide range of orientations using a template matching algorithm. Note that the experimental parameters here were chosen to ensure that the Bragg disks were separated in the diffraction plane. This is necessary

for many types of 4D-STEM analysis including orientation mapping (as shown here) and strain mapping. The extent of separation of Bragg disks is a function of both the crystal lattice of the sample and the convergence angle of the incident probe. As the convergence angle is inversely related to the size of the STEM probe (and therefore the achievable spatial resolution), it is important to consider the trade-off between the two when planning a 4D-STEM experiment. This can be a significant limitation in experiments where high spatial resolution (unit cell level or better) is required, for example in strain mapping of epitaxially connected quantum dot superlattices as discussed in Chapter 2.

Analysis of 4D-STEM data is often complicated due to the volume of data and the density of information contained therein. Furthermore, measurements can be skewed by the myriad factors influencing the the diffracted beam intensities, including thickness variations, crystal tilt, and multiple scattering effects (dynamical diffraction). As the technique grows in popularity, computational approaches are being actively developed to make analysis of 4D-STEM data more robust and streamlined [135, 116, 164, 21]. One method recently developed to reduce the effects of sample mistilt and thickness variation on Bragg disk intensity is the exit wave power cepstrum (EWPC) [116], which will be discussed in Chapter 4. For further discussion of the wide variety measurements possible with 4D-STEM, the reader is referred to a useful review provided by Ophus [114].

1.1.3 Spectroscopy

Beyond structural information from direct imaging or diffraction methods, STEM can provide a wealth of chemical and bonding information from inelastic interactions between the incident beam and bound electrons in the sample. There are two primary techniques used to measure these interactions: electron energy loss spectroscopy (EELS) and energy dispersive x-ray spectroscopy (EDX or EDS). Both techniques probe nominally the same scattering mechanism, wherein an incident electron excites a bound electron in the sample into an unoccupied state above the Fermi level. EELS measures the energy lost by the incident electron by dispersing the transmitted beam with a magnetic lens onto a detector. EDX detects the energies of x-rays that are emitted as the excited electron relaxes back into the lower energy state. Both techniques therefore produce signals characteristic of particular elements and electronic transitions. In combination with the scanned, sub-ångström probe, these characteristic signals can then be used to map and quantify elemental composition from the micron- or nano-scale (for example in nanocrystals as shown in Figure 1.3) down to the atomic-scale as in Figure 1.4.

It is important, when measuring composition of a sample, to consider its 3D structure, since the signal for a given probe position is collected from the full projected thickness at that position. This is exemplified by line profiles (Figure 1.3c) of the Mn and Fe EELS intensities in an $\text{Fe}_3\text{O}_4/\text{MnFe}_2\text{O}_4$ core/shell nanocrystal taken across the nanocrystal, as indicated by the dashed box overlaid on the elemental map in Figure 1.3b. The Mn intensity does not drop to zero in the middle of the nanocrystal as one might naively expect, because the beam is still passing (and scattering) through layers of MnFe_2O_4 shell on the front and

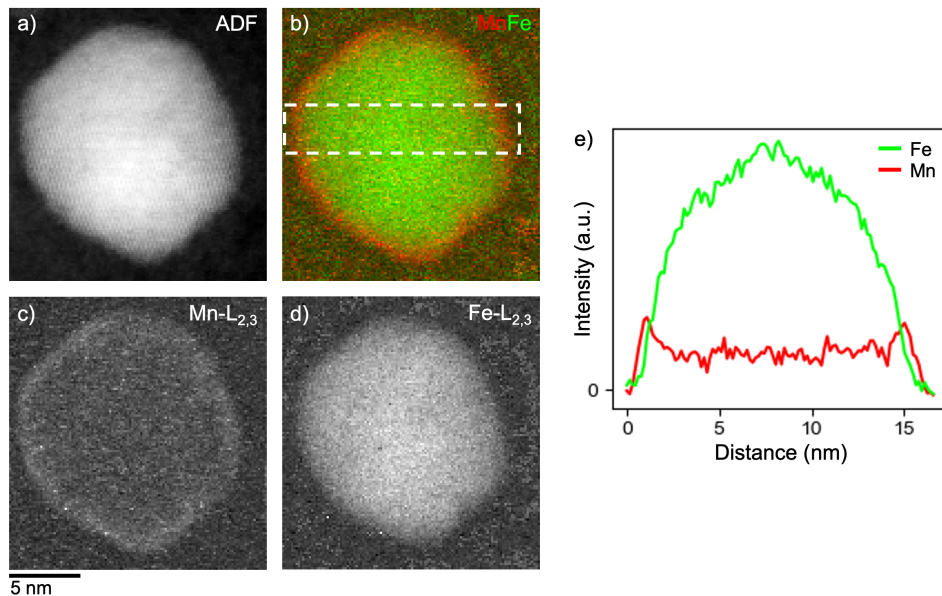


Figure 1.3: STEM-EELS elemental mapping of an $\text{Fe}_3\text{O}_4/\text{MnFe}_2\text{O}_4$ core/shell nanocrystal. (a) Simultaneously acquired ADF-STEM image. (b) False-colored map of the Mn and Fe signals in red and green, respectively. (c,d) Individual elemental maps of the Mn and Fe signals. (e) Line profiles of the Mn and Fe signals from the dashed box indicated in b, clearly showing the Mn/Fe core/shell structure of the nanocrystal. It is important to consider the projection nature of STEM when measuring 3D structures such as this. For example, the Mn signal does not drop to zero in the middle of the nanocrystal, as the beam passes through the MnFe_2O_4 shell on the front and back faces of the nanocrystal along the projection direction. Here, elemental mapping was used to estimate the shell thickness in strained core/shell nanocrystals to assess the effect of strain on Li-ion diffusion in the nanocrystals [15].

back faces of the nanocrystal along the projection axis.

An example of atomic-resolution elemental mapping using EDX is shown in Figure 1.4 for a Sn-doped $\text{Ba}_3\text{In}_2\text{O}_6$ thin film. Panel a presents an ADF image acquired simultaneously with the EDX signal, and panel b shows a false colored map of the elemental signals for Ba, In, and Sn in magenta, cyan, and yellow, respectively. The individual elemental maps are included in Figure 1.4d-f. Here, there was interest in where the Sn dopants were incorporated into the atomic lattice. The vertical line profile in Figure 1.4c shows that the dopants preferentially sit on In sites.

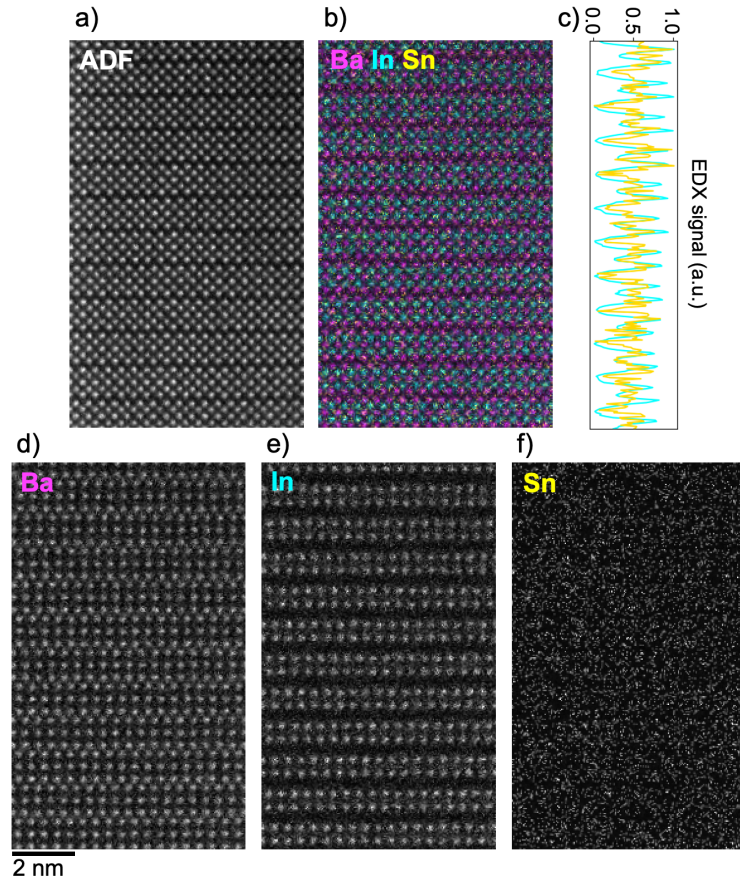


Figure 1.4: Atomic-resolution elemental STEM-EDX mapping of a Sn-doped $\text{Ba}_3\text{In}_2\text{O}_6$ thin film. (a) Simultaneously acquired ADF-STEM image. (b) False-colored map of the Ba, In, and Sn integrated signal intensities in magenta, cyan, and yellow, respectively. (c) Line profiles of the In and Sn signals from b summed horizontally, showing the Sn dopants sit preferentially on In sites. (d-f) Individual elemental maps of Ba, In, and Sn, respectively. The Ba signal was summed over the Ba-L and Ba-K α peaks; the In signal was summed over the In-L $\alpha_{2,1}$, In-K α , and In-K β peaks, and the Sn signal was summed over the Sn-L γ_1 and Sn-K α peaks. Each elemental map was denoised using PCA, subtracting the bottom 5% of components.

While EDX and EELS can both be utilized for atomic-resolution elemental mapping, they have different cross-sections and therefore signal strengths. EDX data can be collected over an enormous energy range (up to tens of keV), while the EELS signal is limited by low scattering cross sections for edges over a couple thousand eV. Recent improvements in EELS detectors have made it possible to access higher energy edges with reasonable signal-to-noise ratio (SNR), but

the range is still significantly lower than that of EDX. On the other hand, the x-ray yield for EDX is relatively low, meaning acquisition times for STEM-EDX maps are much longer than for STEM-EELS maps. This is because x-rays are emitted from the sample isotropically in all directions, and thus the collection efficiency is limited by the solid angle of the detector. Additionally, the x-ray fluorescence yield drops off at low atomic numbers, exacerbating the problem for light elements. The low x-ray yield can be a significant limitation of EDX, particularly for dose-sensitive samples or *in situ* experiments where sample stability is a challenge. Ultimately, both techniques can provide detailed elemental information at the atomic scale, and there are particular use cases where each holds advantages over the other. A more detailed technique comparison can be found in chapter 1.5 of Egerton's textbook: *Electron Energy Loss Spectroscopy in the Electron Microscope* [37]. In addition to elemental mapping, EELS can be used to access local bonding environments and electronic states. As this is the focus of the spectroscopy work presented here, the remainder of this section will focus on EELS analysis.

The EEL spectrum is formed by the unscattered and forward-scattered electrons, dispersed in energy by a magnetic prism and then collected by a detector. It is displayed as the energy lost to the sample by the incident electron. The spectrum comprises two regions: the low-loss region (Figure 1.5a), spanning from 0 eV to ~ 50 eV, and the core-loss region (Figure 1.5b), which refers to energy losses from ~ 50 eV onward. The low-loss region includes the unscattered electrons, or zero-loss peak (ZLP) at 0 eV, phonon and plasmon scattering, and other valence excitation information between 0 and ~ 50 eV. This energy range typically contains many overlapping signals and can thus be challenging to interpret. Low-loss signals are also delocalized over atom sites, which

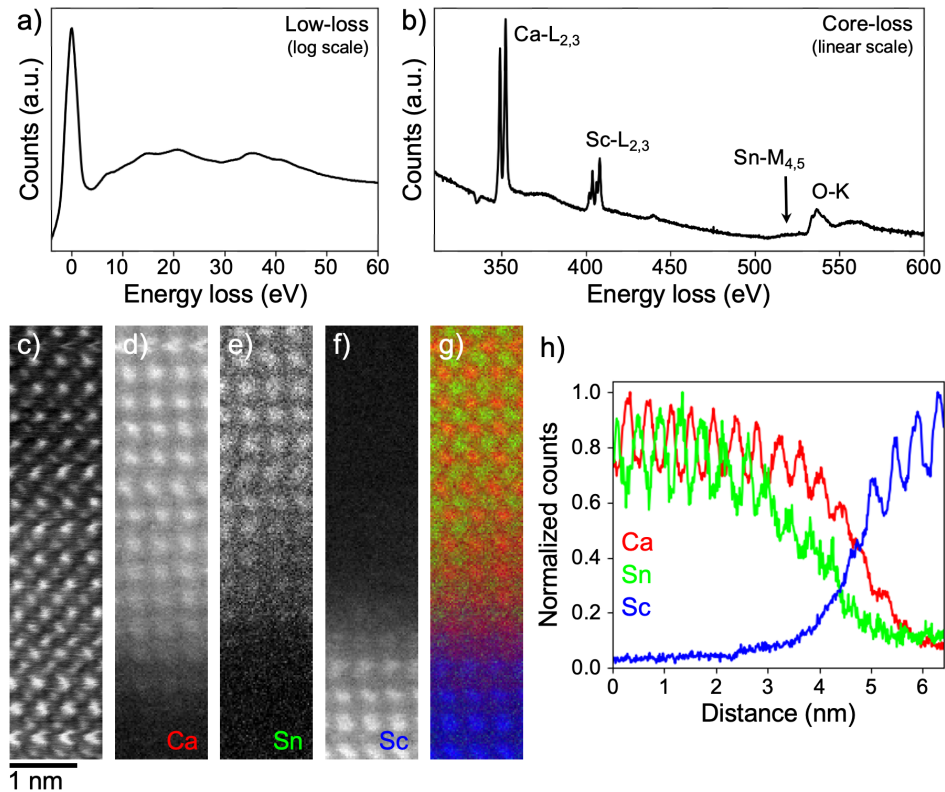


Figure 1.5: EEL spectra and atomic-resolution elemental maps of a $\text{CaSnO}_3/\text{GdScO}_3$ interface. (a) low loss and (b) core-loss spectra summed over the field of view shown in c-g. (c) ADF-STEM image of the $\text{CaSnO}_3/\text{GdScO}_3$ interface and (d-f) simultaneously acquired elemental maps of the (d) $\text{Ca-L}_{2,3}$, (e) $\text{Sn-M}_{4,5}$, and (f) $\text{Sc-L}_{2,3}$ EELS edges. (g) False-colored elemental map with Ca, Sn, and Sc intensities shown in red, green, and blue, respectively. (h) Line profiles of the Ca, Sn, and Sc signals from g summed horizontally showing intermixing over a few unit cells at the interface.

has traditionally limited their usefulness for spatially resolved mapping [104]. Recent advances in monochromation and momentum-resolved EELS, however, have improved the achievable spatial resolution for specific scattering geometries, leading to renewed interest in the low-loss regime [55, 53, 149].

The core-loss region comprises edges formed by core-level excitations. Each edge is characteristic of a particular element and transition from a core energy level to an unoccupied state above the Fermi level. The edges are named according to their associated transitions (e.g. $\text{Ca-L}_{2,3}$ or O-K as shown in Figure

1.5b). They can therefore be used for atomic-resolution elemental mapping as shown in Figure 1.5d-g. Analogous to Figure 1.4, panel c of Figure 1.5 shows an ADF image acquired simultaneously with the EELS signal, and panel g shows a false-colored elemental map formed by the Ca-L_{2,3}, Sn-M_{4,5}, and Sc-L_{2,3} EELS edge signals in red, green, and blue, respectively. The individual elemental maps are shown in Figure 1.5d-f. Prior to integrating the edge intensities, the background, formed by high-energy tails of valence-level excitations and lower-energy core-level excitations, must be removed. This is typically done by fitting the region of spectrum just before the edge to a power law (or linear combination of power laws) function. At high energy, as the background flattens out, an exponential function can also be a good choice. More detailed discussions of background subtraction for core-loss edges can be found in the following references [28, 46, 37].

Beyond elemental composition, EELS contains rich information about local bonding and electronic structure encoded in the shape of each core-level edge, known as the energy-loss near-edge structure (ELNES). To first approximation, the ELNES represents the local unoccupied density of states available to the excited electron. It can therefore be used to map subtle variations in bonding [105, 163, 48] and valence state [111, 106, 155, 123]. Qualitatively, the near-edge structure often contains features characteristic of particular bonding environments. The near-edge structure of the C-K edge, for example, has distinct regions associated with π^* and σ^* antibonding orbitals, allowing for differentiation between the diamond, graphene, and amorphous carbon allotropes [105]. It is sometimes also possible to use core-loss edges to robustly differentiate between valence states, for example by shifts in the energy of the edge onset or by the so-called white-line ratio calculated from the L_{2,3} edge [120, 127]. In calculat-

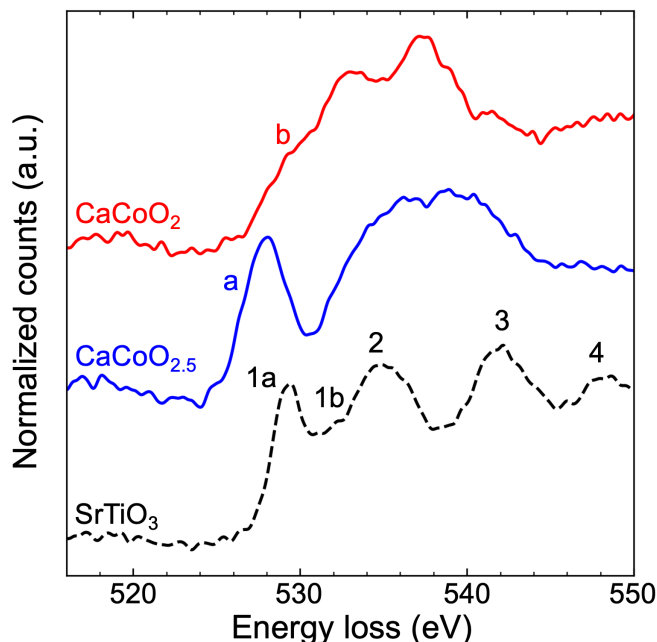


Figure 1.6: O-K edge ELNES analysis of $\text{CaCoO}_{2.5}$ and CaCoO_2 thin films and a SrTiO_3 substrate. Area-averaged EEL spectra for $\text{CaCoO}_{2.5}$ and CaCoO_2 thin films in blue and red, respectively, and a SrTiO_3 substrate in black. The SrTiO_3 is a prototypical O-K edge exhibiting three main regions. The first two features, labeled 1a and 1b correspond to O $2p$ and Ti $3d$ hybridized states. The feature labeled 2 corresponds to hybridization between O $2p$ and Sr d bands and the features labeled 3 and 4 relate to hybridization with higher energy metal states. The $\text{CaCoO}_{2.5}$ and CaCoO_2 spectra present a more complex case. The Co ions in the $\text{CaCoO}_{2.5}$ and CaCoO_2 films have different valence states and different coordination geometries with the O^{2-} ligands, leading to differences in the local electronic structure and corresponding variations in the shape of the edge. In particular, a suppression of the distinct pre-peak (labeled a) is observed in the region of the O-K edge associated with hybridization between O $2p$ and transition metal d orbitals consistent with a nominal electron configurations of $3d^6$ to $3d^7$ for the $\text{CaCoO}_{2.5}$ and CaCoO_2 films, respectively. The emergence of a shoulder in the CaCoO_2 spectrum (labeled b) has been attributed to ligand hole states analogous to those noted in a similar structure [48].

ing white-line ratios, one must be careful to avoid artifacts induced by multiple scattering effects, which influence the intensity of the post-edge. In very thin specimens, these measurements can be used to investigate interface effects in oxide heterostructures or other local defects in the crystal lattice [106, 8].

In $3d$ transition metal perovskite oxides, the O-K edge is particularly useful,

as it is largely formed by transitions from the $1s$ to $2p$ states. It is thus highly sensitive to hybridization between the O $2p$ and the transition metal $3d$ orbitals. The near-edge structure can therefore be interpreted with respect to crystal field and exchange splitting [31, 79], providing significant insights into the oxygen coordination geometry as well as the valence states of the cations. The O-K edge of SrTiO_3 , shown in black in Figure 1.6, represents a well-studied example of some of these effects. There are three main regions of this edge. The first ~ 5 eV correspond to excitations into the hybridized O $2p$ and the transition metal $3d$ orbitals that split into the t_{2g} and e_g bands. This results in the first two features of the edge, labeled 1a and 1b. The second region spans from approximately 5 to 10 eV and corresponds to hybridized states between the O $2p$ and A-site cation d bands (Figure 1.6 feature 2). Finally, the rest of the edge relates to hybridization with higher energy metal bands. In the case of SrTiO_3 , features 3 and 4 in Figure 1.6 relate to the Sr $5p$ and Ti $4sp$ states. The $\text{CaCoO}_{2.5}$ and CaCoO_2 O-K spectra also included in Figure 1.6 represents a more complicated system where this type of analysis can nonetheless provide some insights. Interpretation of these spectra will be discussed in detail in Chapter 5.

More detailed discussions of the theory of core-loss EELS, first described in the quantum mechanical framework by Hans Bethe [13, 14], can be found in the following useful references [77, 37]. The following also provide excellent reviews of ELNES analysis [126, 71, 138].

1.1.4 *In situ* temperature control

The ability to vary the temperature of a sample in the STEM opens the door to studying many exciting phases that exist only above or below room temperature. Cryogenic STEM in particular enables measurements of many exotic quantum phenomena that exist only at low temperature, including electronic transitions, charge density wave phases, and superconductivity [171, 97]. Efforts toward low temperature imaging go back nearly as far as the invention of the TEM itself [61], and there has been a significant resurgence of interest in recent years.

In materials science, cryogenic cooling in the (S)TEM is typically achieved using a conventional side-entry holder with a small dewar attached to the end. The dewar is filled with a cryogen (usually liquid nitrogen, LN₂) and coupled to the sample cradle by a copper rod. One challenge of cryo-(S)TEM is that the length of the copper rod leads to a temperature gradient between the dewar and sample, which results in significant sample drift even when the sample is nominally at the base temperature. Additionally, mechanical instabilities due to bubbling of the LN₂ in the dewar can be coupled to the sample. Scan artifacts due to these instabilities can be significantly reduced by acquiring a series of images with a low pixel dwell time and subsequently aligning and summing the images using a rigid registration technique as discussed above [133].

Besides accessing low temperature phases, *in situ* cooling can also be used to greatly reduce sample damage in beam-sensitive samples and to "freeze out" the buildup of carbon contamination under the beam. Of course, an entire field has sprung up around the former capability with respect to imaging biological samples. In materials research, the latter is particularly beneficial to

the study of nanocrystals, which are often covered in organic ligands that prevent the nanocrystals from agglomerating during solution processing. These organic molecules diffuse under the electron beam and build up during imaging. Common sample cleaning techniques like plasma cleaning or heating are often not good options for nanocrystal samples as they risk modifying or damaging the nanocrystals. Cooling the samples to liquid nitrogen temperature prevents diffusion of organic molecules and the associated contamination and is thus a good choice for otherwise sensitive samples. This concept is also useful for bulk and thin film samples that are particularly air and temperature sensitive as is demonstrated in Chapter 5.

It should be noted that the conventional cryo STEM holders described above can only be operated at room temperature or the base temperature reached by the cryogen (~ 96 K for LN₂). *In situ* heating holders, on the other hand, can be set to any intermediate temperature between room temperature and a max temperature, with the max temperature and minimum step size dictated by the holder specifications. There are several commercial holders available that use microelectromechanical (MEMS) devices to achieve this functionality. These devices provide good thermal and mechanical stability because the heated area is so small ($\sim 300 \times 300 \mu\text{m}$). Each chip is essentially a miniature electric heating coil covered in a silicon nitride membrane upon which the sample sits. The temperature is controlled via four electrical contacts, two of which apply a voltage while the other two measure the current and thereby the temperature. In addition to their good thermal stability, recent advances in the design of these MEMS devices have limited the bulging of the membrane caused by thermal expansion. It is therefore straightforward to track a region of interest through heating cycles. This functionality was leveraged to track the evolution of strain

defects upon thermal annealing in connected quantum dot superlattices as discussed in Chapter 2.

In an exciting next step, a holder has recently been developed that combines the capabilities of liquid nitrogen cooling and MEMS-based heating to enable continuously variable *in situ* temperature control between ~ 100 and 1000 K [47]. This level of temperature control holds significant promise for tracking and understanding phase transitions, including effects of local heterogeneity that are not accessible by other probes

1.2 Thesis outline

In this work, I will highlight the capability of STEM to elucidate atomic displacements in systems with nanoscale heterogeneity across a wide variety of systems for materials discovery and advancement. In Chapter 2 I will discuss the quantification of defects in epitaxially connected quantum dot superlattices, also known as quantum dot solids. Here, STEM enabled the identification of distinct strain defects that contribute to disorder and inhibit carrier delocalization in these materials. I will discuss the development of a new strain mapping technique for quantifying these defects and its utilization to study the evolution of defects upon *in situ* thermal annealing.

While a bespoke method was necessary to quantify strain in quantum dot superlattices, the most direct way to assess atomic displacements is through atom tracking of each atomic column in a STEM image. This has become an invaluable technique in the field of quantum materials where such measurements can elucidate ordering mechanisms and local heterogeneities in systems

exhibiting ferroelectricity, periodic lattice displacements and other strongly correlated electron phenomena. In Chapter 3 I will examine artifacts that can arise in atom tracking measurements of distorted perovskites due to electron channeling effects. I will demonstrate experimentally and through simulation that cation sites in distorted perovskites can appear displaced by several picometers with respect to their true positions in shared cation-anion atomic columns where the anions are coherently displaced. I will then discuss the magnitude and dependencies of the apparent displacements and ways by which they can be minimized or avoided. Chapter 4 will present an example study where oxygen-channeling induced artifacts were avoided through careful data analysis. In this chapter, the domain structure of oxygen vacancy ordered phases of $\text{LaNiO}_{3-\delta}$ was mapped using 4D-STEM and the lattice displacement patterns associated with the $\delta = 0.5$ and 0.25 phases were elucidated.

Chapter 5 discusses an additional system, CaCoO_2 , where careful atomic position measurements were instrumental in determining the structure of a new, highly distorted infinite-layer phase. Here, HAADF- and ABF-STEM imaging were used to first reduce the phase space for a partial x-ray refinement and to ultimately determine the correct structure from multiple potential refinements. Further, the electronic structure of CaCoO_2 was investigated using EELS in the context of its demonstration as the first reported 2D Jahn-Teller effect in a metal-oxide compound.

CHAPTER 2
MAPPING DEFECT RELAXATION IN QUANTUM DOT SOLIDS UPON
IN SITU HEATING

2.1 Background

Epitaxially connected superlattices of quantum dots, called quantum dot solids (QDS), present an exciting route toward designer electronic materials with tunable miniband structures [69, 68]. While traditional quantum dot (QD) thin films have found use in a wide variety of devices including field effect transistors, photovoltaics, and photodetectors [130, 125, 64, 161, 159, 58, 109, 88], introduction of the oriented attachment process to form ordered superlattices with epitaxial connections between neighboring QDs provides two key advantages. Namely, superlattice geometry provides an additional knob with which to tune electronic structure [69, 68, 146], and epitaxial connections provide strong electronic coupling between QDs allowing for charge delocalization [69, 32, 129]. The hierarchical nature of QDS films allows control over the electronic structure *via* the size, shape, and composition of the QD building blocks, as well as the geometry of the superlattice. This results in tunable band gaps for electronic device applications [12, 38, 23, 156, 2], as well as exotic, theoretically predicted miniband structures such as Dirac cones, topological edge states, and nontrivial flat bands for QDS films in the 2D limit [68, 87, 117].

Whitham and coworkers, however, recently showed that charge delocalization, upon which this rich opportunity space is contingent, is limited by disorder in the films [156]. Faulty epitaxial connections cause variation in the electronic coupling between QDs, which subsequently disrupts formation of a miniband

structure [156, 134]. Recent work has attempted to elucidate the origin of reduced electronic coupling by identifying the types of dislocations possible in imperfectly attached QDs and their removal pathways [112, 113], and quantifying positional and orientational disorder [134, 93, 122]. The latter study also noted the presence of strained bridges between imperfectly oriented QDs even when the atomic lattice remained coherent, and suggested the need for further exploration.

Thermal annealing has been proposed as a method to heal faulty epitaxial connections, thus recovering proper electronic coupling and charge delocalization. For example, *in situ* TEM experiments have shown that randomly attached PbSe nanocrystals undergo multiple rotation and interface relaxation steps at 100-150°C in order to fuse into larger single crystals [145]. More recently, transport measurements and X-ray scattering techniques demonstrated an increase in carrier mobility and accompanying decrease in mosaicity and microstrain upon heating, which was attributed to a decrease in the density of edge dislocations and point defects [152]. However, to understand how defect relaxation takes place and to what extent it occurs, local, atomic-scale visualization during *in situ* heating is necessary.

In this work we use atomic-resolution high-angle annular dark-field scanning transmission electron microscopy (HAADF-STEM) imaging in combination with *in situ* heating to identify the nature of defects present in PbSe QDS monolayers and to visualize their evolution upon thermal annealing. Utilizing local strain mapping and QD orientation tracking, we distinguish between tensile, shear, bending, and twisting defects present in epitaxial connections. Tracking distinct defect types, we find that tensile and shear defects are fully

relaxed upon heating to 150-200°C, while bending defects remain, suggesting different energies associated with these defects.

2.2 Results and discussion

We fabricated QDS monolayer films composed of ~ 6 nm PbSe QDs connected along the $\langle 100 \rangle$ crystallographic directions using interfacial assembly [156]. In order to apply stable, rapid heating, we used an *in situ* TEM heating holder (DENSolutions Wildfire system). Localized heating provided by a MEMS device with ~ 20 nm thick SiN support windows allowed us to track a region of interest through multiple heating cycles, acquiring atomic-resolution images over ~ 100 nm fields of view. All images used for strain analysis in this work were acquired at room temperature between heating cycles and consist of single STEM scans in order to minimize electron beam effects due to multiple exposures. Furthermore, the beam was blanked or well away from the areas of interest during annealing to avoid affecting the annealing process. We note that carbon contamination buildup during imaging can suppress annealing effects especially at modest annealing conditions and therefore has to be avoided.

After mild heating at 150°C for 30 minutes we observe several local structural changes, examples of which are shown in Figure 2.1. In agreement with recent *ex situ* TEM experiments [152], we find that some of the necks between QDs widen upon heating (Figure 2.1a), presumably due to surface diffusion driven by reduction in surface area. A schematic representation of this process is shown in Figure 2.1b. Additionally, we observe new epitaxial connections forming, often accompanied by rotation of one or more QDs into better align-

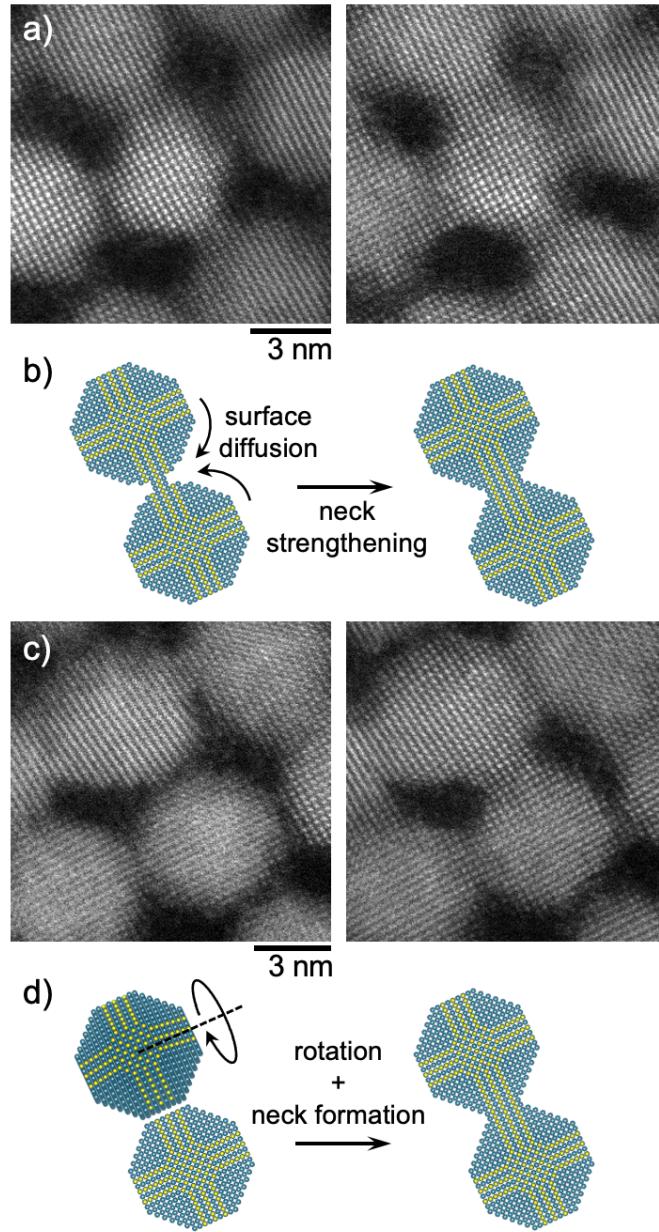


Figure 2.1: Examples of local heating effects in an epitaxially connected square superlattice of PbSe QDs. (a,c) HAADF-STEM images of two regions of a PbSe QDs monolayer before (left) and after (right) heating for 30 minutes at 150°C. (b,d) corresponding schematic representations of the changes observed in a and c. Scale bars are 3 nm.

ment with its neighbor, as shown in Figure 2.1c,d. We expect such rotations occur only when the total strain energy for all nearest neighbor connections is decreased, as we discuss in detail below. Though several instances of neck for-

mation were observed, a statistical analysis of the overall connectivity is outside the scope of the current study and is not reported here. From these observations, we conclude that heating to 150°C allows atomic motion and even rotation of full QDs despite the Van der Waals interactions with the SiN surface they sit on. We note that due to the projection nature of STEM we cannot quantify the extent of the rotation by imaging alone. However, based on our previously reported work using nanobeam diffraction mapping with 4D-STEM, we expect that most rotations are less than six degrees [30]. Rotation of a QD to match the crystallographic orientation of one of its neighbors can then enable formation of a new connection between them. Relative rotations between QDs that are already epitaxially connected appear to be driven by reduction in the strain in the connection. From direct visualization, we identify four discrete strain states that exist in QD connections, namely: twisting, bending (in-plane (IP) and out-of-plane (OP) being possible), shear and tension.

We utilize two methods to measure these strain states and assess their evolution upon heating. To measure IP bending, shear and tension, we locally fit the atomic lattice fringes using 2D sine functions, an approach formerly developed for scanning tunneling microscopy [119], and to measure twisting and OP bending we identify the OP orientation of each QD in the film using local Fourier transforms [93]. Previously, strain mapping was achieved using geometric phase analysis (GPA) [65]. However, drawbacks become apparent when applying GPA to this QDS system, which is composed of a superlattice of QDs representing individual and imperfectly aligned crystalline domains and containing defects characterized by highly localized strain. The first drawback results from the fact that GPA relies on identification of a fixed reference lattice. Given the multitude of crystalline domains present in our samples, any phase

images resulting from GPA analysis appear very convoluted and are difficult to interpret. This difficulty is partially due to phase wrapping artifacts, which not only introduce nonphysical singularities, but can also obfuscate real features caused by defects. Though it is possible to unwrap or avoid these artifacts to an extent, each method thereof introduces its own complications [119, 65]. The other advantage of our real space method is it provides highly local information, maintaining accuracy for high-magnitude and nonuniform strain regions, where the accuracy of GPA suffers [166, 119]. A local version of GPA has been developed, which utilizes the windowed Fourier transform algorithm to improve upon these limitations [166]. However, it still exhibits the same drawbacks related to phase wrapping. Real space strain mapping was recently demonstrated for multigrain nanocrystals by fitting 2D Gaussian functions to the atomic columns of a STEM image and calculating displacements from the ideal lattice [108]. This method, however, still requires a fixed reference lattice and is limited to crystals which are perfectly aligned along the optic axis, making it unsuitable for our system.

In our sine wave fitting approach, we Fourier filter one pair of Bragg peaks at a time and locally fit 2D sine functions to the resulting real space image using a fit window of ~ 1.5 times the wavelength of that lattice spacing. Given the rock salt crystal structure of PbSe, we use the (200) and $(\bar{2}00)$, and (020) and $(0\bar{2}0)$ Bragg peaks for the **a** and **b** directions, respectively, and a fit window size of ~ 5 Å. For each pair of {200} Bragg peaks, the fit directly yields the local lattice spacing and the in-plane lattice rotation, which can then be used to obtain the local tensile and shear strains across the field of view. More detail on this process can be found in the methods section (Section 2.4.1).

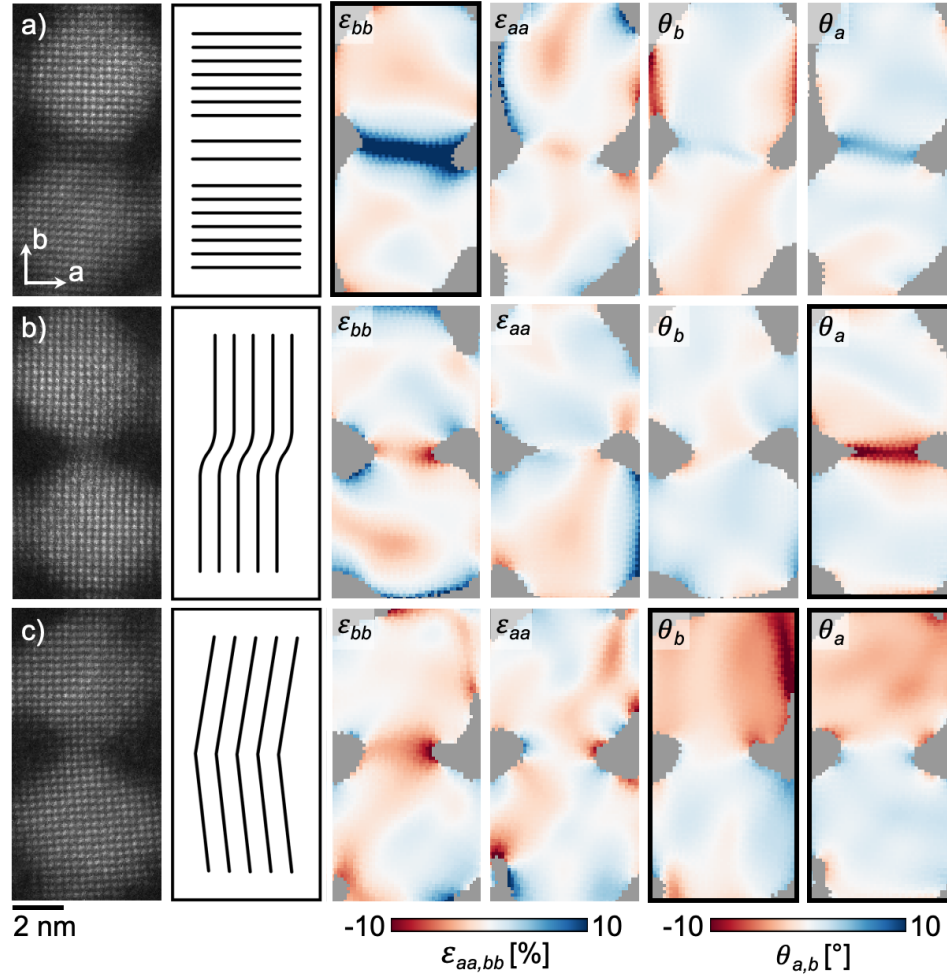


Figure 2.2: Examples of tensile (a), shear (b), and bending (c) strain states in necks between QDs. From left to right, each row shows a HAADF-STEM image of two QDs and the neck region between them, a schematic representation of the strain in the relevant lattice planes, and maps of the tensile strain, ϵ_{mn} , and rotation, θ , for the lattice vector indicated in the upper left corner of each map. The most characteristic map for each strain type is outlined in black.

Figure 2.2 presents examples of characteristic tensile strain and rotation maps for both **a** and **b** directions for each of the three strain states. While it is possible for a given neck to exhibit multiple strain types, these examples have been chosen such that one defect type is clearly dominant. In all maps, a gray mask is applied where the lattice fringe amplitude is below one tenth of the maximum amplitude. This occurs in voids between QDs and for QDs that are tilted far off of the zone axis. Furthermore, the masks for the **a** and **b** directions

are defined independently and do not match exactly. This is because, due to the OP misalignment of the QDs, both sets of lattice fringes are not always visible. The local lattice spacing has been converted to engineering tensile strain using the relation $\epsilon_{nn} = (\lambda_n - \lambda_{n,avg})/\lambda_{n,avg}$, where the subscript n refers to the Bragg frequency it is being applied to, while the rotation values (which could be used to calculate shear strain) are simply presented as the angular difference from the average and are thus related to shear strain. The advantage of plotting rotation values is that it allows us to retain the local orientational information needed to unambiguously identify bending between neighboring QDs. Tensile strain states can be easily identified as areas of high intensity in the tensile strain maps like that shown in Figure 2.2a, where a tensile defect is evident in the neck region in the longitudinal (parallel to the connection axis) lattice map. This effect in the longitudinal lattice is represented schematically in the second panel of Figure 2.2a.

The relationship between the rotation map and shear strain is somewhat more complex, as the strain would be given by the deviation of the difference between the **a** and **b** lattice vector rotations from ninety degrees (the ideal lattice). Therefore, in the rotation maps, shear strain can be identified by high magnitude features which appear for only one lattice direction. An example of this is shown in Figure 2.2b, where the rotation map for the transverse lattice vector (perpendicular to the connection axis) exhibits high magnitude intensity at the bridge. We note that bridges containing a shear or tensile strain defect often contain the other strain type as well, though with a lower magnitude. We believe the presence of one strain defect at a bridge decouples the lattice enough such that other strain defect types may be introduced at a lower energetic cost. Additionally, we find that in the case of both tensile and shear defects, the strain

is localized to only a few atomic planes.

Finally, bending strain defects are characterized by a change in the rotation value of one QD compared to its epitaxially connected neighbor as schematically shown in the transverse lattice in panel two of Figure 2.2c. For a square atomic lattice, which is preserved in the core of the QDs, the observed change should be the same in both orthogonal lattice directions. In strained neck regions, however, shear strain can give rise to additional variations in the individual rotation maps as discussed above. We therefore focus on the relative lattice rotation at the core of neighboring QDs for identification of bending strain defects. Additionally, in keeping with bending in a macroscopic beam, the tensile strain map for the longitudinal lattice vector may exhibit a compressive region on the inner edge of the bend and/or a tensile region on the outer edge. However, due to other contributions in the neck region this strain distribution is not consistent between bridges, making it a less reliable metric for identification of bending strain defects.

The results discussed so far focus on single epitaxial connections between two QDs and demonstrate that our local lattice mapping approach allows us to differentiate between tensile, shear and bending strain states. For all results shown in this work, the error associated with the tensile strain and rotation maps is significantly lower in magnitude than the features characteristic of all three strain defect states. Additional details of measurement error are discussed in the Methods (Section 2.4.1). We note that this strain mapping method quantifies in-plane strain; out-of-plane strain contributions are not extracted. Additionally, QDs which do not display lattice fringes due to large out-of-plane misalignment will be excluded. The method requires that the Fourier space mask

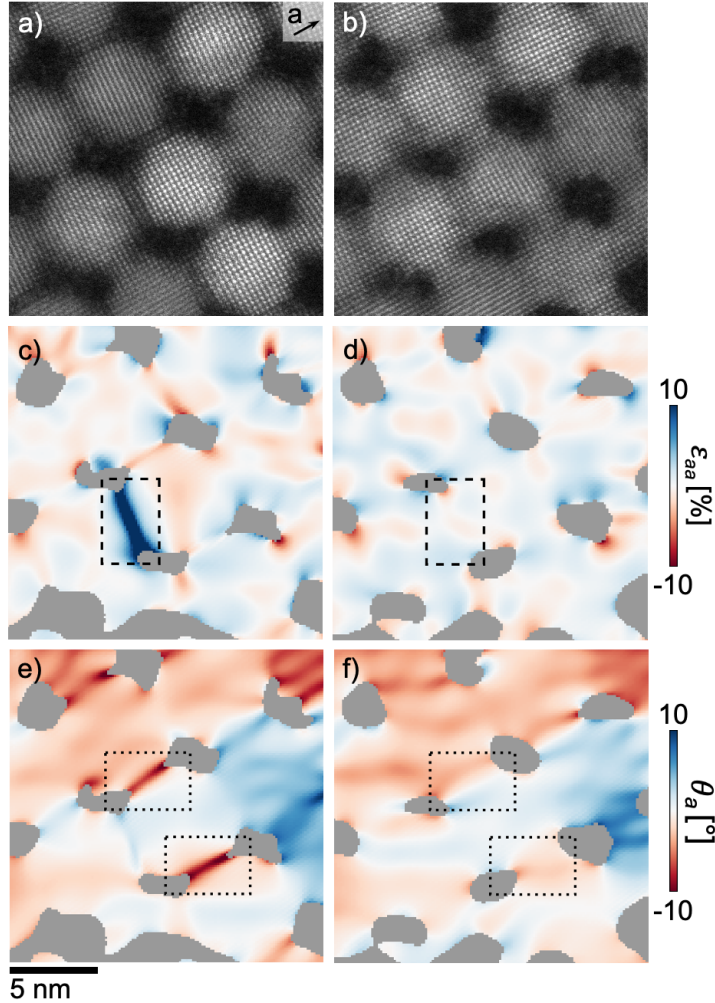


Figure 2.3: Evolution of tensile, shear, and bending strain states upon *in situ* heating. (a,b) HAADF-STEM images of a region of QDS film before (a,c,e) and after (b,d,f) heating for 50 minutes at 150-200°C, with corresponding tensile strain (c,d) and rotation (e,f) maps. Examples of tensile and shear strain are outlined by dashed and dotted lines, respectively, in c and e. Upon heating, the strain disappears, as shown in d and f.

size be carefully chosen so as not to artificially limit the magnitude of tensile strain and rotation extracted.

Having identified the characteristic features present in the tensile strain and rotation maps, we consider how tensile, shear, and bending strain defects evolve in a region of a monolayer film after heating first for 30 minutes at 150°C and then for an additional 20 minutes at 200°C. We consider the initial and final

states in Figure 2.3. From the maps, it is clear that the tensile and shear defects observed before heating and outlined by dashed and dotted lines, respectively, in Figure 2.3c,e are relaxed after heating, as shown in Figure 2.3d,f. However, the bending defects between QDs appear largely unaffected. Given the high magnitude of the shear and tensile defects, it is unsurprising that they are relaxed first as the strain energy introduced by those defects is expected to be correspondingly higher in magnitude, and the energy barrier to relax them is expected to be lower as it requires reorganization of a few planes of atoms instead of the full QD, which is further constrained by connections with other nearest neighbor QDs. Thus, the persistence of the bending defects is due to a combination of lower strain energy and higher energetic barrier to relaxation. The data presented here is not sufficient to quantify the influence of the two effects. Though the relaxation of tensile and shear defects shown here is possible *via* strictly in-plane motion of the atomic lattice, the limitation of this method to in-plane strain measurement means we cannot exclude possible effects from out-of-plane displacements during relaxation. It should be noted that the maps presented in Figure 2.3 represent only the **a** lattice vector as indicated in the upper right corner of Figure 2.3a. The maps for the **b** lattice vector, shown in Figure 2.4, are less well defined due to the atomic lattice of more QDs being somewhat misaligned with respect to the zone axis.

We confirm these trends by extending the analysis to a larger field of view as shown in Figure 2.5. Here, we maintain the unit cell-scale strain information while encompassing approximately 140 QDs. We also include the intermediate heating time point. The tensile strain and rotation maps shown in Figures 2.5a and d, b and e, and c and f correspond to the film before heating, after heating for 30 minutes at 150°C, and after heating for an additional 20 minutes at 200°C,

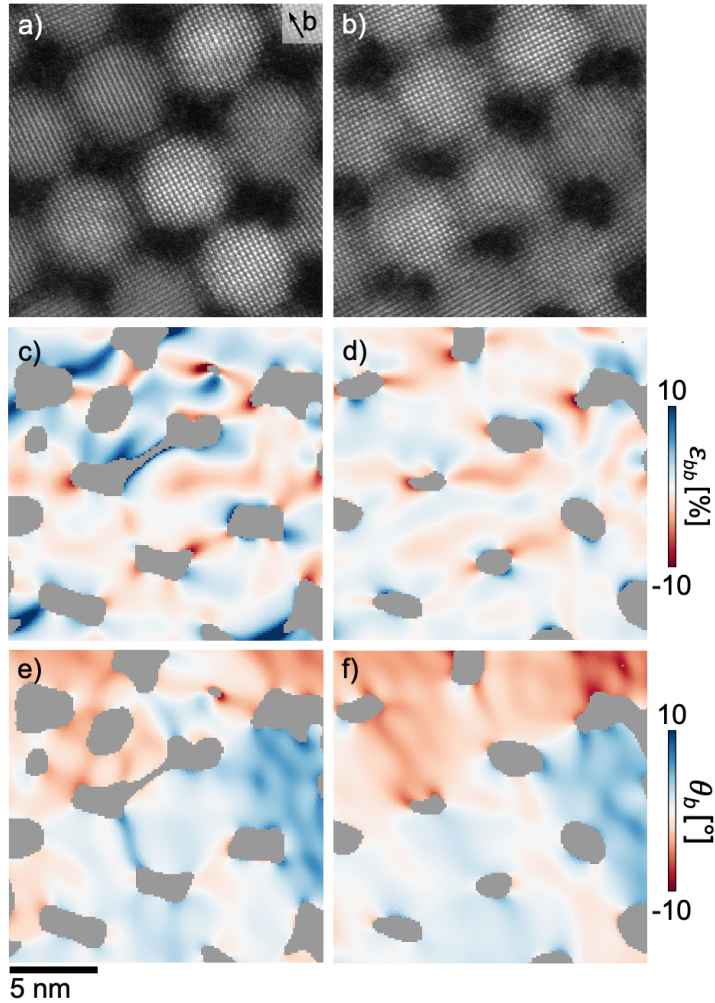


Figure 2.4: Evolution of strain states upon *in situ* heating in the orthogonal lattice vector over the same field of view. (a,b) HAADF-STEM images of the same region of QDS film as in Fig. 2.3 before (a,c,e) and after (b,d,f) heating for 50 minutes at 150-200°C, with corresponding tensile strain (c,d) and rotation (e,f) maps. An example of shear strain is outlined by dashed lines in e. Upon heating, the strain disappears, as shown in f.

respectively. In nearly all cases, tensile and shear defects, identified in the tensile strain and rotation maps, respectively, are relaxed after the final annealing step, leaving a relatively uniform tensile strain map and a rotation map with only the variation between QDs caused by residual bending strain states. Thus, we confirm the case presented in Figure 2.3 insofar as the high magnitude, localized tensile and shear defects are relaxed upon heating, but bending defects

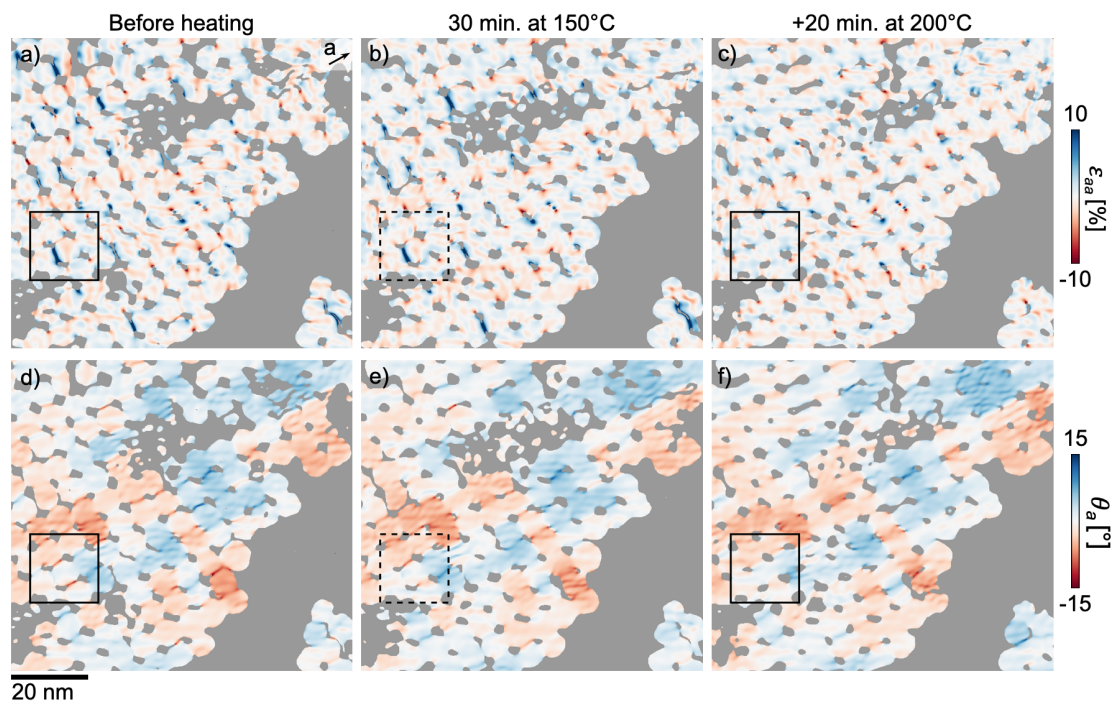


Figure 2.5: Strain states and heating effects tracked over a large field of view. Strain maps for a ~ 100 nm field of view before heating (a,d), after heating for 30 minutes at 150°C (b,e), and after heating an additional 20 minutes at 200°C (c,f). Tensile strain and rotation maps are shown in a-c and d-f, respectively. The black outlines indicate the region shown in Fig. 2.3. As in that region, upon heating, the tensile and shear strain states are relaxed across the whole field of view.

are left largely unchanged. It is interesting, also, that the intermediate time point shows only minimal strain relaxation, particularly of some shear defects, with the majority of the relaxation occurring only after the second heating step. Based on the current data, we cannot conclude whether this is due to the higher annealing temperature, or simply the additional heating time. Further experiments are planned to investigate the relationship between the strain relaxation and the time *versus* the temperature of annealing. We also note that, upon heating, some QDs either partially or fully masked in the initial maps are filled in, meaning that the QDs have rotated such that the atomic lattice is oriented down the zone axis and are therefore accessible to our projection-based quantification. Those QDs which are initially partially masked begin with only edges visible

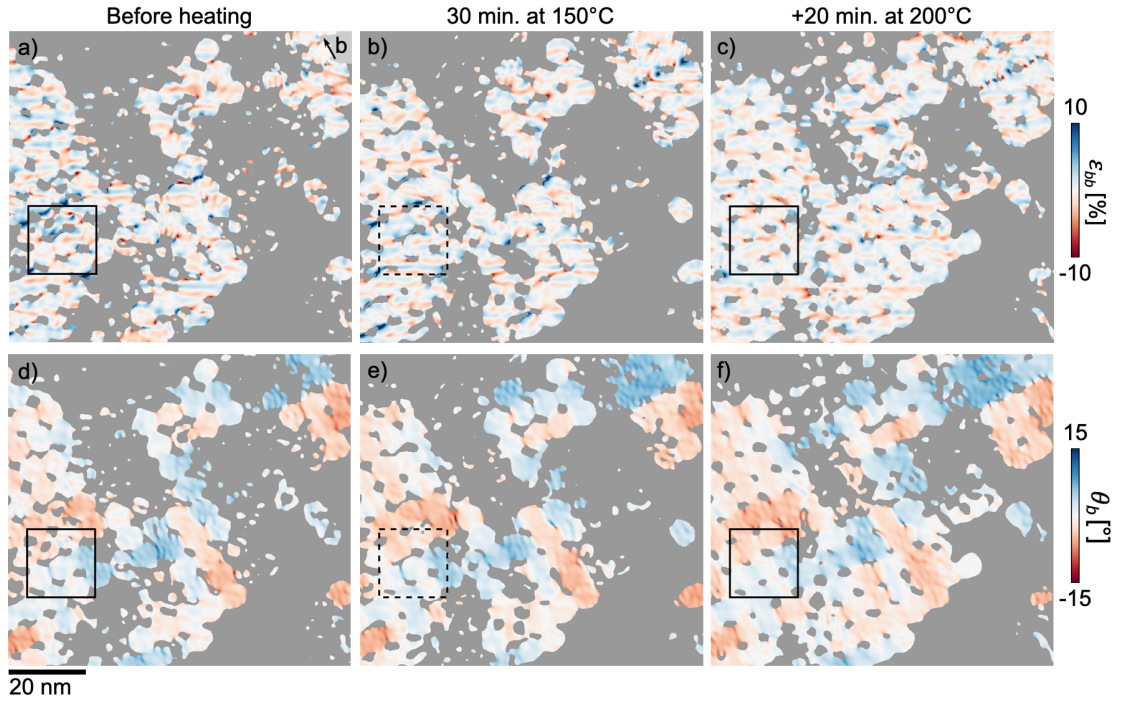


Figure 2.6: Strain states and heating effects tracked over a large field of view in the orthogonal lattice vector. Strain maps for the same field of view as Fig. 2.5 before heating (a,d), after heating for 30 minutes at 150°C (b,e), and after heating an additional 20 minutes at 200°C (c,f). Tensile strain and rotation maps are shown in a-c and d-f, respectively. The black outlines indicate the region shown in Fig. 2.4. As in that region, upon heating, the tensile and shear strain states are relaxed across the whole field of view. Horizontal streaks in a-c are due to scan noise in the raw image.

in the maps and fill in entirely upon heating. In these cases, the QD must be only slightly misaligned out-of-plane such that as the projected thickness of the QD decreases moving from the center to the edge of the QD, the lattice becomes visible, allowing those edges to be mapped. This is evidence that QDs rotate to become better aligned with respect to their neighbors, a phenomenon which will be discussed further below. Maps for the other lattice vector are shown in Figure 2.6.

In a few cases where the mismatch between QD rotations is particularly high (*i.e.*, there is significant bending in the epitaxial connection), upon heating, the

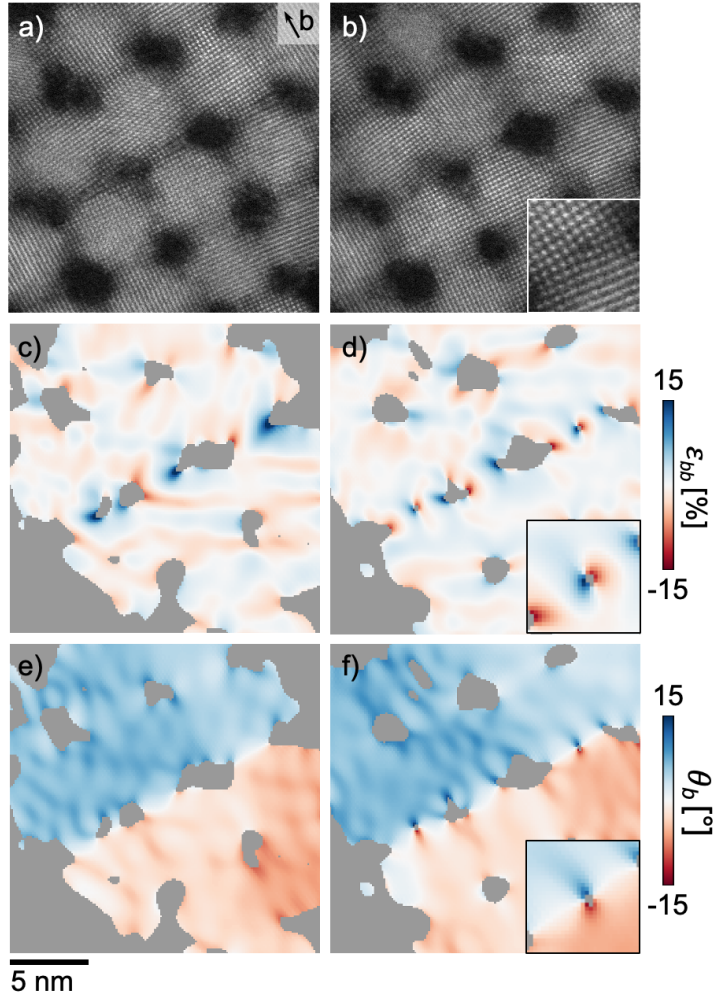


Figure 2.7: Examples of dislocation formation upon *in situ* heating. (a,b) HAADF-STEM images of a region of QDS film before (a,c,e) and after (b,d,f) heating showing the formation of dislocations in two epitaxial connections. Tensile strain and rotation maps are shown in c,d and e,f, respectively. The tensile strain maps before heating show concentrations of tensile and shear strain at the edges of the necks due to the high degree of bending. This strain is reaccommodated after heating in dislocation cores in two of the connections, one of which is highlighted in the insets of b, d and f. Horizontal streaks in c,d are due to scan noise in the raw image.

lattice forms a dislocation in the bridge rather than accommodate the high tensile and compressive regions at the outside and inside of the bend, respectively. A region of film showing two such cases is presented in Figure 2.7, where the dislocations form only after the final heating step. The rotation maps (Figures 2.7e,f) show a relatively high mismatch between the top row of QDs and the bot-

tom row, all of which are connected in both directions before and after heating. The tensile strain maps (Figures 2.7c,d), show the most striking transformation: the strain confined to the edges of the connections in the initial configuration is re-accommodated in the newly formed dislocation cores after heating. The insets in Figures 2.7b,d and f show one dislocation core, which is identifiable by a dumbbell-like feature in both the tensile strain and rotation maps. We infer from these cases that there exists a threshold above which the strain energy accommodated by a bending defect can be decreased by forming a dislocation and that the barrier to forming that dislocation is less than that to lessen the degree of bending strain *via* QD rotation, at least for the specific case of QDs epitaxially connected to all four neighboring QDs. For QD dimers, in contrast, dislocations have been shown to anneal out under the electron beam and upon heating [112, 113, 145]. Here, due to the constraint on in-plane rotation imposed by the other QD connections, we do not expect the dislocations to anneal out under the present heating conditions even with longer heating time. Simulations of these cases are needed to provide a clearer picture of the driving forces present in this complex situation. Similar to Figures 2.3 and 2.5, strain maps for the lattice vector orthogonal to those shown in Figure 2.7 are included in Figure 2.8.

Since STEM imaging is inherently a projection technique, we cannot measure the extent of out-of-plane (OP) misorientation in the QDs and therefore cannot directly observe twisting strain in QD bridges. Though OP orientation measurement of individual QDs was recently demonstrated using 4D-STEM [30], local OP mapping within an epitaxial bridge would pose significant additional challenges. As a proxy, we instead measure the distribution of OP orientations as enumerated in Figure 2.9d. We assign the QD OP orientations *via* an auto-

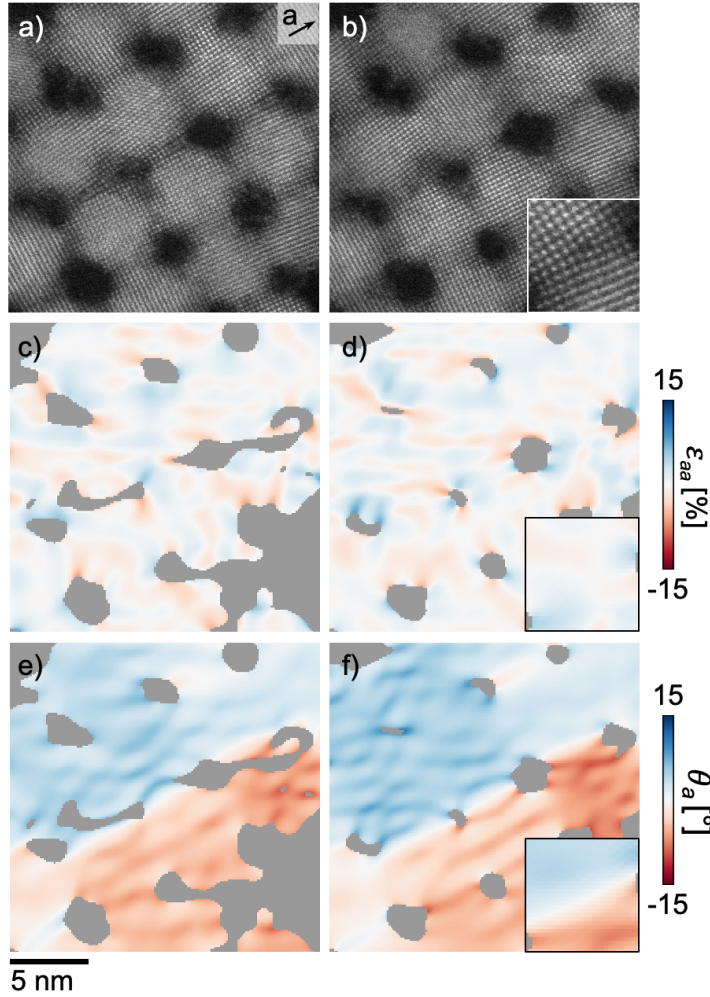


Figure 2.8: Companion to Fig. 2.7 showing strain maps for the orthogonal lattice vector. (a,b) HAADF-STEM images of the same region of QDS film from Fig. 2.7 before (a,c,e) and after (b,d,f) heating. Tensile strain and rotation maps are shown in c,d and e,f, respectively. The tensile strain maps show no concentrations of strain for this lattice since it is orthogonal to the Burgers vectors of the dislocations. However, the rotation maps still show the high degree of tilt between QDs as expected.

ated algorithm similar to that described by McCray *et al.* [93], which matches QD FFTs to expected patterns for each orientation. Bragg peaks were identified using a peak finding algorithm, and a threshold was applied to standardize the peak intensity required to assign a particular orientation. Thus, the quantitative threshold between orientations (*e.g.* $\langle 100 \rangle$ to $\langle 1n0 \rangle$ or $\langle 1nn \rangle$) is not known but is consistent between datasets, making the orientation distributions directly

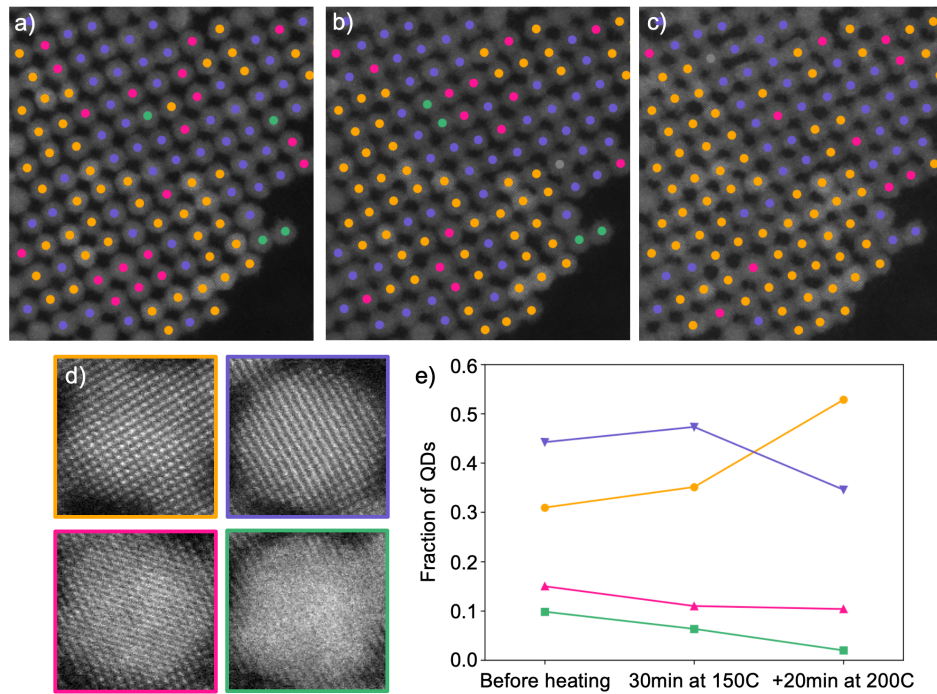


Figure 2.9: Tracking the out-of-plane orientation of QDs in a QDS film upon *in situ* heating. Maps of QD out-of-plane orientations as extracted before (a) and after heating for 30 minutes at 150°C (b) and an additional 20 minutes at 200°C (c). (d) Examples of the OP orientations observed in the film. (e) Evolution of the fraction of QDs with each OP orientation at each time point, showing an increase in the fraction of correctly oriented $\langle 100 \rangle$ QDs at the expense of all other orientations.

comparable.

In a perfect QDS film, all QDs would have the $\langle 100 \rangle$ orientation normal to the plane of the film. The introduction of QDs with some OP tilt with respect to their nearest neighbors necessarily creates bending and/or twisting strain in the epitaxial connections, based on the direction of tilt, assuming such connections have formed. Any increase in the fraction of correctly oriented QDs, then, should decrease the total twisting and OP bending strain. This analysis is thus an indication of the amount of twisting and OP bending strain in the film, but it is not a direct measurement. Of course, our analysis does not consider whether the connections are present; nor does it consider the possibility of rotation of a

given QD relaxing strain in one connection while simultaneously increasing the strain in one or more of the other three connections. However, the latter likely has a significant energetic cost, and we expect such a rotation would not occur unless the total strain energy is decreased by the rotation. This energy balance occurs for all QDs concurrently, so rotations of neighboring QDs may alter the energetic favorability of rotation at any point. It is also possible, if its nearest neighbor QDs are misaligned out-of-plane, for a QD to rotate away from the ideal orientation. Since most QDs are nearly aligned initially, however, we expect the net effect to be an increase in the proportion of correctly oriented QDs over time.

This effect is confirmed in Figure 2.9a-c, which shows a region of the QDS monolayer film with the assigned QD OP orientations (as enumerated in Figure 2.9d) overlaid. There is a marked increase in the number of correctly oriented $\langle 100 \rangle$ QDs from the initial to the final film after heating for a total of 50 minutes at 150-200°C. The evolution in the orientations of over 400 QDs is summarized in Figure 2.9e, showing an increase in the fraction of correctly oriented QDs and a corresponding decrease in all other orientations. We, therefore, conclude that sustained, mild heating also drives relaxation of twisting and OP bending strain *via* QD rotations. Furthermore, given that the extent of OP bending or twisting strain cannot be extracted from this data and the above conclusions that in-plane bending was largely unaffected in this heating regimen, we may infer that these QD rotations were driven more so by relaxation of twisting strain than OP bending strain.

These insights are consistent with recent findings from *in situ* X-ray scattering and rocking curve XRD experiments [152], in that local strain was reduced

and OP misalignment was decreased. However, since X-ray techniques sample a relatively large area of film, the collected signal averages over not only important spatial information but also the range of defect types present. The atomic-scale insights presented here allow us to not only distinguish between defect types but also to assess the benefits of thermal annealing on each.

2.3 Conclusions

In this work we identify and measure four distinct strain states in otherwise coherent epitaxial connections. We measure twisting and bending strain defects, which result from QDs misoriented in the out-of-plane and in-plane directions, and tensile and shear strain defects, which represent translational misalignment in the atomic lattice. Using strain mapping and orientation tracking techniques, we track the evolution of these strain defects upon thermal annealing. Tensile and shear defects fully relax after 50 minutes of annealing at 150-200°C, while bending defects remain. This indicates that the tensile and shear defects are higher in energy and thus produce a higher driving force for relaxation. The bending defects on the other hand are less energetically costly or perhaps are more constrained by connections with other nearest neighbors.

We also observe an increase in the fraction of correctly oriented $\langle 100 \rangle$ QDs upon heating, which indicates a decrease in the number of twisting and OP bending defects in the film. We surmise that the effect is due more to a decrease in twisting, than bending defects since strain mapping showed that IP bending defects were largely unaffected by annealing. Thus, the same may be true for OP bending defects.

The insights gained here into the types and behaviors of strain defects in imperfect epitaxial connections suggest that thermal annealing is highly effective at relaxing high intensity, localized defect types such as tensile and shear defects. However, open questions remain with regard to how best to relax bending defects, which still pose a barrier to charge delocalization. The need for precise control over the orientational order before oriented attachment occurs is, therefore, highly important and worthy of further study. Given this demonstration of the effectiveness of thermal treatments to improve the quality of QD connections, and the utility of direct methods for visualizing defect states in those connections, we believe thermal annealing represents significant potential to improve carrier delocalization and electronic coupling in monolayer QDS films and a step toward realizing predicted rich electronic structures.

2.4 Methods

STEM imaging was performed using an aberration-corrected FEI (now Thermo Fisher) Titan Themis operating at 120kV with a 21.4 mrad convergence angle. *In situ* temperature control was achieved using a commercial double tilt heating holder (DENSsolutions Wildfire system) with the QDS sample prepared on a Wildfire D6 nano-chip with a ~ 20 nm thick SiN support film. The sample remained at $\sim 1 \times 10^{-8}$ torr in the microscope column throughout thermal annealing.

The PbSe QDs and QDS were prepared following published procedures [156, 10]. QDs of 6.1 nm diameter dispersed in toluene ($4 \mu\text{M}$, $6 \mu\text{L}$) were spread on top of ethylene glycol contained in a Teflon trough ($1.5 \text{ cm} \times 1.5 \text{ cm}$) to form

a dense monolayer. Ethylene diamine diluted to 1M with glycol was injected at a final concentration of 25 mM to induce necking; the system was let to proceed for 3 minutes. The film was then transferred to the nano-chip using the Langmuir-Schaefer method and rinsed with MeOH to reduce contamination due to residual ligands.

2.4.1 Strain mapping

An outline of the strain mapping procedure is presented in Figure 2.10. The method is adapted from one previously developed for scanning tunneling microscopy [119]. Beginning with a large field of view, atomic-resolution HAADF-STEM image, we take the fast Fourier transform (FFT) and simultaneously filter the (200) and ($\bar{2}00$) peaks for the **a** direction and the (020) and (0 $\bar{2}0$) peaks for the **b** direction. This process results in two real space images each containing intensity only from the frequency of interest as defined by the filter windows. An example FFT is shown in Figure 2.10b, and the Fourier filtered image for the **a** direction is shown in Figure 2.10c. While the superlattice and atomic lattice peaks are both clearly visible in the FFT, the atomic lattice peaks appear as diffuse arcs due to the rotational disorder between QDs. Due to the lack of well defined peaks, we identify the peak positions manually, as standard fitting algorithms give inaccurate results. The size of the filter window (indicated by red circles in Figure 2.10b) is chosen to encompass the full disperse peak intensity, while minimizing the introduction of noise, particularly due to scan instability. It is possible to reduce this instability by acquiring and registering image stacks, however, the increase in total dose during acquisition of an image series may introduce beam induced effects. If the chosen window was too small,

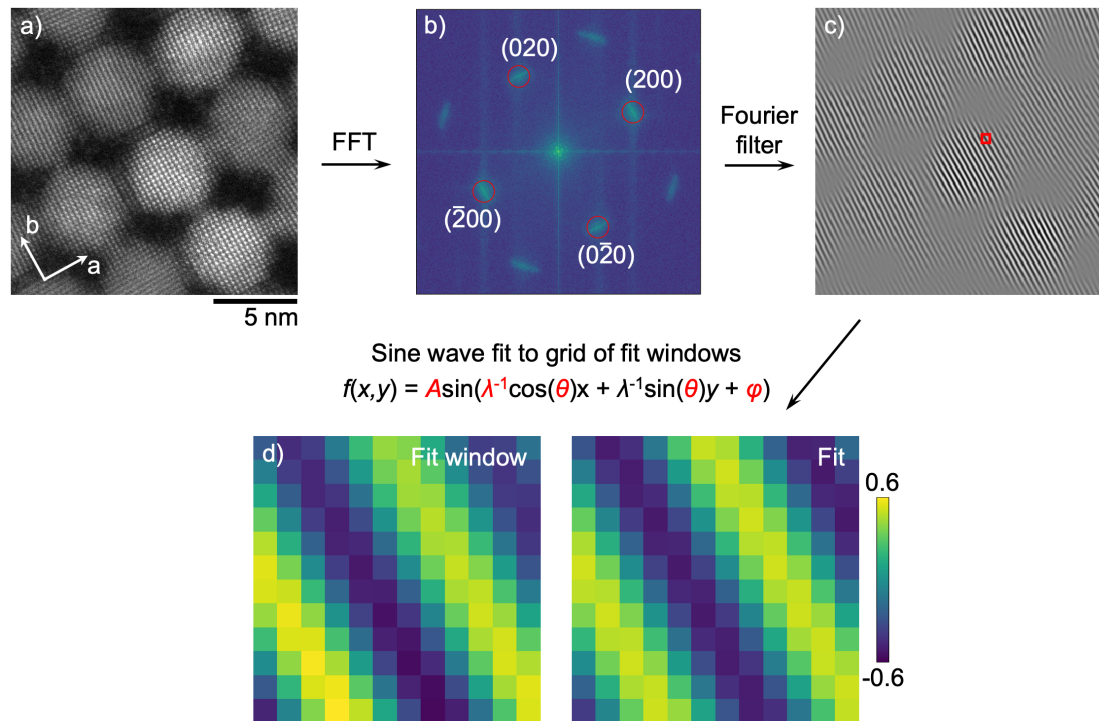


Figure 2.10: Workflow for the sine wave fitting method for strain mapping. (a) Subset of a raw HAADF-STEM image. (b) FFT of the full field of view showing the superlattice peaks at low frequency and the atomic lattice peaks at high frequency. The red circles indicate the atomic lattice peaks used for Fourier filtering, with the radius corresponding to the filter window used. (c) Real space image resulting from Fourier filtering the (200) and ($\bar{2}00$) Bragg peaks for the field of view shown in (a). (d) An example fit window and sine wave fit for the window outlined in red in (c).

areas with large lattice distortion compared to the average would not be well represented in the fitting and the maximum strain magnitude captured in the analysis would be artificially limited. On the other hand, an overly large window would introduce additional noise in the strain maps or would result in the introduction of artifacts due to the contributions of intensity from neighboring Bragg peaks. We tested a series of window sizes encompassing the aforementioned range and chose the window size above which no additional detail was added to the strain features in the maps and confirmed that this window size did not overlap with any neighboring peaks.

The effect of the filtering step is shown in Figure 2.10c for the **a** direction. We perform the local sine wave fitting procedure for each direction (**a** and **b**) independently by fitting subsets of the two real space Fourier filtered images defined by a grid of small, overlapping windows. One fit window and the resulting sine wave fit are shown in Figure 2.10d. The size of the fitting window was chosen to be ~ 1.5 times the filtered wavelength (*i.e.*, $\sim 5 \text{ \AA}$ for the two {200} Bragg peak pairs), and the overlap between windows was half the window size. Theoretically, the fit windows can overlap as much as one wants (up to the sampling rate of the raw data), but this increases computation time substantially and provides no additional information as strain is only defined for length scales larger than one unit cell. The functional form used for the fit was (Eq. 2.1),

$$f(x, y) = A \sin(\lambda^{-1} \cos(\theta)x + \lambda^{-1} \sin(\theta)y + \phi) \quad (2.1)$$

where A , λ^{-1} , θ , and ϕ are fit parameters extracted for every fitting window. The fit is performed using a non-linear least squares algorithm and comparison with raw data shows the correct local minimum is identified. We then used the λ , spacing, and θ , rotation, maps to compute engineering tensile strain and normalized rotation maps, respectively. Note that this method directly calculates λ and θ , whereas reciprocal space methods first calculate the phase ϕ (with λ and θ fixed), then calculate the strains, which could introduce error or artifacts depending on the quality of the phase retrieval.

For the samples investigated in this work, each Bragg frequency is not consistently present across the field of view, due to both the voids between QDs as well as QDs which are rotated off axis. We therefore first apply an amplitude

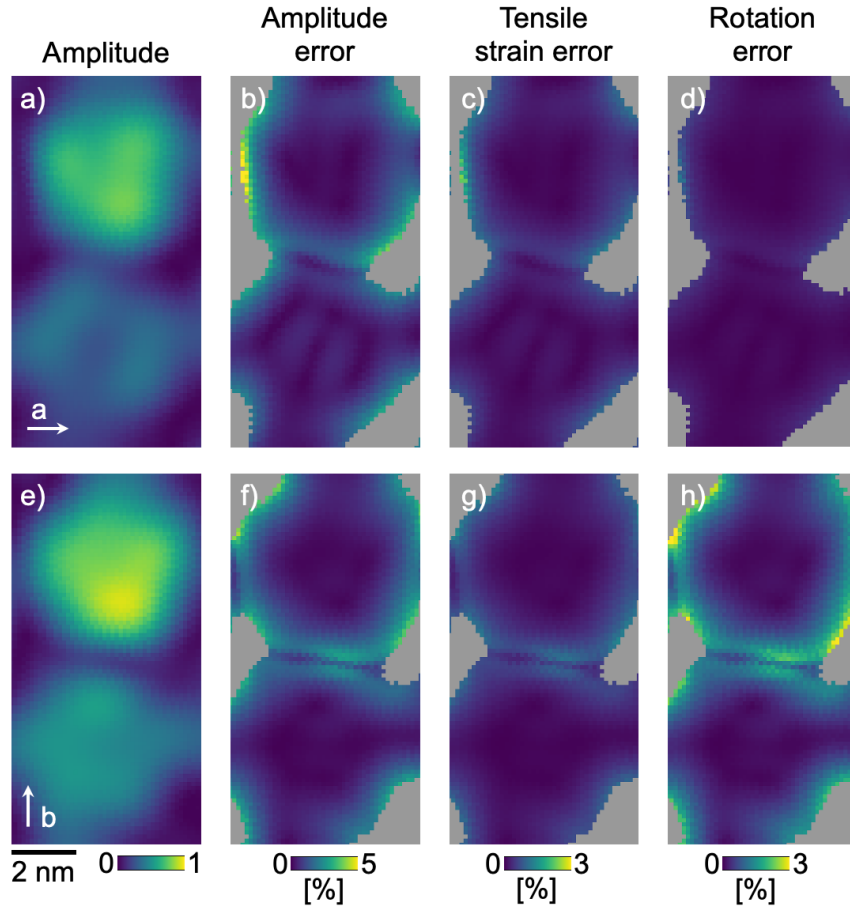


Figure 2.11: Representative examples of error in amplitude, tensile strain, and lattice rotation values extracted using the sine wave fitting method. Examples of extracted amplitude and associated error on the fit parameters for the **a** (a-d) and **b** (e-h) directions. The amplitude maps are shown in (a,e), and (b,f), (c,g), and (d,h) show the error on the amplitude, tensile strain, and rotation values, respectively, presented as a percentage of the fit value. The amplitude maps show the intensity in the neck region is lower than the QD centers, but still significant, and that the error in the fit values remains below a few percent for all three fit parameters. The field of view matches that of Fig. 2.2a.

threshold of one tenth of the maximum amplitude to mask the regions of the image where the frequency is not present. This effectively masks the regions where the fitted spacing and rotation values have no physical significance. The spacing maps are then converted to engineering tensile strain using the simple relation $\epsilon_{nn} = (\lambda_n - \lambda_{n,avg})/\lambda_{n,avg}$, where the subscript n refers to the Bragg frequency it is being applied to. The average spacing, $\lambda_{n,avg}$, is defined as the

average spacing value in the image as masked with a more stringent amplitude threshold, in order to exclude the QD edges and necks where the majority of the strain is present. The rotation maps are simply converted to the deviation from the average rotation value in the map.

Figure 2.11 shows examples of tensile strain and rotation maps alongside maps of the associated standard deviation error presented as a percentage of the fit value. These maps show that the error is well below 1% for most fit windows. The main exception is along the edges of QDs, where the atomic lattice (and therefore the intensity in the filtered image) abruptly ends, naturally decreasing the quality of the fit for windows that include it. A similar argument is true for the highly strained neck between the QDs shown in Figure 2.11. In the neck region, the atomic lattice is less well defined than the centers of the QDs, due to the strain, leading to a reduction in the quality of the fit. However, the error is still significantly lower than the intensity in the tensile strain map. This conclusion holds across the field of view. The ability to estimate the error is another advantage of this method over phase based methods, particularly for this system, which exhibits complex and detailed features which must be delineated from artifacts.

The work presented here is published in [137].

CHAPTER 3

INFLUENCE OF LIGHT ATOMS ON ATOM TRACKING OF CATIONS IN DISTORTED PEROVSKITES WITH ADF-STEM

3.1 Background and theory

With the introduction and proliferation of aberration correction, scanning transmission electron microscopy (STEM) has become an immensely powerful technique for studying the atomic structure of materials. In the field of quantum materials in particular, the ability to resolve subtle atomic displacements at the picometer scale, which can dictate the behavior of the materials, has provided real-space insight into ferroelectric order, periodic lattice distortions and more [147, 92, 97, 52, 99]. In combination with other STEM modalities, high-resolution imaging can help elucidate the connections between charge, spin, lattice, and orbital degrees of freedom in quantum materials.

High-angle annular dark-field (HAADF)-STEM imaging is commonly used for atomic displacement measurements. Due to its strong atomic number (Z) dependence, HAADF-STEM imaging is often considered to be insensitive to light atoms such as oxygen. In atomic columns containing mixtures of heavy and light atoms, however, electron channeling—the behaviour of the electron probe to channel down an atomic column in crystals oriented close to a high-symmetry zone axis—will be affected by both the light and the heavy atoms. The presence of light atoms in such atomic columns can therefore modify the collected signal. Channeling of the electron beam as it travels through a crystal has long been understood to have a strong effect on image contrast, and significant work has been undertaken to better understand the subtleties of its

behavior [151, 76, 63, 157, 80, 89]. In atomic columns that are not coherent or that have close neighboring columns, the channeling behavior can be particularly complex. A recent study combining multislice simulation and experimental ADF-STEM showed that channeling can cause unintuitive contrast in heavy atomic columns that are not coherent based on crystal thickness and lateral separation of atomic sites [162]. Other studies have shown that light species such as oxygen in columns near heavy atomic columns can affect the radial intensity profile and even the shape of the heavy atomic column. [19, 101, 102]. Here, we show experimentally that cation sites in a distorted perovskite oxide crystal can appear displaced by several picometers from their true positions in HAADF-STEM due to coherently displaced oxygen atoms in the same atomic columns. We then elucidate the channeling behavior that causes the apparent displacement using multislice simulations and consider ways to mitigate or avoid the artifact.

3.2 Results and discussion

Experimental HAADF-STEM imaging was performed using accelerating voltages of 120 and 300 kV, with 21.4 and 30.3 mrad convergence angles, respectively. Imaging was performed on a Thermo Fisher Scientific (TFS) Titan Themis and a TFS Spectra 300 X-CFEG. Electron transparent TEM lamellas of rhombohedral lanthanum nickelate (LaNiO_3) were prepared using a TFS Helios G4 X focused ion beam (FIB) from a bulk single crystal synthesized using a recently reported high oxygen pressure floating zone method [167]. See Section 3.3 for full experimental details.

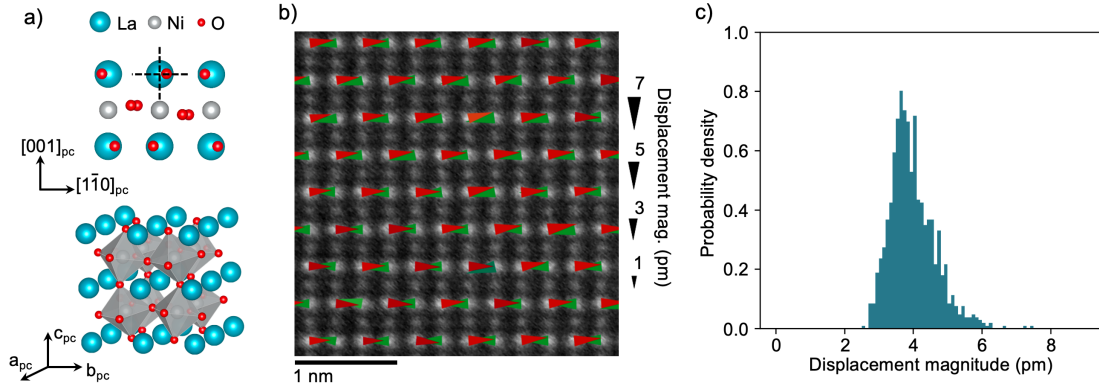


Figure 3.1: Atom tracking in HAADF-STEM imaging of the $[110]_{pc}$ zone axis of LaNiO_3 , showing a consistent displacement patterning with ~ 3.7 pm displacements. (a) Crystal structure of LaNiO_3 showing coherent oxygen atom displacements with respect to the lanthanum atoms in the $[110]_{pc}$ projection. (b) HAADF-STEM image acquired using an accelerating voltage of 120 kV, with overlaid arrows representing the measured displacements of lanthanum-oxygen atomic columns with respect to the crystallographic positions of the lanthanum atoms. (c) Histogram of lanthanum-oxygen column displacements as shown in (b) for a $12 \text{ nm} \times 12 \text{ nm}$ field of view.

Figure 3.1a shows a three-dimensional model of LaNiO_3 and the same model projected down a $[110]$ pseudocubic (pc) axis. In each lanthanum-oxygen column of the $[110]_{pc}$ projection, the oxygen sites are coherently displaced by 35 pm with respect to the lanthanum sites in the plane of the projection. The naive assumption that HAADF-STEM is insensitive to oxygen would suggest that the lanthanum columns would appear at their expected crystallographic positions, unaffected by the relatively displaced oxygen atoms. Experimentally, we find that this is not the case. An HAADF-STEM image of LaNiO_3 in the $[110]_{pc}$ orientation is shown in Figure 3.1b. The overlaid arrows, which indicate the measured displacement of each lanthanum column from its true lattice position, show that there is a distinct shift due to the presence of the coherently displaced oxygen atoms as will be shown below. The displacements were extracted using an atom-tracking technique developed for the study of periodic lattice displacements (see Section 3.3.1) [132]. A histogram of the displacement magnitudes is

included in Figure 3.1c, showing an average apparent displacement of 3.7 pm.

To understand the origin and details of these apparent displacements, the propagation of the electron wave function through the LaNiO_3 crystal was simulated using the frozen-phonon multislice method [27, 49, 75]. All simulations were carried out using the TEMSIM simulation package [74] with 20 frozen phonon configurations. Figure 3.2a shows a cross-section of the probe intensity as a function of depth through the crystal for a probe positioned on the lanthanum column. The positions of the lanthanum and oxygen columns are shown at the top of the panel. There is a visible shift in the probe intensity from the lanthanum position toward the oxygen position as the probe propagates within the first few nanometers of the crystal.

This shift is made clearer in Figure 3.2b, which shows the difference between the cross-section in Figure 3.2a and the perpendicular cross-section for which the lanthanum and oxygen atoms are aligned horizontally in the plane of the cross-section. Since the HAADF-STEM intensity produced by an atom is proportional to the electron probe intensity at that atom position, this shift means the collected intensity for a probe positioned on the lanthanum column will be reduced by the presence of the displaced oxygen atoms. Similarly, for a probe positioned 35 pm from a lanthanum column on the oxygen column, the presence of the oxygen atoms allows the probe intensity to channel onto the lanthanum column more effectively than for a probe positioned 35 pm from the lanthanum column in the opposite direction.

This more complete picture is explored in Figure 3.3, showing probe intensity simulations performed for three probe positions as indicated in Figure 3.3a. As stated above, for a probe positioned directly on the lanthanum column,

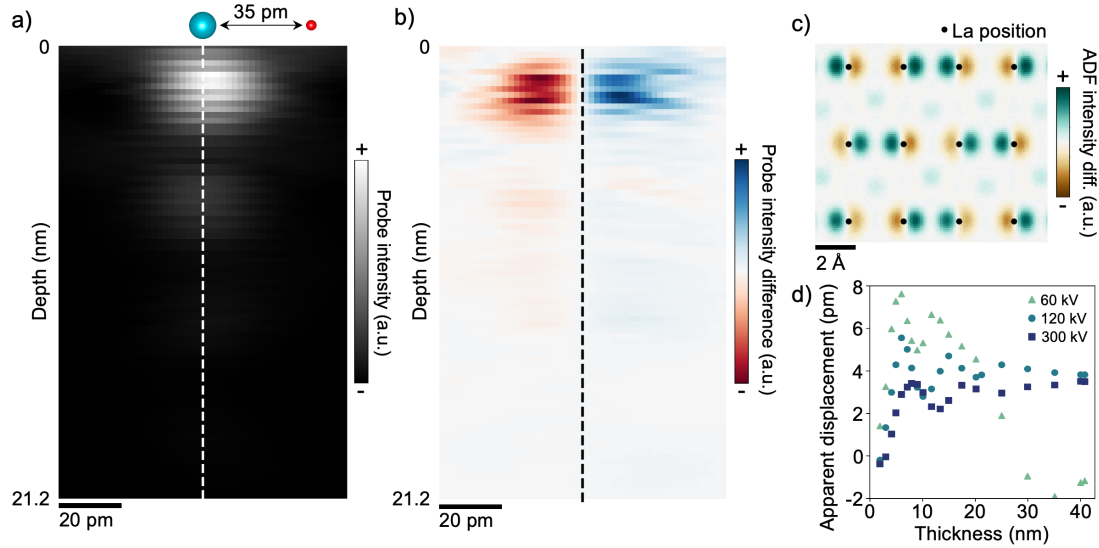


Figure 3.2: Probe intensity and HAADF-STEM image simulations for the $[110]_{pc}$ zone axis of LaNiO_3 . (a) cross-section of the simulated probe intensity as a function of crystal depth for a probe centered on a lanthanum column in $[110]_{pc}$ -oriented LaNiO_3 with an accelerating voltage of 120 kV. The white dashed line represents the initial probe position, and the lanthanum and oxygen positions are shown at the top. (b) Difference between the probe intensity cross-section in a and the perpendicular cross-section in which the lanthanum and oxygen atoms are aligned horizontally when projected onto the plane. The difference map shows a clear shift in probe intensity toward the oxygen atoms as the electron beam propagates through the crystal. (c) Difference between simulated HAADF-STEM images of LaNiO_3 with and without oxygen atoms included, showing the oxygen atoms cause a shift in the HAADF signal off the crystallographic lanthanum positions and toward the oxygen positions. (d) Lanthanum displacement as a function of crystal thickness measured from simulated HAADF-STEM images for accelerating voltages of 60, 120, and 300 kV, showing that a higher accelerating voltage reduces the apparent lanthanum displacements for nearly every thickness. Note the behavior above ~ 20 nm for 60 kV is more complicated, likely due to guaranteed multiple scattering.

there is a shift in intensity toward the displaced oxygen atoms (Figure 3.3c). For probes positioned 35 pm from the lanthanum column, on the oxygen column (Figure 3.3d) and 35 pm in the opposite direction of the oxygen column (Figure 3.3b) there is a dramatic shift of probe intensity onto the much heavier lanthanum column. For the former, the shift appears to be stronger, facilitated by the presence of the displaced oxygen atoms. This effect is made clearer by line profiles of the probe intensity and integrated probe intensity with thickness

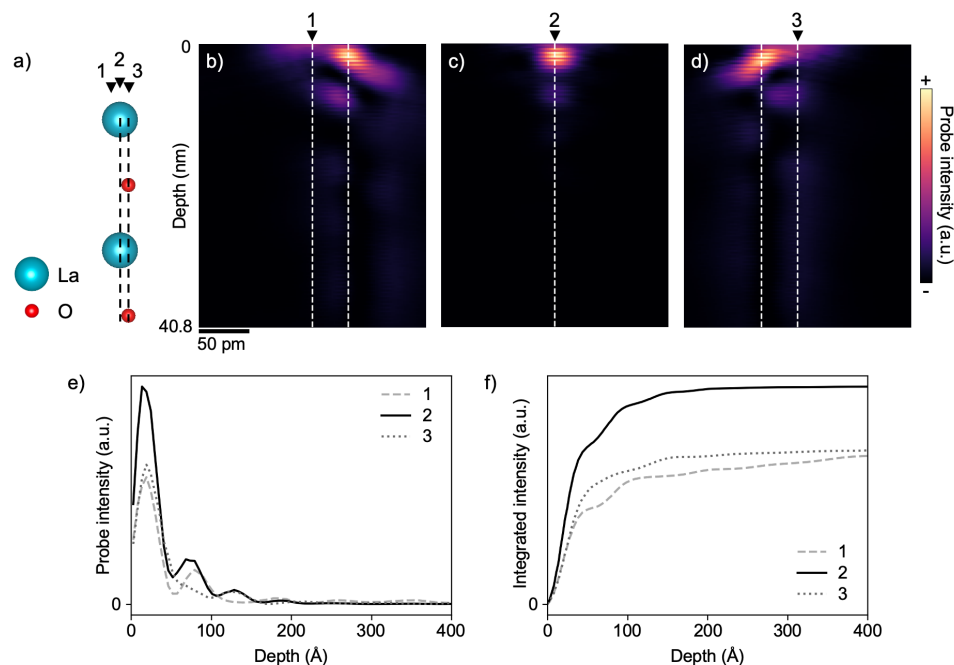


Figure 3.3: Probe intensity simulations for three probe positions around the shared lanthanum-oxygen columns. (a) Model of a single lanthanum-oxygen column. (b-d) Simulated cross-sections of probe intensity vs. depth for probes positioned at points 1, 2, and 3 as shown in a, respectively. Position 2, c, is on the lanthanum column, position 3, d, is 35 pm from position 2 on the oxygen column, and position 1, b, is 35 pm from position 2 in the opposite direction of the oxygen column. (e) Probe intensity profiles along the lanthanum column for all three probe positions. (f) Integrated probe intensity profiles for each probe position, showing the total intensity on the lanthanum column is greater for the probe positioned on the oxygen column compared to opposite the oxygen column at all thicknesses.

on the lanthanum column for all three probe positions as shown in Figure 3.3e and f. These profiles show that the total intensity on the lanthanum column is greater for the probe positioned on the oxygen column than for the probe positioned 35 pm in the opposite direction. Thus, while the presence of displaced oxygen atoms results in a reduction of the probe intensity on the lanthanum column for a probe positioned on that column, they also cause an increase in intensity on the lanthanum column for a probe positioned on the oxygen column (at least for typical sample thicknesses used for atom-tracking in STEM). As the collected HAADF-STEM intensity is proportional to the probe intensity

on the lanthanum column, these effects both contribute to the apparent shift in the shared lanthanum-oxygen column position in the final HAADF-STEM image. Taken together, these probe intensity simulations indicate that an HAADF image of LaNiO_3 oriented as shown in Figure 3.1a should show lanthanum positions shifted with respect to their true positions as was measured experimentally.

Indeed, this result is confirmed by full image simulations. Figure 3.2c shows the difference between a simulated HAADF-STEM image of $[110]_{\text{pc}}$ -oriented LaNiO_3 and a simulated image of the same structure with all oxygen atoms removed. The positive (blue) intensity next to each lanthanum position matches the displacement direction of the oxygen atoms in the column. The measured displacement of the lanthanum-oxygen columns with respect to the true lanthanum positions is plotted as a function of thickness in Figure 3.2d. At 120 kV, the apparent displacement increases sharply in the first 5 nanometers of the crystal and then oscillates in accordance with the channeling signal, finally flattening out at a thickness of around 40 nm. Note the experimentally measured displacement, 3.7 pm, is well within the range of displacements measured from simulation.

While the displacements measured from both simulation and experiment are significantly lower than the actual displacement of the oxygen sites, 35 pm, they are on the order of periodic lattice displacements measured in quantum materials such as $\text{LuFe}_2\text{O}_{4+\delta}$ and $\text{Bi}_{1-x}\text{Sr}_{x-y}\text{Ca}_y\text{MnO}_3$ [33, 9]. It is therefore crucial to understand the possible effects of such coherent displacements when attempting to quantify the lattice modulations in such structures.

In some distorted perovskite structures, the symmetry is such that no orien-

tation will contain coherently displaced oxygen atoms in shared metal-oxygen columns, and in other structures, careful choice of the zone axis can allow one to avoid these channeling artifacts. For any $\langle 100 \rangle$ -type zone axis, there will necessarily be no metal-oxygen columns with coherently displaced oxygen atoms since these orientations are parallel to the axes of the octahedra. For $\langle 110 \rangle$ -type zone axes, whether a particular crystal contains coherently displaced oxygen atoms is dictated by the tilt system of the oxygen octahedra as defined by Glazer notation [43, 44]. Any structure with a tilt system comprising only zero or positive sense tilts, for example: $a^0a^0c^+$ or $a^+b^+b^+$, will have no zone axes with coherently displaced oxygen atoms. On the other hand, any structure with a tilt system containing one or more negative sense tilts will have zone axes with coherently displaced oxygen sites. In particular, any negative sense tilt axis will lead to coherently displaced oxygen sites along any zone axis not orthogonal to the negative sense tilt axis. For example, in a structure with a $a^0a^0c^-$ tilt system, the $[101]$, $[10\bar{1}]$, $[011]$, and $[01\bar{1}]$ pseudocubic zone axes will have coherently displaced oxygen atoms.

Examples of tilt systems with and without coherently displaced oxygen atoms in metal-oxygen columns are depicted in Figure 3.4 in perspective view as well as oriented down $[001]_{pc}$ and $[101]_{pc}$ zone axes. In each structure, octahedra are colored according to their direction of rotation. In the model for tilt system $a^0a^0c^+$, shown in the left column, the rotations of successive octahedra along the $[001]_{pc}$ zone axis are matching, which leads to successive octahedra along the $[101]_{pc}$ zone axis to be opposite, ensuring there are no coherently displaced oxygen atoms along that zone axis. The opposite is true for the $a^0a^0c^-$ tilt system shown in the right column. Here the octahedra match tilt direction in columns along the $[101]_{pc}$ zone axis, and thus the oxygen atoms are displaced

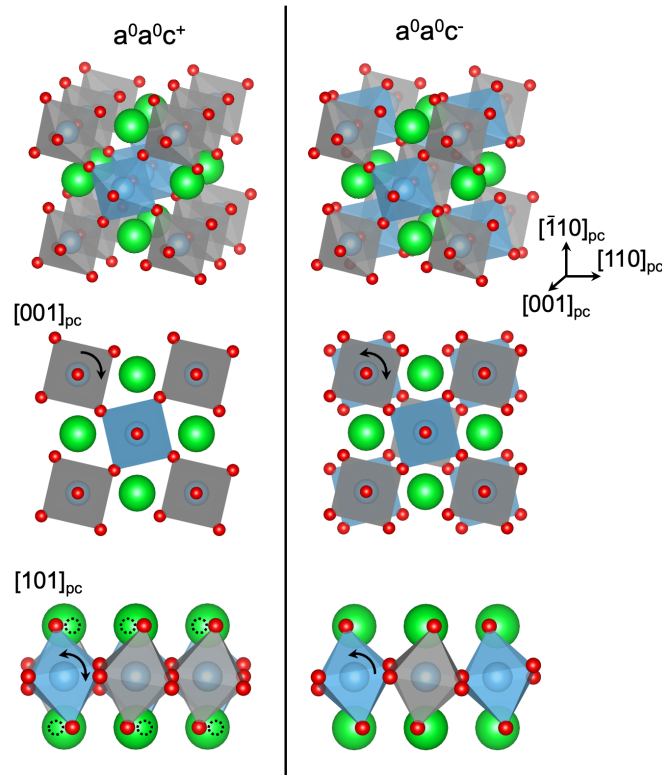


Figure 3.4: Examples of $a^0a^0c^+$ and $a^0a^0c^-$ tilt systems in perspective view as well as projected down their $[001]_{pc}$ and $[101]_{pc}$ zone axes. Oxygen octahedra are colored according to their rotation direction (gray - clockwise, blue - counterclockwise). For the $a^0a^0c^+$ tilt system, the oxygen octahedra alternate their rotation direction along the $[101]_{pc}$ direction, while in the $a^0a^0c^-$ tilt system, the octahedral rotations are aligned in that direction, leading to coherently displaced oxygen atoms in lanthanum-oxygen columns.

coherently along that axis.

In structures where a desired measurement requires data to be taken along a zone axis with coherently displaced oxygen atoms in metal-oxygen columns, the apparent displacement due to the oxygen atoms can be reduced by working at a higher accelerating voltage. This is observed experimentally as shown in Figure 3.5a and b. Figure 3.5a shows an experimental image analogous to that shown in Figure 3.1a, but acquired at 300 kV and overlaid with the measured displacements of the lanthanum-oxygen columns. A histogram of these

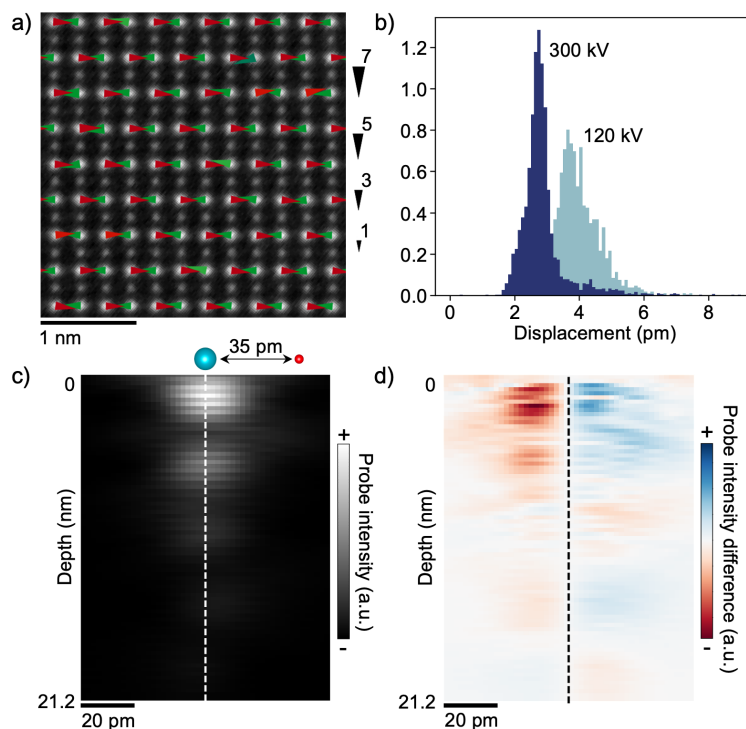


Figure 3.5: Experimental and simulated HAADF-STEM data showing the magnitude of the channeling artifact is less severe at an accelerating voltage of 300 kV. (a) Experimental HAADF-STEM image acquired using a 300 kV accelerating voltage, with overlaid arrows representing the measured displacements of lanthanum-oxygen atomic columns with respect to the crystallographic positions of the lanthanum atoms. (b) Histogram of lanthanum-oxygen displacements as shown in a for a 20 nm \times 20 nm field of view, with the histogram of displacements at 120 kV from Fig. 3.1b included for comparison. (c,d) cross-section of the simulated probe intensity (c) and difference between the probe intensity cross-section in c and the perpendicular cross-section (d) for a probe positioned on a lanthanum column at 300 kV.

displacements is presented in Figure 3.5b along with the histogram for 120 kV, showing that the average apparent displacement is decreased from 3.7 pm at 120 kV to 2.8 pm at 300 kV.

This dependence on voltage was also confirmed through simulations. Similar to Figure 3.2a, Figure 3.5c shows a cross-section of the probe intensity through the lanthanum-oxygen column as a function of depth for a probe positioned on the lanthanum column, and Figure 3.5d shows the difference between

that cross-section and the perpendicular cross-section in which the lanthanum and oxygen columns are aligned in the plane of the cross-section. The shift in probe intensity visible in Figure 3.5c and d is clearly less than that in Figure 3.2a and b. The voltage dependence is further confirmed by the simulated apparent displacement versus depth curves shown in Figure 3.2d for 60, 120, and 300 kV, wherein the displacement decreases with increasing voltage consistently for nearly all thicknesses. At both 120 and 300 kV, the channeling oscillations flatten out by ~ 40 nm. At 60 kV, the channeling behavior is more complex for thicknesses greater than ~ 25 nm, likely due to the guaranteed multiple scattering at those thicknesses.

At an accelerating voltage of 60 kV the trend in apparent atomic column displacement with sample thickness is consistent with the trends found at 120 and 300 kV up until a thickness of ~ 25 nm. At that point, the trend deviates substantially, ultimately exhibiting displacements in the opposite direction at thicknesses greater than 30 nm, as shown in Figure 3.2d. This unexpected behavior is likely due to multiple scattering effects.

For elastic scattering in elemental solids, the mean free path, λ_{el} , is given by:

$$\lambda_{el} = \frac{A}{N_0 \sigma_{el} \rho}$$

where A is the atomic weight of the material, N_0 is Avogadro's number, and ρ is the density. The elastic scattering cross section, σ_{el} , can be estimated by,

$$\sigma_{el} = \frac{1}{\pi} Z^{4/3} \lambda_{el}^2 (1 + E/E_0)^2$$

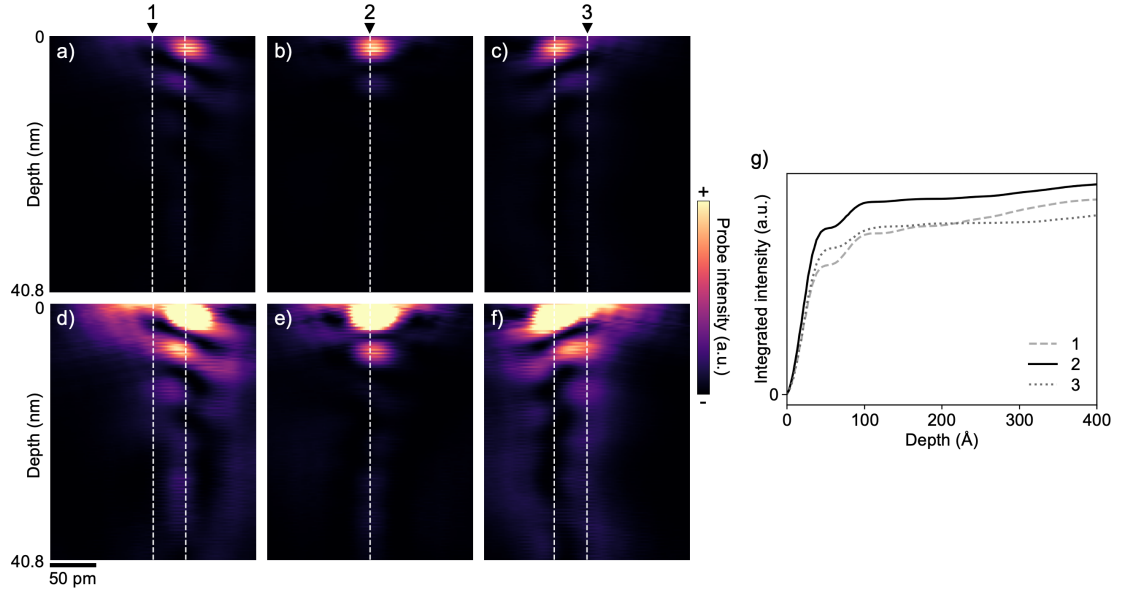


Figure 3.6: Probe intensity simulations for a 60 kV probe showing anomalous behaviour for thick samples due to multiple scattering effects. (a-f) Simulated cross-sections of probe intensity vs. depth for a 60 kV probe positioned at points 1 (a,d), 2 (b,e), and 3 (c,f) as shown in Fig. 3.3a. The intensity in panels d-f has been saturated to better show the probe intensity distribution at high thicknesses. (g) Integrated probe intensity along the lanthanum column for each probe position, showing a crossover point where the integrated intensity for a probe positioned opposite the oxygen column becomes greater than that for the probe positioned on the oxygen column.

according to the Wentzel atom model, where Z is the atomic number, λ is the wavelength of the electron probe, E is the incident electron energy and E_0 is the electron rest energy (511 keV) [37]. Here, composition-weighted averages were used for the atomic weight and number. The dependence on the atomic number has been shown to vary experimentally between $Z^{4/3}$ and $Z^{3/2}$ for metallic alloys [168]. The elastic scattering mean free path of LaNiO_3 at 60 kV can therefore be estimated at 12.3 - 20.5 nm, guaranteeing multiple scattering at larger thicknesses. This is consistent with multiple scattering effects being the primary factor in the deviation of the apparent displacement versus thickness trend after 20 nm.

To further confirm that the unexpected displacement trend is inherent to the

scattering behavior and not an effect of the fitting procedure, the full probe intensity distribution as a function of thickness was simulated for a 60 kV probe for the same three probe positions as in Figure 3.3a. cross-sections of those simulations are shown in Figure 3.6a-f where for sample thicknesses $> \sim 20$ nm the probe intensity is relatively low on the La column for the probe positioned on the oxygen column (Figure 3.6c and d) as compared to the probe positioned opposite the oxygen column (Figure 3.6a and d). This comparison is further clarified in the integrated probe intensity curves shown in Figure 3.6g, where a crossover in the total intensity on the lanthanum column is observed for the probe positions on and opposite the oxygen column at ~ 22 nm.

Even at 300 kV, the apparent displacements due to coherently displaced oxygen atoms are non-negligible. Therefore, care should be taken when interpreting atomic position measurements for such data. Additionally, simulations could be used in combination with thickness measurements and precise atom tracking to help disentangle the effects of cation and anion displacements. Incorrect displacements of cation sites have also been observed resulting from specimen mistilt in combination with differing channeling strength in neighboring columns of different atomic species [29]. Specimen mistilt would also likely affect the magnitude of the apparent displacements due to coherently displaced oxygen atoms.

In summary, we have shown through experiment and simulation that HAADF-STEM images of distorted perovskites can exhibit anomalous atomic positions for mixed cation-anion columns containing coherently displaced anions due to electron channeling effects from the much lighter anions. We have demonstrated that the magnitude of the apparent displacement from the crys-

tallographic position depends on the probe accelerating voltage and the crystal thickness. It is likely also affected by additional imaging parameters such as convergence angle and specimen mistilt. These apparent displacements can be comparable to the magnitudes of lattice modulations associated with quantum phenomena such as charge density waves. Given the recent increased interest in these phenomena and in precise atomic-position measurements enabled by aberration-corrected STEM, it is crucial to remain cognizant of this effect and to consider avenues to avoid or reduce its impact.

3.3 Methods

Bulk single crystals of LaNiO_3 were synthesized via a high pressure floating zone method as described by Zhang et al. [167]. Electron transparent TEM samples were prepared using the standard focused ion beam (FIB) lift out procedure with a Thermo Fisher Scientific (TFS) Helios G4 X FIB. Lamellas were thinned to approximately 20 - 30 nm, and a final polish was performed at 2 kV to reduce surface damage and redeposition. Imaging was performed using an FEI (now TFS) Titan Themis and a TFS Spectra 300 X-CFEG operating at 120 and 300 kV with convergence semi-angles of 21.4 and 30.0 mrad, respectively.

3.3.1 Atomic displacement mapping

Picometer-scale displacements of atomic columns were quantified using a method developed for the analysis of periodic lattice displacements and explained in detail elsewhere [132]. Briefly, the half-order peaks present in the

Fourier transform of the $[110]_{\text{pc}}$ -oriented HAADF-STEM images, which are associated only with the displacements of oxygen atoms with respect to the ideal cubic lattice, were identified and damped to the background level by fitting them with 2D Gaussian functions. The inverse Fourier transform was calculated, creating a reference image with the oxygen-induced displacements removed. The displacement of each lanthanum-oxygen column was then extracted by fitting all atomic columns in both the original and reference images and calculating the difference in each column position. We additionally confirmed the accuracy of this analysis by calculating the lanthanum-oxygen column displacements from the relative fit positions of adjacent columns, which produced consistent results.

3.3.2 Multislice simulations

High-angle annular dark-field (HAADF) images and full probe simulations were carried out using the multislice method [27, 49, 75] implemented in the TEMSIM simulation package [74]. Phonon scattering was modeled using the frozen-phonon approximation [90, 60, 103]. Multislice simulations were performed for a series of 20 phonon configurations and the results were averaged incoherently. The probe was defined with a defocus of 0 nm, a spherical aberration coefficient of $1 \mu\text{m}$, and a convergence semi-angle of 21.4 mrad unless otherwise specified. The $(110)_{\text{pc}}$ oriented LaNiO_3 supercell was defined with dimensions $50.7 \times 46.4 \text{ \AA}$ to prevent wrapping errors due to the rhombohedral lattice. Simulations of the probe intensity evolution with sample depth were calculated using $4096 \times 4096 \text{ pixel}^2$ transmission and probe wave functions resulting in a maximum scattering angle of 1310 mrad. HAADF-STEM images

were simulated using 2048×2048 pixel² transmission and probe wave functions resulting in a maximum scattering angle of 451 mrad. A scan step size of 0.1 Å and inner and outer collection angles of 68 and 300 mrad, respectively, were used.

CHAPTER 4
DISENTANGLING THE STRUCTURE OF OXYGEN VACANCY
ORDERED DOMAINS IN $\text{LaNiO}_{3-\delta}$

4.1 Background

Rare earth perovskite nickelates (RNiO_3) are well known to exhibit electronic and magnetic transitions as a function of temperature [142, 95]. The origins of these transitions have been the subject of intense investigation with regard to correlation effects in charge, spin, lattice and orbital degrees of freedom [50, 67, 148, 83, 18, 3, 94, 82, 35, 98, 118]. Structural transitions ($Pbnm$ to $P2_1/n$) occur simultaneously with metal to insulator phase transitions upon cooling, with the transition temperature varying with the R^{3+} ionic radius [25]. The exception is LaNiO_3 ($\text{R} = \text{La}$), which remains metallic and paramagnetic at all temperatures.

Oxygen deficient compounds ($\text{LaNiO}_{3-\delta}$), however, have been shown to exhibit more complicated electronic and magnetic behavior including ferro- and antiferromagnetism. Specifically, as the oxygen vacancy concentration, δ , is increased from 0 to 0.5, the compound undergoes a metal to insulator transition [128]. For $\delta = 0.25$ and 0.5, the compound is ferro- and antiferromagnetic, respectively, at low temperature [100]. These property changes are linked to regions of ordered oxygen vacancies, where the apical oxygen atoms of each oxygen octahedron are missing from every fourth or second $(110)_{\text{pc}}$ plane in the $\delta = 0.25$ and 0.5 phases, respectively [45]. Detailed investigation of the structure and properties of these oxygen vacancy ordered phases has proven difficult, however, because the phases tend to coexist on length scales of hundreds of nanometers [153]. For example, while the structure of the $\delta = 0.5$ phase was refined by neu-

tron diffraction in 1997 [4], to my knowledge, the structure of the $\delta = 0.25$ phase has not been reported. Additionally, the magnetic transitions for the two ordered structures have been reported at a range of temperatures and are often described as quite broad, likely due to structural heterogeneity. There is, therefore, a need for a nanoscale probe to both directly investigate that heterogeneity and to extract information from the distinct phases.

In this study, I mapped the domain distribution of the $\delta = 0.25$ and 0.5 phases in an oxygen deficient $\text{LaNiO}_{3-\delta}$ bulk single crystal using nanobeam 4D scanning transmission electron microscopy (4D-STEM). Having separated the phases of interest, I employed picometer-scale HAADF-STEM atom tracking to extract the atomic displacement patterns associated with each phase. This work thus provides a direct picture of the structural heterogeneity that exists in these oxygen vacancy ordered crystals and elucidates the effect of the vacancy ordering on the cation sublattice.

4.2 Results and discussion

High-angle annular dark-field (HAADF) scanning transmission electron microscopy (STEM) imaging and 4D-STEM measurements were performed on a Thermo Fisher Scientific (TFS) Titan Themis operating at 120 kV. HAADF-STEM images were acquired with a 21.4 mrad convergence angle and 68 mrad inner collection angle, and nanobeam electron diffraction (NBED) 4D-STEM data sets were acquired in microprobe mode with 0.43-0.55 mrad convergence angles using the EMPAD pixelated detector. STEM specimens of oxygen deficient $\text{LaNiO}_{3-\delta}$ were prepared using a TFS Helios G4 X focused ion beam (FIB) from

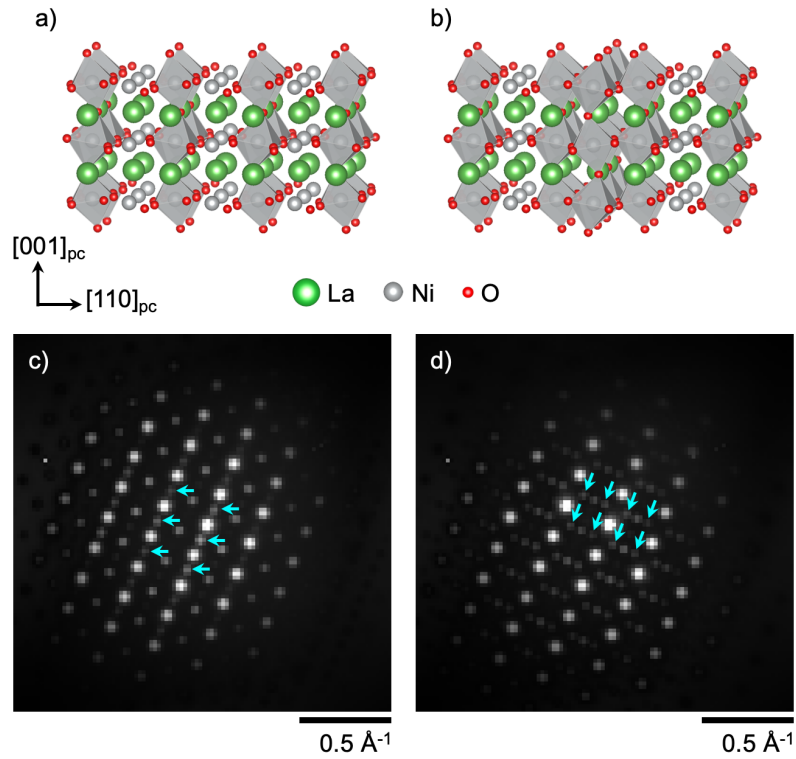


Figure 4.1: Vacancy ordering and summed NBED patterns for the $\delta = 0.5$ (a,c) and 0.25 (b,d) phases of $\text{LaNiO}_{3-\delta}$. (a,b) Atomic models showing the positions of the oxygen vacancies at the apical positions of the oxygen octahedra in every second and fourth $(110)_{\text{pc}}$ plane for the $\delta = 0.5$ and 0.25 phases, respectively. All atom positions are those of the stoichiometric LaNiO_3 phase for simplicity. (c,d) Summed NBED patterns for the $\delta = 0.5$ and 0.25 phases, respectively. The NBED patterns were first filtered using EWPC analysis to reduce effects from tilt and thickness variations and then summed over the vacancy-ordered domains. The superlattice reflections associated with each phase are visible in the NBED patterns, and a few peaks are pointed out in each.

bulk single crystals synthesized using a recently reported high oxygen pressure floating zone method [167, 170]. The as-grown crystal boules exhibit a radial gradient in the oxygen vacancy concentration, decreasing with radius. Samples for subsequent FIB lamella preparation were extracted from the center, where the oxygen vacancy concentration was relatively high.

We first assess the distribution of oxygen vacancy ordered domains using nanobeam 4D-STEM by summing the intensity of the superlattice reflections

associated with the $\delta = 0.5$ and 0.25 phases. These reflections have been identified by previous x-ray and electron diffraction studies [4, 45, 100]. In the $\delta = 0.5$ phase, vacancies are present in the apical oxygen positions in every second $(110)_{\text{pc}}$ crystallographic plane as shown in Figure 4.1a, giving rise to half-integer superlattice reflections in the $[110]_{\text{pc}}$ and $[001]_{\text{pc}}$ directions. These reflections are present in the EWPC filtered (see methods, Section 4.3.1) NBED pattern in Figure 4.1c, though those along the $[110]_{\text{pc}}$ direction are relatively faint. The $\delta = 0.25$ phase contains vacancies at the same apical oxygen positions but only in every fourth $(110)_{\text{pc}}$ plane (Figure 4.1b). Thus, associated superlattice peaks appear at the quarter- and half-integer positions along the $[110]_{\text{pc}}$ direction as evident in Figure 4.1d. The half-integer reflections along the $[110]_{\text{pc}}$ direction are associated with both vacancy-ordered phases and are therefore excluded from the superlattice intensity maps for both phases (even though they appear relatively faint in both cases) for better clarity.

Figure 4.2 shows the domain distributions mapped over two ~ 600 nm fields of view. The contrast in the maps for the $\delta = 0.25$ phase (Figure 4.2c and f) shows distinct and sharp domains in both fields of view. The domains are irregularly shaped and ~ 100 - 400 nm in size. The maps of the $\delta = 0.5$ phase (Figure 4.2b and e) also show distinct domains, ~ 100 - 400 nm in size, but the boundaries are less well defined in some places, particularly in the field of view shown in panel b. This may be due to the $\delta = 0.5$ domains being smaller, causing the electron probe to project through stoichiometric LaNiO_3 lattice in addition to a vacancy-ordered domain, thus reducing the intensity of the half-integer diffraction disks. There are also some $\delta = 0.5$ domains in panel b that appear needle-like in shape. It is possible that these needle-like domains are in fact plate-like domains that extend along the projection axis. Extending this thought experiment could then

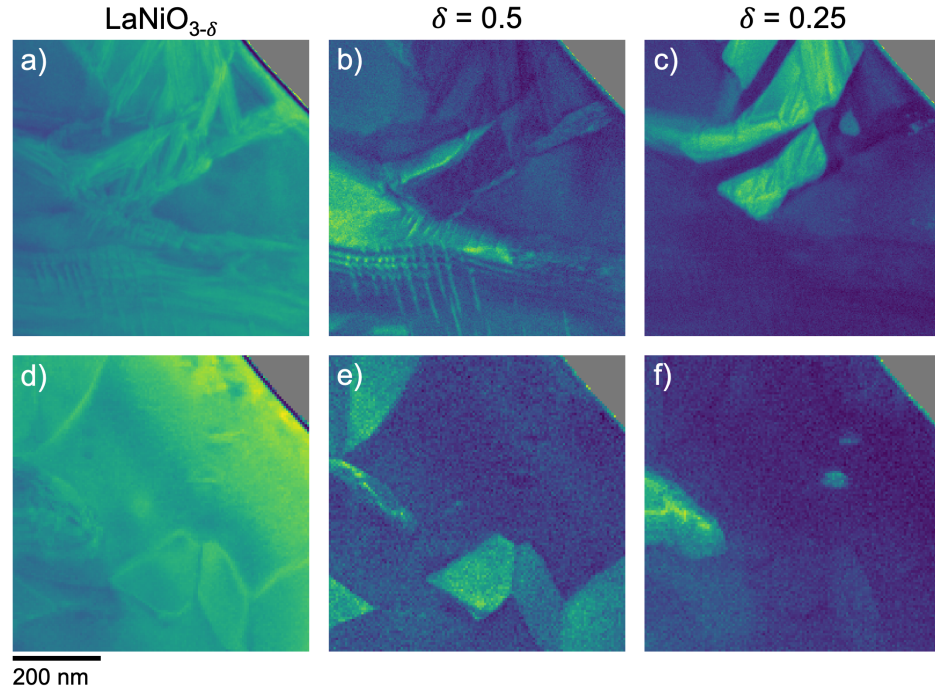


Figure 4.2: Domain mapping of the $\delta = 0.5$ and 0.25 phases of $\text{LaNiO}_{3-\delta}$ with 4D-STEM. Maps of $\delta = 0.5$ (b,e) and 0.25 (c,f) domain distributions for two regions of crystal. Bragg intensity maps for each region are presented in a,d showing the overall domain distribution. b,e and c,f map the summed intensities of the Bragg reflections associated with the $\delta = 0.5$ and 0.25 vacancy-ordered phases, respectively. The NBED 4D-STEM data sets were filtered using EWPC analysis to reduce the effect of tilt and thickness variations across the ~ 600 nm fields of view.

mean that the low contrast but wider domains are caused by stacking of these plate-like domains in the projection direction, resulting in mixed intensity from LaNiO_3 and $\text{LaNiO}_{2.5}$ phases. Simulations could give insight to whether this is an energetically favorable geometry for domain wall formation.

Once the domain distributions of the oxygen deficient phases were identified, atomic-resolution HAADF-STEM imaging was performed to investigate the cation displacement patterns induced by the vacancy-ordered structures. The displacement patterns of the lanthanum and nickel columns in the $[\bar{1}10]_{\text{pc}}$ projection were extracted as shown in Figure 4.3 using an atom tracking technique as discussed in Section 3.3.1 [132]. The displacements associated with the

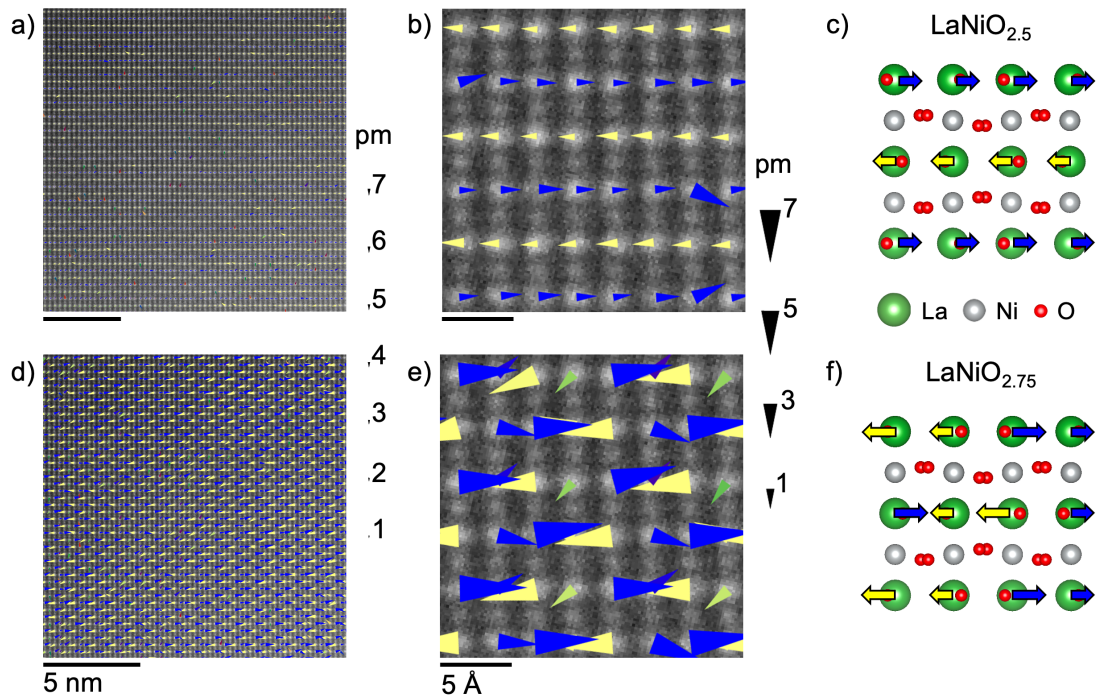


Figure 4.3: Atomic column displacements mapped for lanthanum along the $[\bar{1}10]_{pc}$ projection of $\text{LaNiO}_{3-\delta}$. (a,d) Displacements associated with the $\delta = 0.5$ and 0.25 phases, respectively, over a ~ 15 nm field of view. A subset of a(d) is presented in b(e), more clearly displaying the displacement pattern. An atomic model of $[\bar{1}10]_{pc}$ -oriented LaNiO_3 is shown in c and f overlaid with arrows indicating the displacement patterns for the $\delta = 0.5$ and 0.25 phases. The arrow size indicates the magnitude, and the arrow direction and color indicate the direction of the displacement for each atomic column.

$\delta = 0.5$ phase were extracted from the half-ordered peaks along the $[001]_{pc}$ direction, and the displacements associated with the $\delta = 0.25$ phase were extracted from the quarter-ordered peaks along the $[110]_{pc}$ direction. The half-ordered peaks along the $[110]_{pc}$ direction were not used, as they are associated with both phases. I note, however, that inclusion of those peaks did not significantly affect the direction or magnitude of extracted displacements for either phase. The displacement magnitudes for the nickel columns were below the noise floor of the measurement for both phases and were thus excluded for clarity. Figure 4.3a and d show the displacements associated with the $\delta = 0.5$ and 0.25 phases, respectively, over a ~ 15 nm \times 15 nm field of view. The arrow size indicates

the magnitude of displacement, and the arrow direction and color indicate the direction of the displacement for each atomic column. The displacement patterns appear consistent over the field of view in both cases, indicating that the displacements are intrinsic to the material. Indeed, the displacement pattern for the $\delta = 0.5$ phase matches the structure published in 1997 [4]. To my knowledge, the cation structure of the $\delta = 0.25$ phase has not been previously published. As seen in the magnified subsets of Figure 4.3 panels a and d shown in panels b and e, the pattern for the $\delta = 0.5$ phase consists of displacements in the $[110]_{\text{pc}}$ and $[\bar{1}\bar{1}0]_{\text{pc}}$ directions in alternating lanthanum layers along the $[001]_{\text{pc}}$ direction. The pattern for the $\delta = 0.25$ phase is more complicated, including alternations in both the size and direction of the displacements, though the directions are still primarily along the $[110]_{\text{pc}}$ and $[\bar{1}\bar{1}0]_{\text{pc}}$ lattice vectors. In both phases, the nickel sites were found not to exhibit significant displacements and thus were excluded from the displacement maps.

Note, while 4D-STEM analysis revealed distinct domains of the $\delta = 0.5$ and 0.25 phases, the region imaged for subsequent atom tracking analysis contained superlattice intensity from both phases. This is likely due to the electron beam projecting through multiple domains, a situation that would be particularly feasible in the case of thin plate-like $\delta = 0.5$ domains as discussed above. This is also reflected in the magnitude of the displacements measured for the $\delta = 0.5$ domain, which are significantly lower than those expected from the published structure (~ 1 pm compared to 4.6 pm) [4]. This makes sense given the electron beam is scattered by lanthanum atoms in the displaced positions of the $\delta = 0.5$ domain as well as the positions of the $\delta = 0.25$ (and perhaps $\delta = 0$) domain(s). The image contrast would thus reflect the combination of lanthanum positions in those phases. The exact positions must depend on both the volume fraction of

the phases and their arrangement along the zone axis, which will affect electron channeling behavior. The precise magnitude of the $\delta = 0.25$ phase displacements are likely also lower than the true values, though the relative magnitudes and the pattern within that phase should be accurate.

In conclusion, domain mapping with nanobeam 4D-STEM revealed distinct domains of both the $\delta = 0.5$ and 0.25 vacancy-ordered $\text{LaNiO}_{3-\delta}$ phases over several hundred nanometers of crystal. Most domains were irregularly shaped and a few hundred nanometers in size. The $\delta = 0.5$ domain maps also contained some needle-like domains, which I suggest may in fact be plate-like, extending in the projection direction. Atom tracking subsequently revealed the picometer-scale atomic displacement pattern for each phase in the $[\bar{1}10]_{\text{pc}}$ projection. The extracted displacement patterns confirm the previously published structure for the $\delta = 0.5$ phase and elucidate the cation displacements for the $\delta = 0.25$ phase for the first time. These new insights demonstrate the power of STEM imaging and 4D-STEM as a local probe for investigating the structure of this highly interesting mixed-phase system. Additional measurements in combination with simulations could provide further insights into the formation of the vacancy-ordered domains and the influence of the lattice on the emergent electronic and magnetic properties in those domains.

4.3 Methods

Oxygen deficient $\text{LaNiO}_{3-\delta}$ single crystals were synthesized using a recently reported high oxygen pressure floating zone method [167, 170]. The as-grown crystal boules exhibit a radial gradient in the oxygen vacancy concentration,

and samples were extracted from the center where the concentration of oxygen vacancies was relatively high. STEM lamellas were then prepared from these samples using a TFS Helios G4 X focused ion beam (FIB) following established methods. High-angle annular dark-field (HAADF) scanning transmission electron microscopy (STEM) imaging and 4D-STEM measurements were performed on a Thermo Fisher Scientific (TFS) Titan Themis operating at 120 kV. HAADF-STEM images were acquired with a 21.4 mrad convergence semi-angle and 68 mrad inner collection angle. 4D-STEM data sets were acquired in microprobe mode using the EMPAD pixelated detector. Convergence semi-angles of 0.43 and 0.55 mrad were used to ensure separation of Bragg reflections in the NBED patterns, resulting in maximum spatial resolutions of 4.8 and 3.7 nm, respectively. The pixel size of the 4D-STEM scans were chosen to approximately match the spatial resolution of the probe.

4.3.1 EWPC filtering

Maps of the $\delta = 0.5$ and 0.25 $\text{LaNiO}_{3-\delta}$ phases were calculated by first filtering each NBED pattern with exit wave power cepstrum (EWPC) analysis to decrease the effect of thickness and crystal tilt variations and then summing the intensities of the Bragg reflections associated with each phase. The NBED filtering method was previously developed by Padgett et al. and is discussed in detail elsewhere [116]. Briefly, the EWPC of each NBED pattern is first calculated from the equation:

$$EWPC = |\mathcal{F}(\log_{10}(NBED))|$$

A Hann window was applied to each log scale NBED pattern to prevent the introduction of artifacts due to non-periodic boundary conditions in diffraction space when the Fourier transform was calculated.

An inverse elliptical Gaussian mask was then applied to each pattern to exclude the low frequency portion of the EWPC corresponding to the probe envelope function. The inverse Fourier transform was calculated to recover the diffraction space pattern with primarily the lattice information remaining.

CHAPTER 5
STRUCTURE DETERMINATION OF A NEW, HIGHLY DISTORTED
INFINITE-LAYER PHASE

5.1 Background

The infinite-layer structure, comprising square planar-coordinated transition metal oxide layers (as depicted in Figure 5.1a), has attracted significant attention over the last few decades as a result of the discovery of unconventional superconductivity in $(\text{La,Ba})_2\text{CuO}_4$ [7]. The search for analogous infinite-layer structures has revealed several such compounds including iron oxide compounds exhibiting antiferromagnetic ground states [144, 70, 140]. Recently, superconductivity was demonstrated in a hole-doped infinite-layer nickel oxide as well [84, 85, 165]. Further research is being undertaken to understand the similarities and distinctions between the mechanisms of superconductivity in the nickelate and cuprate infinite-layer systems, leading to the investigation of other transition metal $3d$ oxides such as those plotted in Figure 5.1d.

The infinite-layer structure also provides a unique opportunity to investigate the two-dimensional (2D) Jahn-Teller effect (JTE). In the cooperative JTE, electronic configurations with orbital degeneracy lift that degeneracy through collective distortion of the lattice. This effect has been known to induce strong coupling effects between charge, orbital, and magnetic ordering and has been linked to many correlated phenomena such as superconductivity [56] and colossal magnetoresistance [150, 124]. In oxides, it has mostly been studied in octahedral or tetrahedral coordination geometries, with no cases of the JTE in a square planar-coordinated compound yet reported. The infinite-layer structure

presents an opportunity for such an effect to be realized, and the relatively low interlayer distance due to the absence of apical oxygen atoms in the structure creates the possibility for further complexity in the electronic structure induced by interlayer coupling. The high spin d^7 electronic configuration of cobalt in the infinite-layer cobalt oxides exhibits the necessary partial filling of the degenerate d_{xz} and d_{yz} orbitals, making them an ideal system in which to investigate the effects on crystal and electronic structure of the 2D JTE. Here, the infinite-layer compound CaCoO_2 was stabilized for the first time, revealing a complex structure comprising JT active CoO_2 layers coupled with the Ca layers due to the short interlayer distance and resulting in ångström-scale displacements in both the cobalt and calcium sites. The crystal structure was refined through a combination of STEM imaging and x-ray scattering techniques, and EELS energy-loss near-edge structure (ELNES) analysis was used to gain insight into the electronic structure.

5.2 Results and discussion

Thin films of brownmillerite $\text{CaCoO}_{2.5}$ were grown by pulsed laser deposition (PLD) and subsequently reduced via a topotactic reduction strategy to the nominal infinite-layer phase, CaCoO_2 , as shown schematically in Figure 5.1a. The structure was initially probed with benchtop x-ray diffraction (XRD). Figure 5.1b and c show 2θ scans for the as-grown and reduced films, respectively. A 12% contraction of the out-of-plane lattice parameter is observed upon reduction, from ~ 3.72 Å in the brownmillerite phase to ~ 3.27 Å in the reduced phase. Initial evidence suggesting the successful stabilization of the infinite-layer structure is provided by the agreement between this contraction and a trend exhib-

ited by several previously identified infinite-layer compounds as shown in Figure 5.1d. The successful reduction of the films was further supported by EELS analysis of the Co-L_{2,3} edge as shown in Figure 5.2. Panel a of Figure 5.2 shows EEL spectra of the Co-L_{2,3} edge for the as-grown and reduced films in blue and red, respectively. The ratio of the integrated intensities for the L₃ and L₂ edges, I_{L_3}/I_{L_2} , known as the white line ratio, was calculated for each spectrum using the Pearson method [120, 127]. These were then used to estimate the valence of each film by plotting the intensity ratios on a trend line formed by cobalt-containing compounds with known valence states (Figure 5.2b) [155]. This analysis showed a valence reduction from $\sim +2.7$ to $\sim +2.1$ for the as-grown and reduced films.

While these XRD and EELS measurements support the successful stabilization of the infinite-layer phase, they do not fully characterize the reduced phase, and leave open the possibility of significant deviations from the ideal infinite-layer structure. Traditionally, structure refinement by synchrotron x-ray scattering would be the clear way to move forward. However, since high crystalline quality was only achievable in these films for film thicknesses ~ 30 nm or less, the low crystal volume and large available phase space limited the efficacy of a traditional x-ray refinement. As a local probe, STEM is not limited by crystal volume, but imaging of multiple zone axes and with multiple imaging modalities is needed to get a complete picture of the atomic structure. The CaCoO₂ phase was therefore refined iteratively using a combination of STEM imaging and synchrotron x-ray scattering techniques.

Figure 5.3 presents cross-sectional HAADF-STEM images for two zone axes of a 31 nm thick CaCoO₂ film on a (001)-oriented SrTiO₃ substrate with a SrTiO₃ capping layer. Images of the [100]_t (tetragonal) zone axis are shown in Figure

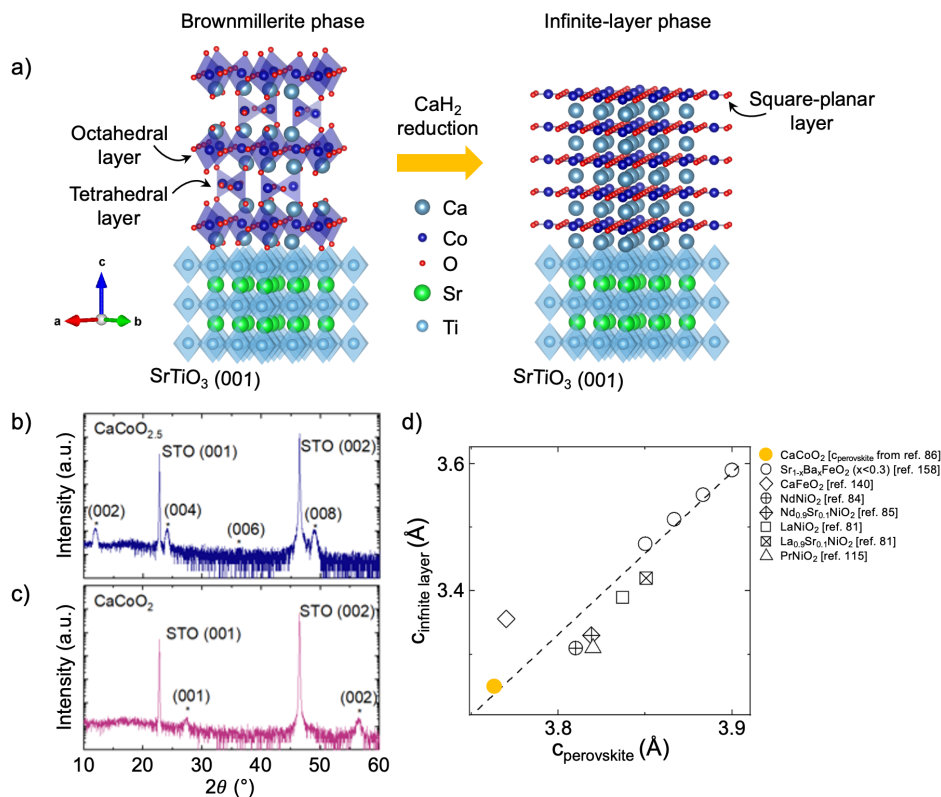


Figure 5.1: Synthesis and XRD of CaCoO_2 and $\text{CaCoO}_{2.5}$ thin films. (a) schematic of the topotactic reduction of brownmillerite $\text{CaCoO}_{2.5}$ (left) to infinite-layer CaCoO_2 (right). (b,c) XRD $\theta-2\theta$ symmetric scans of 18-nm-thick $\text{CaCoO}_{2.5}$ (b) and CaCoO_2 (c) films capped with 2-nm-thick SrTiO_3 (STO) layers grown on SrTiO_3 (001) substrates. (d) Out-of-plane lattice parameters for various transition metal oxide compounds plotted for the perovskite phase and the infinite-layer phase after topotactic reduction [86, 158, 140, 84, 85, 81, 115]. The dashed line is a linear fit for all the data points in the plot, showing a consistent relationship between the perovskite and infinite-layer phase lattice parameters. Note that CaFeO_2 has a relatively large $c_{\text{infinite layer}}/c_{\text{perovskite}}$ associate with out-of-plane displacements in both the FeO_4 and Ca layers [140]. Adapted from [72].

5.3a and b. The full film thickness is visible in panel a, showing a consistent contrast pattern over the field of view. That pattern is made clearer in the higher-resolution image in panel b. Half of the cobalt columns and all of the calcium columns are stretched in-plane into ellipses, and the other half of the cobalt columns are round and brighter than the other columns. The origins of these differences in shape and contrast are made clearer by STEM imaging down the

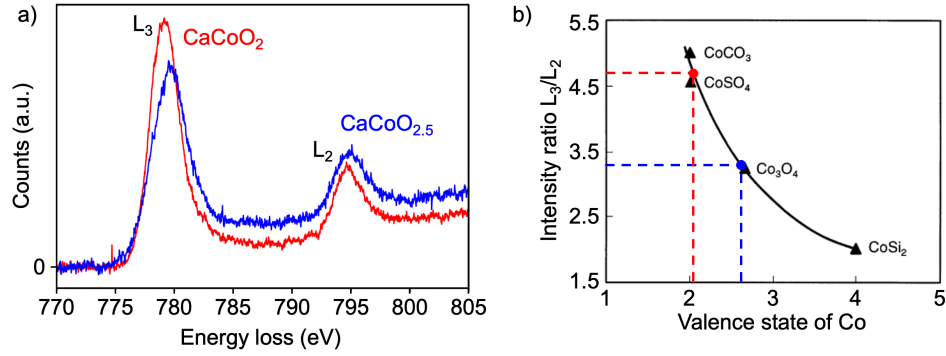


Figure 5.2: Estimation of the Co valence states in CaCoO_2 and $\text{CaCoO}_{2.5}$ thin films from the Co- $L_{2,3}$ EELS edge using the white line ratio. (a) area-averaged EEL spectra of the Co- $L_{2,3}$ edge for the as-grown, $_{2.5}$, and reduced, CaCoO_2 , films. (b) Plot of the intensity ratio I_{L_3}/I_{L_2} of the Co- $L_{3,2}$ edge for different cobalt-containing compounds with varying oxidation states. The black line indicates a polynomial fit curve for four compounds from [155] (CoCO_3 , CoSO_4 , Co_3O_4 , and CoSi_2). I_{L_3}/I_{L_2} measurements for the $\text{CaCoO}_{2.5}$ and CaCoO_2 films are denoted with blue and red circles, respectively, and indicate a reduction in oxidation state of Co of approximately +2.7 to +2.1.

$[110]_t$ zone axis in Figure 5.3c. Here, half of the cobalt and half of the calcium columns are stretched in-plane to the extent that they are each split into two columns. The distances separating the split cobalt and calcium columns were measured using an atom tracking algorithm, showing enormous separations of $1.1 \pm 0.1 \text{ \AA}$ and $0.86 \pm 0.08 \text{ \AA}$, respectively. Those measurements were used in combination with the contrast from the $[100]_t$ zone axis images to deduce the cation positions and symmetry of the unit cell. The cation positions are presented in Table 5.1. An atomic model based on those cation positions is shown in Figure 5.3d in the $[001]_t$, $[100]_t$ and $[110]_t$ projections. The observed cation structure can be described by a tetragonal unit cell $2\sqrt{2}a_t \times 2\sqrt{2}a_t \times c_t$, in the $P4_212$ symmetry group, where a_t is the lattice parameter of the ideal infinite-layer tetragonal unit cell. The oxygen positions shown in the model are those of the ideal simple-tetragonal infinite layer structure. The cation model is also overlaid on the images in Figure 5.3b and c.

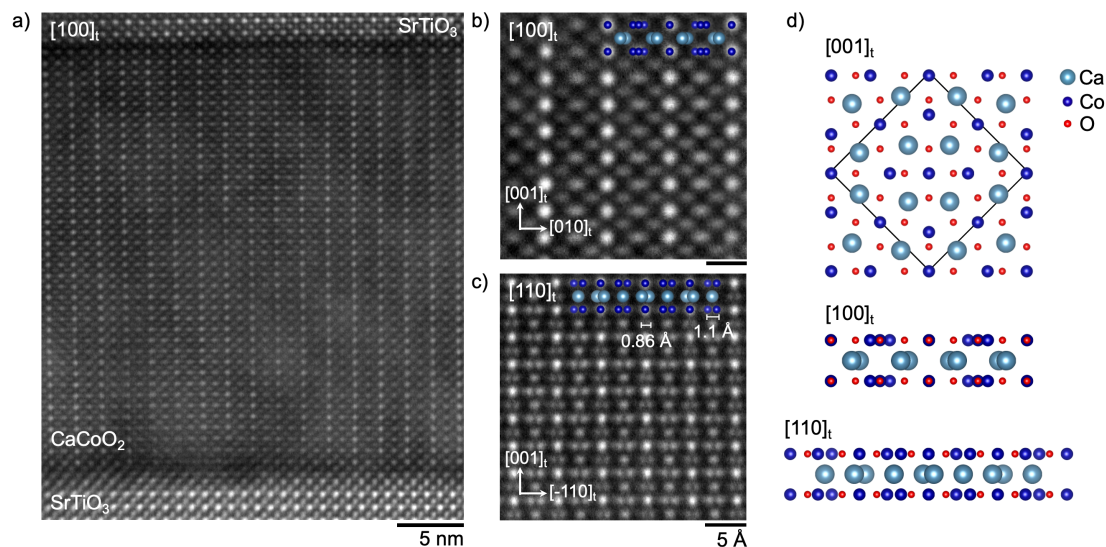


Figure 5.3: Cross-sectional HAADF-STEM imaging and measured cation model of CaCoO₂ thin films. (a) Image of the [100]_t projection of a ~ 31 nm thick CaCoO₂ film on a SrTiO₃ (001) substrate. (b,c) Higher resolution images of the [100]_t and [110]_t crystallographic projections, respectively. The measured separation between distorted cobalt and calcium columns as measured from the [110]_t projection are overlaid in panel c. (d) Cation model deduced from the measured cation displacements shown in the [001]_t, [100]_t and [110]_t projections. The same model is overlaid in b and c, showing a good match in the contrast in both cases.

It is clear the oxygen atoms would not be energetically stable in their ideal infinite-layer positions surrounded by the highly distorted cations. They must distort as well. To access these oxygen positions, an x-ray refinement was carried out using synchrotron grazing incidence x-ray diffraction (GIXRD), utilizing the cation positions measured by STEM to reduce the phase space searched over. X-ray diffraction was first simulated using the cation positions measured from HAADF-STEM and the ideal infinite-layer oxygen positions, revealing seven distinct in-plane superlattice peaks. These peaks were then measured experimentally, and their positions and integrated intensities were used to perform a Rietveld refinement, again using the measured cation positions as an initial guess. The refinement produced two possible structures, which are presented in Figure 5.4a and b and labeled x-ray refinements #1 and #2. The cation

atom	<i>P42₁2</i> symmetry group			
	x	y	z	occupation
Co ₍₁₎	0	0	0	1
Co ₍₂₎	0.2 ± 0.01	0.2 ± 0.01	0	1
Co ₍₃₎	0.5	0	0	1
Ca	0.46 ± 0.01	0.25 ± 0.01	0.5	1

Table 5.1: Atomic coordinates for cations in CaCoO₂ measured from cross-sectional HAADF-STEM imaging.

positions changed very little from the initial positions determined by STEM imaging. The main differences between the models are in the oxygen positions, particularly those delineated with black dashed boxes in Figure 5.4a and b. While the goodness of fit, *R*, for refinement #1 is somewhat better than that of refinement #2, the latter is perhaps more intuitive as it contains more cobalt sites with traditional JT-distorted oxygen coordination environments. As the experimental limit of synchrotron GIXRD measurements for these films had been reached, further STEM measurements were needed to determine the correct structure.

I therefore attempted to assess the positions of the oxygen atoms in the CaCoO₂ structure using cross-sectional ABF-STEM imaging as shown in Figure 5.5a. The ABF contrast shows no sign of oxygen atoms in the calcium planes and no sign of CoO₂-plane oxygen atoms distorting out-of-plane, confirming that CaCoO₂ is indeed an infinite-layer structure. The ABF-STEM contrast does not, however, clearly show the positions of the oxygen atoms in the CoO₂ planes. This is due in part to overlap with the highly distorted cobalt atoms and in part to the SNR of the image, which is limited by beam and air sensitivity of the sample. Figure 5.5b and c show multislice simulations of x-ray refined models #1 and #2. It is clear even from the projected atomic models in Figure 5.4a and

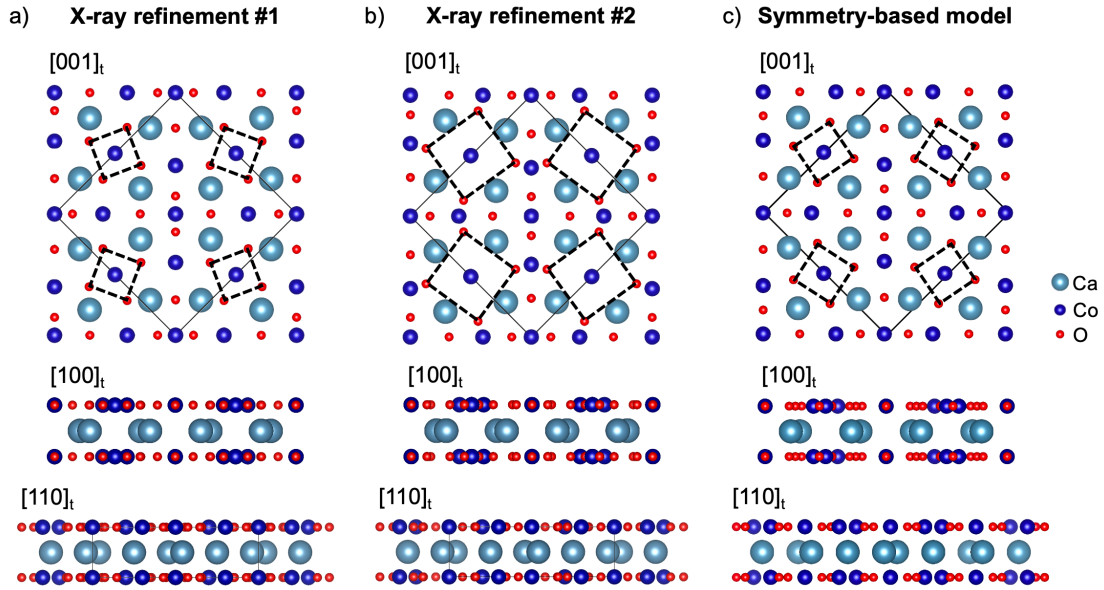


Figure 5.4: Prospective structure models for CaCoO_2 . (a,b) X-ray refined models #1 and #2 shown for the $[001]_t$, $[100]_t$ and $[110]_t$ projections. (c) Symmetry-based model with cation positions measured from STEM and oxygen positions hypothesized based on observed symmetry and ABF contrast shown in the same three projections.

b that there are minimal differences in the oxygen positions for the $[100]_t$ and $[110]_t$ projections. This is made clearer in the simulated images in Figure 5.5b and c, which show only small differences in the contrast in the CoO_2 planes. Given that these simulations represent a nearly ideal case with only $1 \mu\text{m}$ spherical aberration, and no defocus, detector noise, finite source size, crystal mistilt etc., it would be very difficult to distinguish between the two structures with experimental cross-sectional ABF-STEM contrast even if the sample was more robust. Moving to plan-view imaging therefore presented the obvious next step to identify the structure.

In plan-view, all the atomic positions are well separated, and there are clear differences in the positions of some of the oxygen atoms, as shown in Figure 5.4a and b. However, the same limitations of beam and air sensitivity of the sample exist. Additionally, the preparation of plan-view focused ion beam (FIB) sam-

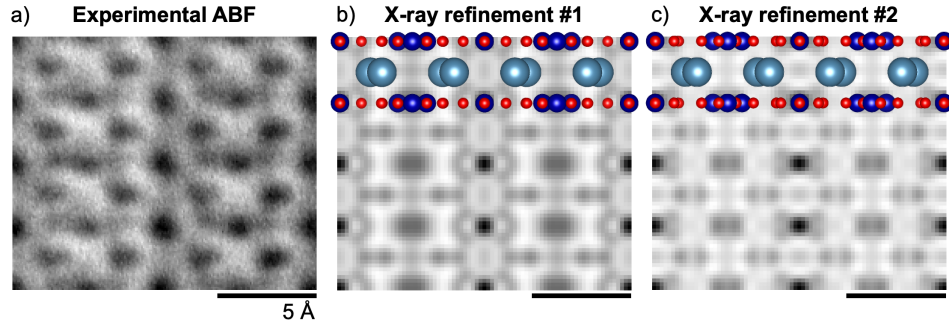


Figure 5.5: Experimental and simulated cross-sectional ABF-STEM imaging of $[110]_t$ -oriented CaCoO_2 . (a) Experimental ABF-STEM image. (b,c) Simulated ABF-STEM images for x-ray refinements #1 and #2. The simulations were calculated for 25 nm thick specimens, with a 120 kV electron probe, a 21.4 mrad convergence angle, 0 nm of defocus, 1 μm of spherical aberration, and no other aberrations. The associated atomic model is overlaid on each simulated image.

ples is quite challenging due to the thinness of the film. In order to unambiguously identify oxygen positions, the sample needed to be quite thin (~ 20 nm or less), and the substrate needed to be completely removed in order to avoid contributions of the oxygen atoms in the perovskite SrTiO_3 substrate to the image contrast. Details of the methods used to achieve this sample preparation are included in Section 5.3.2.

Figure 5.6a presents a plan-view HAADF-STEM image where the contrast is coming solely from the CaCoO_2 film. This image once again confirms the cation positions previously measured from cross-sectional STEM imaging as demonstrated by the overlaid cation model. The vertical groups of three cobalt columns are likely due to those columns sitting so close together, in combination with a slight mistilt of the crystal in this field of view. This effect is likely due to mild out-of-plane buckling of the lattice that has been observed by strain mapping in cross-sectional imaging and can be seen in larger field-of-view plan-view imaging as shown in Figure 5.7. In this image, there is a transition from the cobalt column triplets appearing most obvious in the vertical direction on

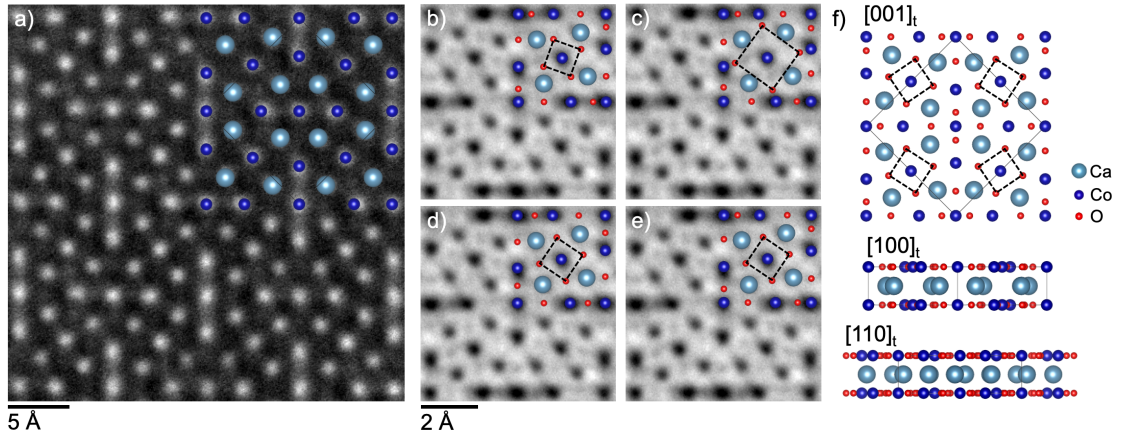


Figure 5.6: Plan-view HAADF- and ABF-STEM imaging of CaCoO_2 films and final refined structure model. (a) HAADF-STEM image showing good agreement with the cation model based on cross-sectional imaging. (b-e) Unit cell averaged ABF-STEM image with x-ray refined model 1, x-ray refined model 2, the symmetry-based model, and the final refinement overlaid, respectively. (f) $[001]_t$, $[100]_t$ and $[110]_t$ projections of the final refined structure.

the left side of the image to appearing most obvious in the horizontal direction on the right side of the image.

Figure 5.6b and c show a unit cell averaged ABF-STEM image from the same region of crystal as Figure 5.6a. The image is repeated in each panel, and subsets of the atomic models for x-ray refinement #1 and x-ray refinement #2 are overlaid in panels b and c, respectively. Comparing the image contrast with the oxygen atoms highlighted by the black dashed box in each model, it is clear that x-ray refinement #1 (panel b) is the better match. The match is not perfect, however, as the corners of the dashed box appear slightly rotated with respect to the actual oxygen contrast in the image.

Due to the large phase space of the x-ray refinement and the limited number of measurable diffraction peaks, it is possible the calculation terminated in a local minimum. Therefore, to further limit the available phase space, a model of the oxygen positions was developed based on the ABF-STEM contrast and the

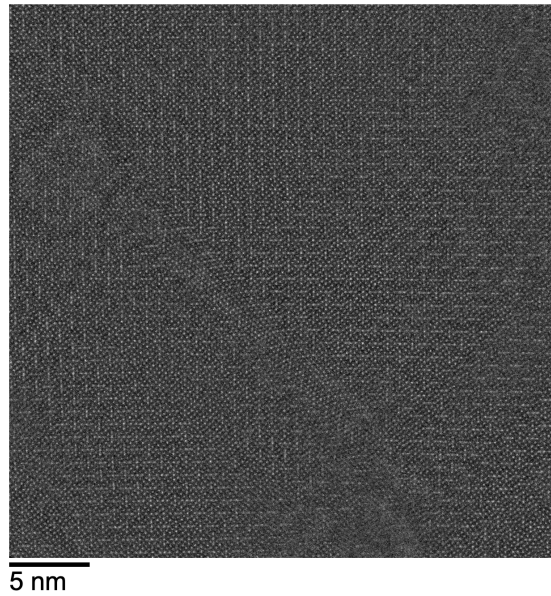


Figure 5.7: Larger field-of-view plan-view HAADF-STEM image of CaCoO_2 . The image shows a transition between the cobalt column triplet pattern appearing more obvious in the vertical direction on the left side of the image to appearing more obvious in the horizontal direction on the right side of the image. There is also an extended defect in the lattice visible through the center of the image.

available phonon displacement modes for the observed symmetry group, $P42_12$, using the ISODISTORT software package (see Section 5.3.4 for details) [139, 22]. A subset of this model, shown in full in Figure 5.4c, is overlaid on the plan-view ABF-STEM image in Figure 5.6d. The symmetry-based model was then used as the starting structure in a refinement of the same x-ray data. The oxygen positions delineated by the blacked dashed boxes in Figure 5.4c were fixed to those positions to further decrease the likelihood of the refinement terminating in a local minimum. The final refined structure for CaCoO_2 is presented in Figure 5.6f and is overlaid on the unit cell averaged ABF-STEM image in Figure 5.6e. The agreement with the ABF-STEM contrast is observably better than x-ray refinement #1 for both the fixed and unfixed oxygen positions. Atomic coordinates for the symmetry-based model and the final refined structure are presented in Table 5.2.

atom	x		y		z		occupation
	Initial	Refined	Initial	Refined	Initial	Refined	
Co ₍₁₎	0	0	0		0	0	1
Co ₍₂₎	0.20 ± 0.01	0.21 ± 0.01	0.2 ± 0.01	0.21 ± 0.01	0	0	1
Co ₍₃₎	0.5	0.50	0		0	0	1
Ca	0.46 ± 0.01	0.45 ± 0.01	0.25 ± 0.01	0.25 ± 0.01	0.5	0.5	1
O ₍₁₎	0.35	0.35 ± 0.01	0.10	0.10 ± 0.01	0	0	1
O ₍₂₎	0.35	0.36 ± 0.01	0.35	0.36 ± 0.01	0	0	1
O ₍₃₎	0.10	0.08 ± 0.01	0.10	0.08 ± 0.01	0	0	1

Table 5.2: Atomic coordinates for the initial (symmetry-based) structure model and final refined structure of CaCoO₂

The final refined structure contains three distinct cobalt coordination environments: Co₍₁₎, Co₍₂₎, and Co₍₃₎ as depicted in blue, green, and orange respectively in Figure 5.8a. The blue plaquette (Co₍₁₎) is strongly JT-distorted, while the orange plaquette (Co₍₂₎) is trapezoidal and the green plaquette (Co₍₃₎) is square. It is surprising that only one quarter of the cobalt ions in the structure exhibit a traditional JT-distortion. The mix of coordination environments can be understood to originate from a competition between the JTE and geometric frustration induced by coupling between the CoO₂ planes and the Ca planes, which sit much closer than in the perovskite structure due to the lack of apical oxygen atoms. As indicated by the dashed rectangles in Figure 5.8a, the JTE distorts the Ca layer in addition to the Co₍₁₎O₄ plaquettes. The anisotropic distortions of neighboring Ca sites are highly geometrically frustrated, leading to the complex distortion pattern observed.

Analysis of the O-K and Ca-L_{2,3} EELS edges was undertaken to investigate the electronic structure effects associated with the observed distortion pattern. Figure 5.9a and b present area-averaged O-K edge and Ca-L_{2,3} edge spectra for the brownmillerite CaCoO_{2.5} and distorted infinite-layer CaCoO₂ films in blue

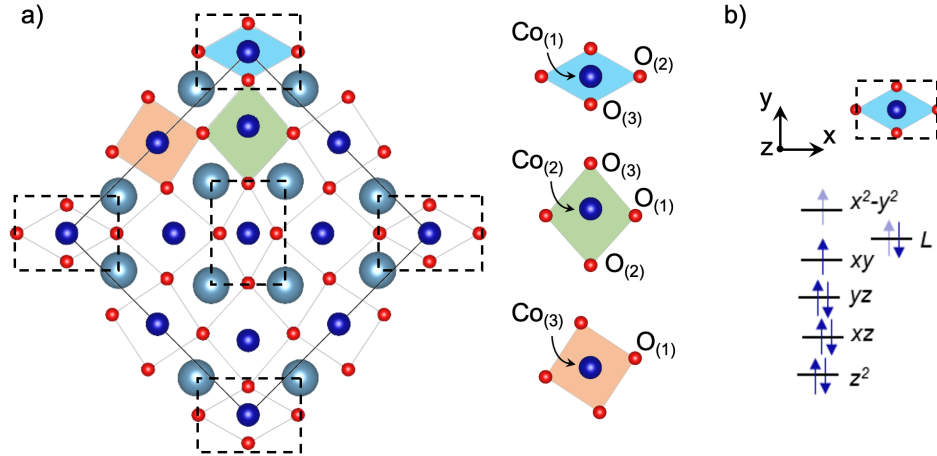


Figure 5.8: Jahn-Teller effect and geometric frustration in the CaCoO_2 lattice. (a) $[001]_t$ projection of the final refined CaCoO_2 structure. The three distinct oxygen-coordinated Co sites, $\text{Co}_{(1)}$, $\text{Co}_{(2)}$, and $\text{Co}_{(3)}$, are highlighted in blue, green, and orange, respectively. Each plaquette is shown on the right with the coordinating oxygen sites labeled. (b) Energy level diagram of the JT-distorted $\text{Co}_{(1)}$ sites from a ligand multiplet calculation. Light blue arrows indicate occupation by half an electron. Adapted from [72].

and red, respectively. The $\text{Ca-L}_{2,3}$ spectra show no significant change upon reduction, indicating as expected, that the valence state of Ca is not affected by the process. On the other hand, there are two notable differences in the O-K edge spectra. First, upon reduction of the $\text{CaCoO}_{2.5}$ films to CaCoO_2 , I observe a suppression of the distinct pre-peak (labeled a in Figure 5.9a) in the region of the O-K edge associated with hybridization between O $2p$ and transition metal $3d$ orbitals, consistent with a nominal electronic transition from $3d^6$ to $3d^7$. This is similar to the pre-peak suppression observed upon reduction from the perovskite to the infinite-layer phase in the related nickelates [48]. At the same time, a shoulder emerges in the CaCoO_2 spectrum (labeled b in Figure 5.9a), which is similar to a feature attributed to ligand hole states in doped infinite-layer nickelates [48]. This feature is also consistent with published spectra reported for low oxygen-coordination layers of other reduced cobalt oxide compounds, for example $\text{LaCoO}_{2.67}$ and $\text{La}_{0.5}\text{Sr}_{0.5}\text{CoO}_{2.25}$, as well as tetrahedrally coordinated Co

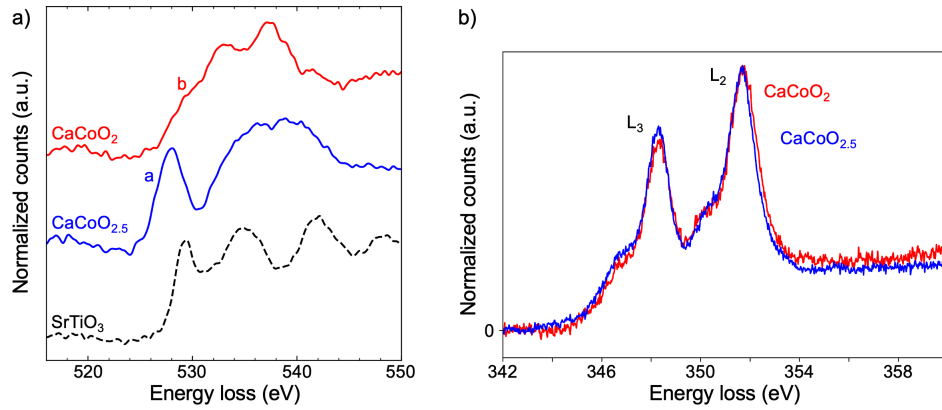


Figure 5.9: EELS analysis of the O-K and Ca-L_{2,3} edges of CaCoO_{2.5} and CaCoO₂ thin films. (a) O-K edge and (b) Ca-L_{2,3} edge spectra for brownmillerite CaCoO_{2.5} and CaCoO₂ films shown in blue and red, respectively. Upon reduction of the CaCoO_{2.5} films to CaCoO₂, a suppression of the distinct pre-peak (labeled a) was observed in the region of the O-K edge associated with hybridization between O 2*p* and transition metal 3*d* orbitals consistent with a nominal electronic transition from 3*d*⁶ to 3*d*⁷. The emergence of a shoulder in the CaCoO₂ spectrum (labeled b) was also observed and attributed to ligand hole states similar to those observed in doped infinite-layer nickelates [48]. This feature is also consistent with published spectra acquired from low oxygen-coordination layers of other reduced cobalt oxide compounds, LaCoO_{2.67} and La_{0.5}Sr_{0.5}CoO_{2.25}, as well as tetrahedrally coordinated Co in CoO [51, 42, 169]. An O-K edge spectrum of the SrTiO₃ substrate is included in black for comparison. All spectra are Gaussian filtered with an 8 energy channel standard deviation for clarity. The unfiltered spectra are shown in Figure 5.10

in CoO [51, 42, 169].

In CaCoO₂, the presence of a feature associated with ligand hole states supports the nominal electron energy level diagram presented in Figure 5.8b for the JT-distorted Co₍₁₎ sites. In this diagram, the degeneracy of the 3*d*_{*xz*} and 3*d*_{*yz*} orbitals has been lifted and a ligand hole state, *L*, has been introduced with an electron shared between that state and the 3*d*_{*x²-y²*} states to form a 3*d*⁸*L* configuration. Details of additional density functional theory (DFT) + *U* calculations and linearly polarized x-ray absorption spectroscopy (XAS) measurements that support this picture of the origin and electronic structure of the distortion pattern observed in CaCoO₂ can be found in Reference [72].

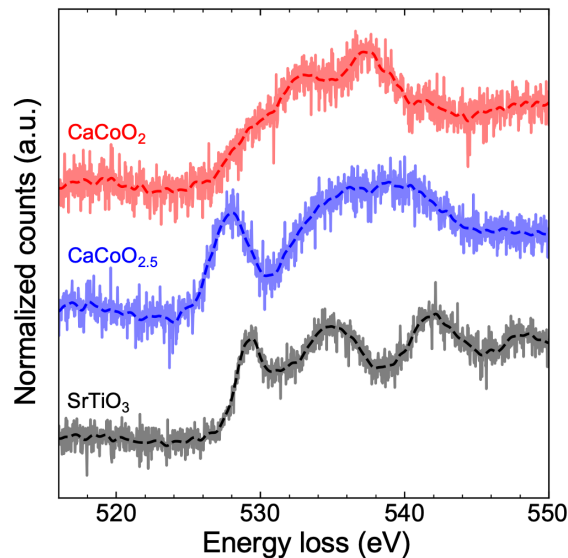


Figure 5.10: Unfiltered O-K edge EEL spectra. O-K edge spectra of CaCoO_2 and $\text{CaCoO}_{2.5}$ in red and blue, respectively. The partially transparent, solid lines indicate the raw, background subtracted data, and the dashed lines indicate the Gaussian filtered spectra as shown in Figure 5.9a. An O-K edge spectrum of the SrTiO_3 substrate is included in black for comparison.

In conclusion, CaCoO_2 represents the first demonstration of the 2D JTE in a metal oxide compound. The highly distorted structure was refined through an iterative combination of HAADF- and ABF-STEM imaging and synchrotron x-ray refinement. The complex distortion pattern was found to arise from a combination of the JTE and geometric frustration due to interlayer coupling between the CoO_2 and Ca layers. This competition results in three distinct oxygen-coordinated cobalt sites, setting apart the JT-distorted infinite-layer structure from other layered perovskite compounds which exhibit equivalent octahedral distortions [17, 59, 1]. The understanding of the JTE developed through the investigation of this system may have general implications for complex compounds comprising 2D atomic layers where the JTE and interlayer coupling are important.

5.3 Methods

5.3.1 Thin film synthesis and characterization

Brownmillerite $\text{CaCoO}_{2.5}$ thin films were deposited on perovskite SrTiO_3 001 substrates by pulsed laser deposition (PLD). A 5 unit cell SrTiO_3 capping layer was added to each film to inhibit degradation during or after the film reduction process. The as grown $\text{CaCoO}_{2.5}$ films were then reduced via topotactic reduction to CaCoO_2 . Additional film deposition and reduction details are available elsewhere [72].

Conventional XRD was performed using a monochromated $\text{Cu K}_{\alpha 1}$ source ($\lambda = 1.5406 \text{ \AA}$). Synchrotron grazing incidence x-ray diffraction (GIXRD) measurements were performed using the Huber six-circle diffractometer at the 3A beamline of the Pohang Light Source-II in South Korea. The incident beam was monochromated to 1.1078 \AA . GIXRD data were acquired over a 2θ range from 0° to 75° with a step interval of 0.01° .

GIXRD refinement was performed using the Reitveld method. Seven independent (hkl) peaks were used for the refinement. The goodness of fit was characterized by the R-factor $R = \frac{\sum_i |I_i^{obs} - I_i^{calc}|}{\sum_i I_i^{obs}}$ where I_i^{obs} and I_i^{calc} are the observed and calculated integrated Bragg peak intensity of the i^{th} (hkl) plane, respectively.

5.3.2 Cross-section and plan-view FIB lamella preparation

STEM specimens were prepared using a Thermo Fisher Scientific Helios G4 UX focused ion beam (FIB). Total air exposure of the prepared STEM specimens was

limited to less than 15 minutes to minimize possible degradation of the films. Cross-section samples were prepared and thinned to electron transparency using standard lift out and thinning methods.

Plan-view samples were prepared by first using the standard lift out method with the lamella width increased to $4\ \mu\text{m}$ and then attaching to a half grid at a 90° angle to the standard orientation (i.e., with the grid cartridge lying flat across two SEM pegs on the FIB stage). The grid cartridge was then reloaded in the standard orientation for thinning. A layer of protective platinum was deposited on the top edge of the lamella. A schematic view of the top (thinned) edge of a plan-view lamella is shown in Figure 5.11a. The lamellas were thinned at the indicated 3° angle to ensure that along the length of each lamella there was a region containing only the film, with the substrate and protective carbon layers removed from each side. As high crystallinity was only achievable for films thinner than 30 nm, this usable region was limited to $\sim 300 - 400$ nm in width. To ensure the contrast between platinum, carbon, and substrate layers was directly interpretable and not influenced by lamella thickness, the film side of the lamella was thinned first, until transitions between all four layers were visible. Note the film was too thin to produce reliable contrast in the electron beam image. The substrate side was subsequently thinned to achieve electron transparency. Figure 5.11b shows an SEM image of the film side of a final, thinned lamella where the platinum, carbon, and substrate layers are distinguishable across the length of the lamella. The region where the lamella is expected to both contain only film and be sufficiently thin for ABF-STEM imaging is indicated.

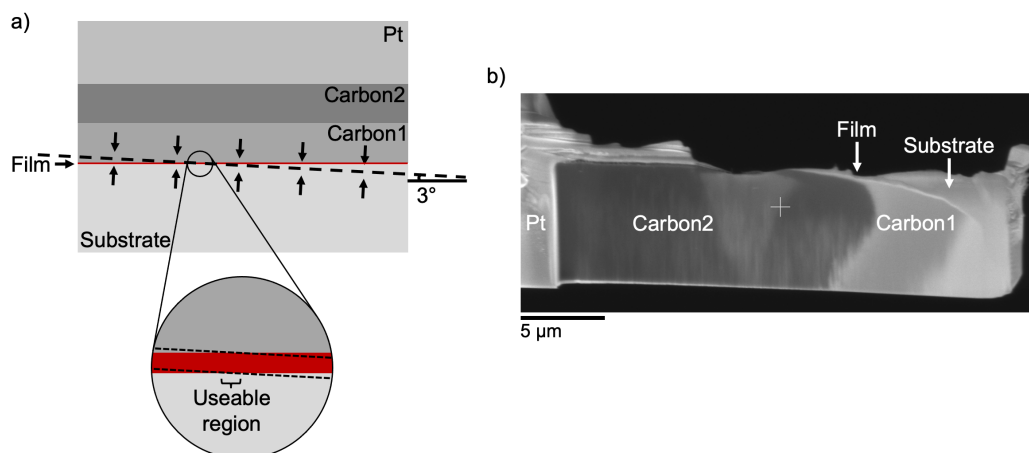


Figure 5.11: Plan-view FIB lamella preparation. (a) Schematic representation of top (thinned) edge of plan-view lamella showing the substrate on one side, the thin film in red, and the protective layers of carbon and platinum on the other side. The lamella is thinned at the 3° angle shown to ensure there exists a region in the final thinned lamella with only the film left. This usable region is shown in the blown up view. (b) SEM image of a final, thinned plan-view lamella. From left to right, the contrast across the length of the lamella indicates the layers of platinum, carbon and substrate. The usable region where only film remains is indicated.

5.3.3 STEM and EELS measurements

HAADF- and ABF-STEM data were acquired using a Thermo Fisher Scientific Spectra 300 X-CFEG operating at 120 or 300 kV with a convergence angle of 30 mrad. Inner and outer collection angles were approximately 60 and 200 mrad respectively for HAADF and 15 and 30 mrad respectively for ABF imaging. Samples were cleaned by baking for 10-12 hours at 100°C under vacuum, ensuring the sample would not be modified. Further, cryogenic cooling using a liquid nitrogen holder was used to suppress the buildup of remaining carbon contamination on plan-view samples. To obtain high signal-to-noise-ratio (SNR) images, many fast-acquisition images were acquired and subsequently aligned using a rigid registration process optimized for noisy images [133]. The displacements of cation positions were estimated from HAADF-STEM images

of the $[110]_t$ zone axis by first fitting all atomic positions using a Gaussian fitting algorithm in python and then extracting the distances separating cobalt and calcium dumbbells. This was repeated for multiple images and the average separations were tabulated, with the measurement error given as the standard deviation over all distances measured for each atomic species. These $[\bar{1}10]_t$ -direction displacements were then used in combination with the contrast from the $[100]_t$ zone axis imaging to deduce the cation positions.

Due to electron beam sensitivity of the sample, a probe current of less than 30 pA was used for all STEM data acquisitions. EELS measurements therefore required total acquisition times of $\sim 5,000$ seconds for each spectrum to achieve sufficient SNR to distinguish differences in the EELS fine structure. The spectra presented are aligned and summed series of several acquisitions. To ensure stage stability sufficient for such long acquisitions, a Nion UltraSTEM operated at 100 kV and equipped with a high stability stage, an Enfinium ER spectrometer, and Quefina2 camera was used to acquire all EELS data. The effective energy resolution, measured by the full-width-at-half-maximum of the zero-loss peak, was 0.34 eV. To ensure consistency, spectra from multiple regions of each sample were acquired. The individual spectra for each edge were first aligned with respect to each other and summed to produce high SNR measurements for the as-grown and reduced films. Absolute energy alignments were then applied to the Co-L_{3,2} and Ca-L_{3,2} edges and the O-K edges based on the Ti-L_{3,2} and O-K edges of the SrTiO₃ substrate, respectively, which serve as well studied and consistent references. White line ratios were calculated from the Co-L_{3,2} edges using the Pearson method [120, 127].

5.3.4 Estimation of oxygen positions

The positions of oxygen atoms were estimated based on ABF-STEM contrast in combination with the phonon displacement modes allowed by the measured crystal symmetry. The available displacement modes were identified using the ISODISTORT software package, part of the ISOTROPY suite, which outputs the atomic displacement modes available given a parent structure transitioning to a lower symmetry state [139, 22]. These displacement modes were then visualized and manipulated using the application ISOVIZ, allowing me to identify the combination of modes and associated oxygen positions that provided the best qualitative match with the ABF-STEM contrast.

5.3.5 Multislice simulations

Annular bright-field (ABF) STEM image simulations were carried out using the multislice method [27, 49, 75] implemented in the TEMSIM simulation package [74]. For each simulation the probe was defined with a defocus of 0 nm, a spherical aberration coefficient of 1 μm , and a convergence semi-angle of 21.4 mrad. Supercells of x-ray refined structures #1 and #2 in the $[100]_t$ orientation were defined with dimensions $26.1 \times 30.5 \times 250 \text{ \AA}$. ABF-STEM images were simulated using $1024 \times 1024 \text{ pixel}^2$ transmission and probe wave functions resulting in a maximum scattering angle of 375 mrad. A scan step size of 0.1 \AA and inner and outer collection angles of 9 and 18 mrad, respectively, were used. Phonon effects were not included in the simulations.

The work presented here is published in [72]

BIBLIOGRAPHY

- [1] F. Aguado, F. Rodríguez, R. Valiente, A. Señas, and I. Goncharenko. Three-Dimensional Magnetic Ordering in the Rb_2CuCl_4 Layer Perovskite - Structural Correlations. *Journal of Physics Condensed Matter*, 16(12):1927–1938, 2004.
- [2] M. Alimoradi Jazi, V. A.E.C. Janssen, W. H. Evers, A. Tadjine, C. Delerue, L. D.A. Siebbeles, H. S.J. Van Der Zant, A. J. Houtepen, and D. Vanmaekelbergh. Transport Properties of a Two-Dimensional PbSe Square Superstructure in an Electrolyte-Gated Transistor. *Nano Letters*, 17(9):5238–5243, 2017.
- [3] S. James Allen, Adam J. Hauser, Evgeny Mikheev, Jack Y. Zhang, Nelson E. Moreno, Junwoo Son, Daniel G. Ouellette, James Kally, Alex Kozhanov, Leon Balents, and Susanne Stemmer. Gaps and Pseudogaps in Perovskite Rare Earth Nickelates. *APL Materials*, 3(6), 2015.
- [4] J. A. Alonso, M. J. Martínez-Lope, J. L. García-Muñoz, and M. T. Fernández-Díaz. A Structural and Magnetic Study of the Defect Perovskite $\text{LaNiO}_{2.5}$ from High-Resolution Neutron Diffraction Data. *Journal of Physics Condensed Matter*, 9(30):6417–6426, 1997.
- [5] M. Arredondo, M. Weyland, M. Hambe, Q. M. Ramasse, P. Munroe, and V. Nagarajan. Chemistry of Ruddlesden-Popper Planar Faults at a Ferroelectric-Ferromagnet Perovskite Interface. *Journal of Applied Physics*, 109(8), 2011.
- [6] Ryotaro Aso, Daisuke Kan, Yuichi Shimakawa, and Hiroki Kurata. Atomic Level Observation of Octahedral Distortions at the Perovskite Oxide Heterointerface. *Scientific Reports*, 3:1–6, 2013.
- [7] M. Azuma, Z. Hiroi, M. Takano, Y. Bando, and Y. Takeda. Superconductivity at 110 K in the Infinite-Layer Compound $(\text{Sr}_{1-x}\text{Ca}_x)_{1-y}\text{CuO}_2$. *Nature*, 356(6372):775–776, 1992.
- [8] David J. Baek, Di Lu, Yasuyuki Hikita, Harold Y. Hwang, and Lena F. Kourkoutis. Mapping Cation Diffusion Through Lattice Defects in Epitaxial Oxide Thin Films on the Water-Soluble Buffer Layer $\text{Sr}_3\text{Al}_2\text{O}_6$ using Atomic Resolution Electron Microscopy. *APL Materials*, 5(9), 2017.

- [9] Ismail El Baggari, Benjamin H. Savitzky, Alemayehu S. Admasu, Jaewook Kim, Sang Wook Cheong, Robert Hovden, and Lena F. Kourkoutis. Nature and Evolution of Incommensurate Charge Order in Manganites Visualized with Cryogenic Scanning Transmission Electron Microscopy. *Proceedings of the National Academy of Sciences of the United States of America*, 115(7):1445–1450, 2018.
- [10] Daniel M. Balazs, Tyler A. Dunbar, Detlef M. Smilgies, and Tobias Hanrath. Coupled Dynamics of Colloidal Nanoparticle Spreading and Self-Assembly at a Fluid-Fluid Interface. *Langmuir*, 36(22):6106–6115, 2020.
- [11] P. E. Batson, N. Dellby, and O. L. Krivanek. Sub-Ångstrom Resolution Using Aberration Corrected Electron Optics. *Nature*, 418(6898):617–620, 2002.
- [12] William J. Baumgardner, Kevin Whitham, and Tobias Hanrath. Confined-but-Connected Quantum Solids via Controlled Ligand Displacement. *Nano Letters*, 13(7):3225–3231, 2013.
- [13] H. Bethe. Zur Theorie des Durchgangs Schneller Korpuskularstrahlen durch Materie. *Annalen der Physik*, 397:325–400, 1930.
- [14] H. Bethe. Bremsformel für Elektronen Relativistischer Geschwindigkeit. *Zeitschrift für Physik*, 76:293–299, 1932.
- [15] Anuj Bhargava, Yuval Elbaz, Quynh Sam, Michelle A. Smeaton, Lena F. Kourkoutis, Maytal Caspary Toroker, and Richard D. Robinson. Enhanced Li-ion Diffusion and Electrochemical Performance in Strained-Manganese-Iron Oxide Core-Shell Nanoparticles. *Journal of Chemical Physics*, 155(14), 2021.
- [16] Nabraj Bhattarai, Gilberto Casillas, Arturo Ponce, and Miguel Jose-Yacaman. Strain-Release Mechanisms in Bimetallic Core-Shell Nanoparticles as Revealed by C_s -Corrected STEM. *Surface Science*, 609:161–166, 2013.
- [17] D. I. Bilc and D. J. Singh. Frustration of Tilts and A-Site Driven Ferroelectricity in KNbO_3 - LiNbO_3 Alloys. *Physical Review Letters*, 96(14):1–4, 2006.
- [18] Valentina Bisogni, Sara Catalano, Robert J. Green, Marta Gibert, Raoul Scherwitzl, Yaobo Huang, Vladimir N. Strocov, Pavlo Zubko, Shadi Balandeh, Jean Marc Triscone, George Sawatzky, and Thorsten Schmitt.

Ground-State Oxygen Holes and the Metal-Insulator Transition in the Negative Charge-Transfer Rare-Earth Nickelates. *Nature Communications*, 7:17–19, 2016.

- [19] Albina Y Borisevich, Oleg S Ovchinnikov, Hye Jung Chang, Mark P Oxley, Pu Yu, Jan Seidel, Eugene A Eliseev, Anna N Morozovska, Ramamoorthy Ramesh, Stephen J Pennycook, and Sergei V Kalinin. Mapping Octahedral Tilts and Polarization Across a Domain Wall in BiFeO₃ from Z-Contrast Scanning Transmission Electron Microscopy Image Atomic Column Shape Analysis. *ACS nano*, 4(10):6071–6079, 2010.
- [20] G. Brunetti, D. Robert, P. Bayle-Guillemaud, J. L. Rouvière, E. F. Rauch, J. F. Martin, J. F. Colin, F. Bertin, and C. Cayron. Confirmation of the Domino-Cascade Model by LiFePO₄/FePO₄ Precession Electron Diffraction. *Chemistry of Materials*, 23(20):4515–4524, 2011.
- [21] Karen C Bustillo, Steven E Zeltmann, Min Chen, Jennifer Donohue, Jim Ciston, Colin Ophus, and Andrew M Minor. 4D-STEM of Beam-Sensitive Materials. *Accounts of Chemical Research*, 54:2543–2551, 2021.
- [22] Branton J. Campbell, Harold T. Stokes, David E. Tanner, and Dorian M. Hatch. ISODISPLACE: A Web-Based Tool for Exploring Structural Distortions. *Journal of Applied Crystallography*, 39(4):607–614, 2006.
- [23] Graham H. Carey, Larissa Levina, Riccardo Comin, Oleksandr Voznyy, and Edward H. Sargent. Record Charge Carrier Diffusion Length in Colloidal Quantum Dot Solids via Mutual Dot-to-Dot Surface Passivation. *Advanced Materials*, 27(21):3325–3330, 2015.
- [24] T. A. Caswell, P. Ercius, M. W. Tate, A. Ercan, S. M. Gruner, and D. A. Muller. A High-Speed Area Detector for Novel Imaging Techniques in a Scanning Transmission Electron Microscope. *Ultramicroscopy*, 109(4):304–311, 2009.
- [25] S Catalano, M Gilbert, J Fowlie, J Iniguez, J-M Triscone, and J Kreisel. Rare-Earth Nickelates RNiO₃: Thin Films and Heterostructures. *Reports on Progress in Physics*, 81:046501, 2018.
- [26] Zhen Chen, Yi Jiang, Yu-Tsun Shao, Megan E. Holtz, Michal Odstrčil, Manuel Guizar-Sicairos, Isabelle Hanke, Steffen Ganschow, Darrell G. Schlom, and David A. Muller. Electron Ptychography Achieves Atomic-Resolution Limits Set by Lattice Vibrations. *Science*, 372(6544):826–831, 2021.

- [27] J. M. Cowley and A. F. Moodie. The Scattering of Electrons by Atoms and Crystals. I. A New Theoretical Approach. *Acta Crystallographica*, 10(10):609–619, 1957.
- [28] Paul Cueva, Robert Hovden, Julia A. Mundy, Huolin L. Xin, and David A. Muller. Data Processing for Atomic Resolution Electron Energy Loss Spectroscopy. *Microscopy and Microanalysis*, 18(4):667–675, 2012.
- [29] J. Cui, Y. Yao, Y. G. Wang, X. Shen, and R. C. Yu. The Origin of Atomic Displacements in HAADF Images of the Tilted Specimen. *Ultramicroscopy*, 182:156–162, 2017.
- [30] Jessica Cimada daSilva, Michelle A. Smeaton, Tyler A. Dunbar, Yuanze Xu, Daniel M. Balazs, Lena F. Kourkoutis, and Tobias Hanrath. Mechanistic Insights into Superlattice Transformation at a Single Nanocrystal Level Using Nanobeam Electron Diffraction. *Nano Letters*, 20(7):5267–5274, 2020.
- [31] F.M.F; de Groot, M; Grioni, J.C; Fuggle, J. Ghijsen, G.A. Sawatzky, and H. Petersen. Oxygen 1s X-Ray-Absorption Edges of Transition-Metal Oxides. *Physical Review B*, 40(8):5715–5723, 1989.
- [32] Christophe Delerue. From Semiconductor Nanocrystals to Artificial Solids with Dimensionality Below Two. *Physical Chemistry Chemical Physics*, 16(47):25734–25740, 2014.
- [33] Shiqing Deng, Lijun Wu, Hao Cheng, Jin Cheng Zheng, Shaobo Cheng, Jun Li, Wenbin Wang, Jian Shen, Jing Tao, Jing Zhu, and Yimei Zhu. Charge-Lattice Coupling in Hole-Doped $\text{LuFe}_2\text{O}_{4+\delta}$: the Origin of Second-Order Modulation. *Physical Review Letters*, 122(12):126401, 2019.
- [34] G. Deptuch, A. Besson, P. Rehak, M. Szelezniak, J. Wall, M. Winter, and Y. Zhu. Direct Electron Imaging in Electron Microscopy with Monolithic Active Pixel Sensors. *Ultramicroscopy*, 107(8):674–684, 2007.
- [35] Ankit S. Disa, F. J. Walker, Sohrab Ismail-beigi, and Charles H. Ahn. Research Update: Orbital Polarization in LaNiO_3 -Based Heterostructures. *APL Materials*, 3(062303), 2015.
- [36] Roberto Dos Reis, Hao Yang, Colin Ophus, Peter Ercius, Gregory Bizarri, Didier Perrodin, Tetiana Shalapska, Edith Bourret, Jim Ciston, and Ulrich Dahmen. Determination of the Structural Phase and Octahedral Rotation Angle in Halide Perovskites. *Applied Physics Letters*, 112(7), 2018.

- [37] R.F. Egerton. *Electron Energy Loss Spectroscopy in the Electron Microscope*. Springer, Boston, MA, third edition, 2011.
- [38] Wiel H. Evers, Juleon M. Schins, Michiel Aerts, Aditya Kulkarni, Pierre Capiod, Maxime Berthe, Bruno Grandidier, Christophe Delerue, Herre S. J. van der Zant, Carlo van Overbeek, Joep L. Peters, D. Vanmaekelbergh, and Laurens D. A. Siebbeles. High Charge Mobility in Two-Dimensional Percolative Networks of PbSe Quantum Dots Connected by Atomic Bonds. *Nature Communications*, 6:8195, 2015.
- [39] A. R. Faruqi, R. Henderson, M. Pryddetch, P. Allport, and A. Evans. Direct Single Electron Detection with a CMOS Detector for Electron Microscopy. *Nuclear Instruments and Methods in Physics Research, Section A: Accelerators, Spectrometers, Detectors and Associated Equipment*, 546(1-2):170–175, 2005.
- [40] S. D. Findlay, N. Shibata, H. Sawada, E. Okunishi, Y. Kondo, and Y. Ikuhara. Dynamics of Annular Bright Field Imaging in Scanning Transmission Electron Microscopy. *Ultramicroscopy*, 110(7):903–923, 2010.
- [41] Marcus Gallagher-jones, Colin Ophus, Karen C Bustillo, David R Boyer, Ouliana Panova, Calina Glynn, Chih-te Zee, Jim Ciston, Kevin Canton Mancia, Andrew M Minor, and Jose A Rodriguez. Nanoscale Mosaicity Revealed in Peptide Microcrystals by Scanning Electron Nanodiffraction. *Communications Biology*, 2(26), 2019.
- [42] Jaume Gazquez, Weidong Luo, Mark P. Oxley, Micah Prange, Maria A. Torija, Manish Sharma, Chris Leighton, Sokrates T. Pantelides, Stephen J. Pennycook, and Maria Varela. Atomic-Resolution Imaging of Spin-State Superlattices in Nanopockets within Cobaltite Thin Films. *Nano Letters*, 11(3):973–976, 2011.
- [43] A. M. Glazer. The Classification of Tilted Octahedra in Perovskites. *Acta Crystallographica Section B*, 28(11):3384–3392, 1972.
- [44] A. M. Glazer. Simple Ways of Determining Perovskite Structures. *Acta Crystallographica Section A*, 31(6):756–762, 1975.
- [45] J.M. Gonzalez-Calbet, M.J. Sayagues, and M. Vallet-Regi. An Electron Diffraction Study of New Phases in the LaNiO_{3-x} System. *Solid State Ionics*, 32-33:721–726, 1989.
- [46] Berit H. Goodge. *Advances in Scanning Transmission Electron Microscopy for*

Materials Discovery an Innovation. PhD thesis, Cornell University, Ithaca, NY, 2020.

- [47] Berit H. Goodge, Elisabeth Bianco, Noah Schnitzer, Henny W. Zandbergen, and Lena F. Kourkoutis. Atomic-Resolution Cryo-STEM Across Continuously Variable Temperatures. *Microscopy and Microanalysis*, 26(3):439–446, 2020.
- [48] Berit H. Goodge, Danfeng Li, Kyuho Lee, Motoki Osada, Bai Yang Wang, George A. Sawatzky, Harold Y. Hwang, and Lena F. Kourkoutis. Doping Evolution of the Mott-Hubbard Landscape in Infinite-Layer Nickelates. *Proceedings of the National Academy of Sciences*, 118(2), 2021.
- [49] P. Goodman and A. F. Moodie. Numerical Evaluations of N -Beam Wave Functions in Electron Scattering by the Multi-Slice Method. *Acta Crystallographica Section A*, 30(2):280–290, 1974.
- [50] R. J. Green, M. W. Haverkort, and G. A. Sawatzky. Bond Disproportionation and Dynamical Charge Fluctuations in the Perovskite Rare-Earth Nickelates. *Physical Review B*, 94(19):1–5, 2016.
- [51] Xiangxiang Guan, Xi Shen, Weipeng Wang, Wei Wang, Qianqian Lan, Jing Zhang, Jine Zhang, Huaiwen Yang, Yuan Yao, Junjie Li, Changzhi Gu, Jirong Sun, and Richeng Yu. Two Kinds of Metastable Structures in an Epitaxial Lanthanum Cobalt Oxide Thin Film. *Inorganic Chemistry*, 58(19):13440–13445, 2019.
- [52] Hangwen Guo, Mohammad Saghayezhian, Zhen Wang, Yimei Zhu, Jiandi Zhang, and Ward Plummer. Visualizing Quantum Phenomena at Complex Oxide Interfaces: An Atomic View from Scanning Transmission Electron Microscopy. *Frontiers of Physics*, 15(1), 2020.
- [53] Jordan A. Hachtel, Jingsong Huang, Ilja Popovs, Santa Jansone-Popova, Jong K. Keum, Jacek Jakowski, Tracy C. Lovejoy, Niklas Dellby, Ondrej L. Krivanek, and Juan Carlos Idrobo. Identification of Site-Specific Isotopic Labels by Vibrational Spectroscopy in the Electron Microscope. *Science*, 363(6426):525–528, 2019.
- [54] Jordan A. Hachtel, Juan Carlos Idrobo, and Miaofang Chi. Sub-Ångstrom Electric Field Measurements on a Universal Detector in a Scanning Transmission Electron Microscope. *Advanced Structural and Chemical Imaging*, 4(1), 2018.

- [55] Fredrik S Hage, Rebecca J Nicholls, Jonathan R Yates, Dougal G Mcculloch, Tracy C Lovejoy, Niklas Dellby, Ondrej L Krivanek, Keith Refson, and Quentin M Ramasse. Nanoscale Momentum-Resolved Vibrational Spectroscopy. *Science Advances*, 4:1–7, 2018.
- [56] J. E. Han, O. Gunnarsson, and V. H. Crespi. Strong Superconductivity with Local Jahn-Teller Phonons in C_{60} Solids. *Physical Review Letters*, 90(16):4, 2003.
- [57] Yimo Han, Kayla Nguyen, Michael Cao, Paul Cueva, Saien Xie, Mark W. Tate, Prafull Purohit, Sol M. Gruner, Jiwoong Park, and David A. Muller. Strain Mapping of Two-Dimensional Heterostructures with Subpicometer Precision. *Nano Letters*, 18(6):3746–3751, 2018.
- [58] Frederik Hetsch, Ni Zhao, Stephen V. Kershaw, and Andrey L. Rogach. Quantum Dot Field Effect Transistors. *Materials Today*, 16(9):312–325, 2013.
- [59] M Hidaka, K Inoue, I Yamada, and P J Walker. X-Ray Diffraction Study of the Crystal Structures of K_2CuF_4 and $K_2Cu_xZn_{1-x}F_4$. *Physica B+C*, 121(3):343–350, 1983.
- [60] S. Hillyard and J. Silcox. Detector Geometry, Thermal Diffuse Scattering and Strain Effects in ADF STEM Imaging. *Ultramicroscopy*, 58:6–17, 1995.
- [61] Goro Honjo, Norihisa Kitamura, Kohji Shimaoka, and Kazuhiro Mihama. Low Temperature Specimen Method for Electron Diffraction and Electron Microscopy. *Journal of the Physical Society of Japan*, 11(5):527–536, 1956.
- [62] Robert Hovden and David A. Muller. Efficient Elastic Imaging of Single Atoms on Ultrathin Supports in a Scanning Transmission Electron Microscope. *Ultramicroscopy*, 123:59–65, 2012.
- [63] Robert Hovden, Huolin L. Xin, and David A. Muller. Channeling of a Sub-angstrom Electron Beam in a Crystal Mapped to Two-Dimensional Molecular Orbitals. *Physical Review B - Condensed Matter and Materials Physics*, 86(19):1–7, 2012.
- [64] Chen Hu, Alban Gassenq, Yolanda Justo, Kilian Devloo-Casier, Hongtao Chen, Christophe Detavernier, Zeger Hens, and Günther Roelkens. Air-Stable Short-Wave Infrared PbS Colloidal Quantum Dot Photoconductors Passivated with Al_2O_3 Atomic Layer Deposition. *Applied Physics Letters*, 105(17):171110, 2014.

- [65] M. J. Hÿtch, E. Snoeck, and R. Kilaas. Quantitative Measurement of Displacement and Strain Fields from HREM Micrographs. *Ultramicroscopy*, 74(3):131–146, 1998.
- [66] Soohyun Im, Zhen Chen, Jared M. Johnson, Pengyang Zhao, Geun Hee Yoo, Eun Soo Park, Yunzhi Wang, David A. Muller, and Jinwoo Hwang. Direct Determination of Structural Heterogeneity in Metallic Glasses using Four-Dimensional Scanning Transmission Electron Microscopy. *Ultramicroscopy*, 195(September):189–193, 2018.
- [67] Steve Johnston, Anamitra Mukherjee, Ilya Elfimov, Mona Berciu, and George A. Sawatzky. Charge Disproportionation without Charge Transfer in the Rare-Earth-Element Nickelates as a Possible Mechanism for the Metal-Insulator Transition. *Physical Review Letters*, 112(10):1–5, 2014.
- [68] E. Kalesaki, C. Delerue, C. Morais Smith, W. Beugeling, G. Allan, and D. Vanmaekelbergh. Dirac Cones, Topological Edge States, and Nontrivial Flat Bands in Two-Dimensional Semiconductors with a Honeycomb Nanogeometry. *Physical Review X*, 4(1):011010, 2014.
- [69] E. Kalesaki, W. H. Evers, G. Allan, D. Vanmaekelbergh, and C. Delerue. Electronic Structure of Atomically Coherent Square Semiconductor Superlattices with Dimensionality Below Two. *Physical Review B - Condensed Matter and Materials Physics*, 88(11):115431, 2013.
- [70] Tsukasa Katayama, Akira Chikamatsu, Hideyuki Kamisaka, Yuichi Yokoyama, Yasuyuki Hirata, Hiroki Wadati, Tomoteru Fukumura, and Tetsuya Hasegawa. Topotactic Synthesis of Strontium Cobalt Oxyhydride Thin Film with Perovskite Structure. *AIP Advances*, 5(10), 2015.
- [71] V. J. Keast, A. J. Scott, R. Brydson, D. B. Williams, and J. Bruley. Electron Energy-Loss Near-Edge Structure - A Tool for the Investigation of Electronic Structure on the Nanometre Scale. *Journal of Microscopy*, 203(2):135–175, 2001.
- [72] Woo Jin Kim, Michelle A. Smeaton, Chunjing Jia, Berit H. Goodge, Byoung-Gwan Cho, Kyuho Lee, Motoki Osada, Daniel Jost, Anton V. Ievlev, Brian Moritz, Lena F. Kourkoutis, Thomas P. Devereaux, and Harold Y. Hwang. Geometric Frustration of Jahn-Teller Order and Ice Rules in the Infinite-Layer Lattice. *Preprint from Research Square*, 2022.
- [73] Koji Kimoto and Kazuo Ishizuka. Spatially Resolved Diffractometry with Atomic-Column Resolution. *Ultramicroscopy*, 111(8):1111–1116, 2011.

- [74] Earl J. Kirkland. *Advanced Computing in Electron Microscopy*. Springer Nature Switzerland, 3rd edition, 2020.
- [75] Earl J. Kirkland, Russell F. Loane, and John Silcox. Simulation of Annular Dark Field STEM Images using a Modified Multislice Method. *Ultramicroscopy*, 23(1):77–96, 1987.
- [76] L. Fitting Kourkoutis, M. K. Parker, V. Vaithyanathan, D. G. Schlom, and D. A. Muller. Direct Measurement of Electron Channeling in a Crystal using Scanning Transmission Electron Microscopy. *Physical Review B - Condensed Matter and Materials Physics*, 84(7):1–7, 2011.
- [77] Lena F. Kourkoutis. *Atomic-Scale Studies Of Structure And Bonding At Perovskite Oxide Heterointerfaces*. PhD thesis, Cornell University, Ithaca, NY, 2009.
- [78] Ondrej L. Krivanek, Matthew F. Chisholm, Valeria Nicolosi, Timothy J. Pennycook, George J. Corbin, Niklas Dellby, Matthew F. Murfitt, Christopher S. Own, Zoltan S. Szilagy, Mark P. Oxley, Sokrates T. Pantelides, and Stephen J. Pennycook. Atom-by-Atom Structural and Chemical Analysis by Annular Dark-Field Electron Microscopy. *Nature*, 464(7288):571–574, 2010.
- [79] Hiroki Kurata and Christian Colliex. Electron-Energy-Loss Core-Edge Structures in Manganese Oxides. *Physical Review B*, 48(4):2102–2108, 1993.
- [80] James M. Lebeau, Scott D. Findlay, Xiqu Wang, Allan J. Jacobson, Leslie J. Allen, and Susanne Stemmer. High-Angle Scattering of Fast Electrons from Crystals Containing Heavy Elements: Simulation and Experiment. *Physical Review B - Condensed Matter and Materials Physics*, 79(21):2–7, 2009.
- [81] Kyuho Lee, Berit H. Goodge, Danfeng Li, Motoki Osada, Bai Yang Wang, Yi Cui, Lena F. Kourkoutis, and Harold Y. Hwang. Aspects of the Synthesis of Thin Film Superconducting Infinite-Layer Nickelates. *APL Materials*, 8(4), 2020.
- [82] Sungbin Lee, Ru Chen, and Leon Balents. Metal-Insulator Transition in a Two-Band Model for the Perovskite Nickelates. *Physical Review B - Condensed Matter and Materials Physics*, 84(16):1–18, 2011.
- [83] Bing Li, Despina Louca, Shinichiro Yano, Luke G. Marshall, Jianshi Zhou, and John B. Goodenough. Insulating Pockets in Metallic LaNiO₃. *Advanced Electronic Materials*, 2(2):1–5, 2016.

- [84] Danfeng Li, Kyuho Lee, Bai Yang Wang, Motoki Osada, Samuel Crossley, Hye Ryoung Lee, Yi Cui, Yasuyuki Hikita, and Harold Y. Hwang. Superconductivity in an Infinite-Layer Nickelate. *Nature*, 572(7771):624–627, 2019.
- [85] Danfeng Li, Bai Yang Wang, Kyuho Lee, Shannon P. Harvey, Motoki Osada, Berit H. Goodge, Lena F. Kourkoutis, and Harold Y. Hwang. Superconducting Dome in $\text{Nd}_{1-x}\text{Sr}_x\text{NiO}_2$ Infinite Layer Films. *Physical Review Letters*, 125(2):1–6, 2020.
- [86] Xiang Li, Hao Wang, Zhiming Cui, Yutao Li, Sen Xin, Jianshi Zhou, Youwen Long, Changqing Jin, and John B. Goodenough. Exceptional Oxygen Evolution Reactivities on CaCoO_3 and SrCoO_3 . *Science Advances*, 5(8):3–10, 2019.
- [87] Zhenglu Li, Ting Cao, Meng Wu, and Steven G. Louie. Generation of Anisotropic Massless Dirac Fermions and Asymmetric Klein Tunneling in Few-Layer Black Phosphorus Superlattices. *Nano Letters*, 17(4):2280–2286, 2017.
- [88] Yao Liu, Jason Tolentino, Markelle Gibbs, Rachelle Ihly, Craig L. Perkins, Yu Liu, Nathan Crawford, John C. Hemminger, and Matt Law. PbSe Quantum Dot Field-Effect Transistors with Air-Stable Electron Mobilities Above $7 \text{ cm}^2\text{V}^{-1}\text{s}^{-1}$. *Nano Letters*, 13(4):1578–1587, 2013.
- [89] R. F. Loane, E. J. Kirkland, and J. Silcox. Visibility of Single Heavy Atoms on Thin Crystalline Silicon in Simulated Annular Dark-Field STEM Images. *Acta Crystallographica Section A*, 44(6):912–927, 1988.
- [90] R. F. Loane, P. Xu, and J. Silcox. Thermal Vibrations in Convergent-Beam Electron Diffraction. *Acta Crystallographica Section A*, 47(3):267–278, 1991.
- [91] Juan G. Lozano, Gerardo T. Martinez, Liyu Jin, Peter D. Nellist, and Peter G. Bruce. Low-Dose Aberration-Free Imaging of Li-Rich Cathode Materials at Various States of Charge Using Electron Ptychography. *Nano Letters*, 18(11):6850–6855, 2018.
- [92] Ian MacLaren and Quentin M. Ramasse. Aberration-Corrected Scanning Transmission Electron Microscopy for Atomic-Resolution Studies of Functional Oxides. *International Materials Reviews*, 59(3):115–131, 2014.
- [93] Arthur R. C. Mccray, Benjamin H. Savitzky, Kevin Whitham, and Lena F.

- Kourkoutis. Orientational Disorder in Epitaxially Connected Quantum Dot Solids. *ACS Nano*, 13:11460–11468, 2019.
- [94] M. Medarde, M. T. Fernández-Díaz, and Ph Lacorre. Long-Range Charge Order in the Low-Temperature Insulating Phase of PrNiO₃. *Physical Review B - Condensed Matter and Materials Physics*, 78(21):2–5, 2008.
- [95] María Luisa Medarde. Structural, Magnetic and Electronic Properties of RNiO₃ Perovskites (R = Rare Earth). *Journal of Physics Condensed Matter*, 9(8):1679–1707, 1997.
- [96] Anna Clare Milazzo, Philippe Leblanc, Fred Duttweiler, Liang Jin, James C. Bouwer, Steve Peltier, Mark Ellisman, Fred Bieser, Howard S. Matis, Howard Wieman, Peter Denes, Stuart Kleinfelder, and Nguyen Huu Xuong. Active Pixel Sensor Array as a Detector for Electron Microscopy. *Ultramicroscopy*, 104(2):152–159, 2005.
- [97] Andrew M. Minor, Peter Denes, and David A. Muller. Cryogenic Electron Microscopy for Quantum Science. *MRS Bulletin*, 44(12):961–966, 2019.
- [98] T. Mizokawa, D. Khomskii, and G. Sawatzky. Spin and Charge Ordering in Self-Doped Mott Insulators. *Physical Review B - Condensed Matter and Materials Physics*, 61(17):11263–11266, 2000.
- [99] Kalani Moore, Ursel Bangert, and Michele Conroy. Aberration Corrected STEM Techniques to Investigate Polarization in Ferroelectric Domain Walls and Vortices. *APL Materials*, 9(2), 2021.
- [100] Toshihiro Moriga, Osamu Usaka, Tomomi Imamura, Ichiro Nakabayashi, Ichiro Matsubara, Tsuneo Kinouchi, Shinichi Kikkawa, and Fumikazu Kanamaru. Synthesis, Crystal Structure, and Properties of Oxygen-Deficient Lanthanum Nickelate LaNiO_{3-x} (0 ≤ x ≤ 0.5). *Chemical Society of Japan*, 67:687–693, 1994.
- [101] Ali Mostaed, Geetha Balakrishnan, Martin Richard Lees, Yukio Yasui, Lih Jeng Chang, and Richard Beanland. Atomic Structure Study of the Pyrochlore Yb₂Ti₂O₇ and its Relationship with Low-Temperature Magnetic Order. *Physical Review B - Condensed Matter and Materials Physics*, 95(9):094431, 2017.
- [102] Ali Mostaed, Brant Walkley, Monica Ciomaga Hatnean, Geetha Balakrishnan, Martin R. Lees, Richard Beanland, Derek C. Sinclair, and Ian M.

- Reaney. Characterizing Oxygen Atoms in Perovskite and Pyrochlore Oxides using ADF-STEM at a Resolution of a Few Tens of Picometers. *Acta Materialia*, 208:116717, 2021.
- [103] David A. Muller, Byard Edwards, Earl J. Kirkland E, and John Silcox. Simulation of Thermal Diffuse Scattering Including a Detailed Phonon Dispersion Curve. *Ultramicroscopy*, 86(3-4):371–380, 2001.
- [104] David A. Muller and John Silcox. Delocalization in Inelastic Scattering. *Ultramicroscopy*, 59:195–213, 1995.
- [105] David A. Muller, Yujiun Tzou, Rishi Raj, and John Silcox. Mapping sp^2 and sp^3 States of Carbon at Sub-Nanometre Spatial Resolution. *Nature*, 366:725–727, 1993.
- [106] Julia A. Mundy, Yasuyuki Hikita, Takeaki Hidaka, Takeaki Yajima, Takuya Higuchi, Harold Y. Hwang, David A. Muller, and Lena F. Kourkoutis. Visualizing the Interfacial Evolution from Charge Compensation to Metallic Screening Across the Manganite Metal-Insulator Transition. *Nature Communications*, 5:3–8, 2014.
- [107] P. D. Nellist, M. F. Chisholm, N. Dellby, O. L. Krivanek, M. F. Murfitt, Z. S. Szilagy, A. R. Lupini, A. Borisevich, W. H. Sides, and S. J. Pennycook. Direct Sub-Angstrom Imaging of a Crystal Lattice. *Science*, 305(5691):1741, 2004.
- [108] Myoung Hwan Oh, Min Gee Cho, Dong Young Chung, Inchul Park, Youngwook Paul Kwon, Colin Ophus, Dokyoon Kim, Min Gyu Kim, Beomgyun Jeong, X. Wendy Gu, Jinwoung Jo, Ji Mun Yoo, Jaeyoung Hong, Sara McMains, Kisuk Kang, Yung Eun Sung, A. Paul Alivisatos, and Taeghwan Hyeon. Design and Synthesis of Multigrain Nanocrystals via Geometric Misfit Strain. *Nature*, 577(7790):359–363, 2020.
- [109] Soong Ju Oh, Nathaniel E. Berry, Ji Hyuk Choi, E. Ashley Gauling, Hangfei Lin, Taejong Paik, Benjamin T. Diroll, Shin Muramoto, Christopher B. Murray, and Cherie R. Kagan. Designing High-Performance PbS and PbSe Nanocrystal Electronic Devices through Stepwise, Post-Synthesis, Colloidal Atomic Layer Deposition. *Nano Letters*, 14(3):1559–1566, 2014.
- [110] Eiji Okunishi, Hidetaka Sawada, and Yukihiro Kondo. Experimental Study of Annular Bright Field (ABF) Imaging using Aberration-Corrected

- Scanning Transmission Electron Microscopy (STEM). *Micron*, 43(4):538–544, 2012.
- [111] M. J. Olszta, J. Wang, and E. C. Dickey. Stoichiometry and Valence Measurements of Niobium Oxides Using Electron Energy-Loss Spectroscopy. *Journal of Microscopy*, 224(3):233–241, 2006.
- [112] Justin C. Ondry, Matthew R. Hauwiler, and A. Paul Alivisatos. Dynamics and Removal Pathway of Edge Dislocations in Imperfectly Attached PbTe Nanocrystal Pairs: Towards Design Rules for Oriented Attachment. *ACS Nano*, 12:3178–3189, 2018.
- [113] Justin C. Ondry, John P. Philbin, Michael Lostica, Eran Rabani, and A. Paul Alivisatos. Resilient Pathways to Atomic Attachment of Quantum Dot Dimers and Artificial Solids from Faceted CdSe Quantum Dot Building Blocks. *ACS Nano*, 13:12322–12344, 2019.
- [114] Colin Ophus. Four-Dimensional Scanning Transmission Electron Microscopy (4D-STEM): From Scanning Nanodiffraction to Ptychography and Beyond. *Microscopy and Microanalysis*, pages 563–582, 2019.
- [115] Motoki Osada, Bai Yang Wang, Berit H. Goodge, Kyuho Lee, Hyeok Yoon, Keita Sakuma, Danfeng Li, Masashi Miura, Lena F. Kourkoutis, and Harold Y. Hwang. A Superconducting Praseodymium Nickelate with Infinite Layer Structure. *Nano letters*, 20(8):5735–5740, 2020.
- [116] Elliot Padgett, Megan E. Holtz, Paul Cueva, Yu Tsun Shao, Eric Langenberg, Darrell G. Schlom, and David A. Muller. The Exit-Wave Power-Cepstrum Transform for Scanning Nanobeam Electron Diffraction: Robust Strain Mapping at Subnanometer Resolution and Subpicometer Precision. *Ultramicroscopy*, 214, 2020.
- [117] Cheol-Hwan Park and Steven G. Louie. Making Massless Dirac Fermions from a Patterned Two-Dimensional Electron Gas. *Nano Letters*, 9(5):1793–1797, 2009.
- [118] Hyowon Park, Andrew J. Millis, and Chris A. Marianetti. Site-Selective Mott Transition in Rare-Earth-Element Nickelates. *Physical Review Letters*, 109(15):1–5, 2012.
- [119] rpd Pasztor, Alessandro Scarfato, Marcello Spera, Celine Barreteau, Enrico Giannini, and Christoph Renner. Holographic Imaging of the Com-

- plex Charge Density Wave Order Parameter. *Phys. Rev. Research*, 1:033114, 2019.
- [120] D H Pearson, C C Ahn, and B Fultz. White Lines and d -Electron Occupancies for the $3d$ and $4d$ Transition Metals. *Physical Review B*, 47(14):8471–8478, 1993.
- [121] Timothy J. Pennycook, Andrew R. Lupini, Hao Yang, Matthew F. Murfitt, Lewys Jones, and Peter D. Nellist. Efficient Phase Contrast Imaging in STEM using a Pixelated Detector. Part 1: Experimental Demonstration at Atomic Resolution. *Ultramicroscopy*, 151:160–167, 2015.
- [122] Joep L. Peters, Thomas Altantzis, Ivan Lobato, Maryam Alimoradi Jazi, Carlo Van Overbeek, Sara Bals, Daniel Vanmaekelbergh, and Sophia Buhbut Sinai. Mono- and Multilayer Silicene-Type Honeycomb Lattices by Oriented Attachment of PbSe Nanocrystals: Synthesis, Structural Characterization, and Analysis of the Disorder. *Chemistry of Materials*, 30(14):4831–4837, 2018.
- [123] G. Radtke, S. Lazar, and G. A. Botton. High-Resolution EELS Investigation of the Electronic Structure of Ilmenites. *Physical Review B - Condensed Matter and Materials Physics*, 74(15):155117, 2006.
- [124] B. Raveau, M. Hervieu, A. Maignan, and C. Martin. The Route to CMR Manganites: What About Charge Ordering and Phase Separation? *Journal of Materials Chemistry*, 11(1):29–36, 2001.
- [125] Zhenwei Ren, Jiankun Sun, Hui Li, Peng Mao, Yuanzhi Wei, Xinhua Zhong, Jinsong Hu, Shiyong Yang, and Jizheng Wang. Bilayer PbS Quantum Dots for High-Performance Photodetectors. *Advanced Materials*, 29(33):1702055, 2017.
- [126] Peter Rez and David A. Muller. The Theory and Interpretation of Electron Energy Loss Near-Edge Fine Structure. *Annual Review of Materials Research*, 38:535–558, 2008.
- [127] T. Riedl, T. Gemming, and K. Wetzig. Extraction of EELS White-Line Intensities of Manganese Compounds: Methods, Accuracy, and Valence Sensitivity. *Ultramicroscopy*, 106(4-5):284–291, 2006.
- [128] R. D. Sánchez, M. T. Causa, A. Caneiro, A. Butera, M. Vallet-Regí, M. J. Sayagués, J. González-Calbet, F. García-Sanz, and J. Rivas. Metal-

Insulator Transition in Oxygen-Deficient LaNiO_{3-x} Perovskites. *Physical Review B*, 54(23):574–578, 1996.

- [129] C. S. Suchand Sandeep, Jon Mikel Azpiroz, Wiel H. Evers, Simon C. Boehme, Iwan Moreels, Sachin Kinge, Laurens D.A. Siebbeles, Ivan Infante, and Arjan J. Houtepen. Epitaxially Connected PbSe Quantum-Dot Films: Controlled Neck Formation and Optoelectronic Properties. *ACS Nano*, 8(11):11499–11511, 2014.
- [130] Rinku Saran and Richard J. Curry. Lead Sulphide Nanocrystal Photodetector Technologies. *Nature Photonics*, 10(2):81–92, 2016.
- [131] Benjamin H. Savitzky. *Computational Analysis of Order and Disorder at the Picometer to Micron Scale in Selected Scanning Transmission Electron Microscopy Studies*. PhD thesis, Cornell University, Ithaca, NY, 2018.
- [132] Benjamin H. Savitzky, Ismail El Baggari, Alemayehu S. Admasu, Jaewook Kim, Sang Wook Cheong, Robert Hovden, and Lena F. Kourkoutis. Bending and Breaking of Stripes in a Charge Ordered Manganite. *Nature Communications*, 8(1):1–6, 2017.
- [133] Benjamin H. Savitzky, Ismail El Baggari, Colin B. Clement, Emily Waite, Berit H. Goodge, David J. Baek, John P. Sheckelton, Christopher Pasco, Hari Nair, Nathaniel J. Schreiber, Jason Hoffman, Alemayehu S. Admasu, Jaewook Kim, Sang Wook Cheong, Anand Bhattacharya, Darrell G. Schlom, Tyrel M. McQueen, Robert Hovden, and Lena F. Kourkoutis. Image Registration of Low Signal-to-Noise Cryo-STEM Data. *Ultramicroscopy*, 191:56–65, 2018.
- [134] Benjamin H. Savitzky, Robert Hovden, Kevin Whitham, Jun Yang, Frank Wise, Tobias Hanrath, and Lena F. Kourkoutis. Propagation of Structural Disorder in Epitaxially Connected Quantum Dot Solids from Atomic to Micron Scale. *Nano Letters*, 16(9):5714–5718, 2016.
- [135] Benjamin H. Savitzky, Steven E. Zeltmann, Lauren A. Hughes, Hamish G. Brown, Shiteng Zhao, Philipp M. Pelz, Thomas C. Pekin, Edward S. Barnard, Jennifer Donohue, Luis Rangel Dacosta, Ellis Kennedy, Yujun Xie, Matthew T. Janish, Matthew M. Schneider, Patrick Herring, Chirranjeevi Gopal, Abraham Anapolsky, Rohan Dhall, Karen C. Bustillo, Peter Ercius, Mary C. Scott, Jim Ciston, Andrew M. Minor, and Colin Ophus. Py4DSTEM: A Software Package for Four-Dimensional Scanning Transmission Electron Microscopy Data Analysis. *Microscopy and Microanalysis*, 27(4):712–743, 2021.

- [136] Alpesh Khushalchand Shukla, Quentin M. Ramasse, Colin Ophus, Despoina Maria Kepaptsoglou, Fredrik S. Hage, Christoph Gammer, Charles Bowling, Pedro Alejandro Hernández Gallegos, and Subramanian Venkatachalam. Effect of Composition on the Structure of Lithium- and Manganese-Rich Transition Metal Oxides. *Energy and Environmental Science*, 11(4):830–840, 2018.
- [137] Michelle A. Smeaton, Ismail El Baggari, Daniel M. Balazs, Tobias Hanrath, and Lena F. Kourkoutis. Mapping Defect Relaxation in Quantum Dot Solids upon In Situ Heating. *ACS Nano*, 15(1):719–726, 2021.
- [138] John C.H. Spence. Absorption Spectroscopy with Sub-Angstrom Beams: ELS in STEM. *Reports on Progress in Physics*, 69(3):725–758, 2006.
- [139] Harold T Stokes, Dorian M Hatch, and Branton J Campbell. Isotropy software suite. iso.byu.edu.
- [140] Cedric Tassel, Jose Miguel Pruneda, Naoaki Hayashi, Takashi Watanabe, Atsushi Kitada, Yoshihiro Tsujimoto, Hiroshi Kageyama, Kazuyoshi Yoshimura, Mikio Takano, Masakazu Nishi, Kenji Ohoyama, Masaichiro Mizumaki, Naomi Kawamura, Jorge Iniguez, and Enric Canadell. CaFeO₂: A New Type of Layered Structure with Iron in a Distorted Square Planar Coordination. *Journal of the American Chemical Society*, 131:221–229, 2009.
- [141] Mark W. Tate, Prafull Purohit, Darol Chamberlain, Kayla X. Nguyen, Robert Hovden, Celesta S. Chang, Pratiti Deb, Emrah Turgut, John T. Heron, Darrell G. Schlom, Daniel C. Ralph, Gregory D. Fuchs, Katherine S. Shanks, Hugh T. Philipp, David A. Muller, and Sol M. Gruner. High Dynamic Range Pixel Array Detector for Scanning Transmission Electron Microscopy. *Microscopy and Microanalysis*, 22(1):237–249, 2016.
- [142] J. B. Torrance, P. Lacorre, A.I. Nazzal, E.J. Ansaldo, and Ch. Niedermayer. Systematic Study of Insulator-Metal Transitions in Perovskites RNiO₃ (R = Pr, Nd, Sm, Eu) Due to Closing of Charge-Transfer Gap. *Physical Review B*, 45(14):8209–8212, 1992.
- [143] Michael M.J. Treacy. Z Dependence of Electron Scattering by Single Atoms into Annular Dark-Field Detectors. *Microscopy and Microanalysis*, 17(6):847–858, 2011.
- [144] Y. Tsujimoto, C. Tassel, N. Hayashi, T. Watanabe, H. Kageyama, K. Yoshimura, M. Takano, M. Ceretti, C. Ritter, and W. Paulus. Infinite-

- Layer Iron Oxide with a Square-Planar Coordination. *Nature*, 450:1062–1065, 2007.
- [145] Marijn A. Van Huis, Lucas T. Kunneman, Karin Overgaag, Qiang Xu, Gregory Pandraud, Henny W. Zandbergen, and D. Vanmaekelbergh. Low-Temperature Nanocrystal Unification through Rotations and Relaxations Probed by in Situ Transmission Electron Microscopy. *Nano Letters*, 8:3959–3963, 2008.
- [146] Carlo Van Overbeek, Joep L. Peters, Susan A.P. Van Rossum, Marc Smits, Marijn A. Van Huis, and Daniel Vanmaekelbergh. Interfacial Self-Assembly and Oriented Attachment in the Family of PbX (X = S, Se, Te) Nanocrystals. *Journal of Physical Chemistry C*, 122(23):12464–12473, 2018.
- [147] Gustaaf Van Tendeloo, Sara Bals, Sandra Van Aert, Jo Verbeeck, and Dirk Van Dyck. Advanced Electron Microscopy for Advanced Materials. *Advanced Materials*, 24(42):5655–5675, 2012.
- [148] Julien Varignon, Mathieu N. Grisolia, Jorge Íñiguez, Agnès Barthélémy, and Manuel Bibes. Complete Phase Diagram of Rare-Earth Nickelates from First-Principles. *npj Quantum Materials*, 2(1):1–9, 2017.
- [149] Kartik Venkatraman, Peter Rez, Katia March, and Peter A. Crozier. The Influence of Surfaces and Interfaces on High Spatial Resolution Vibrational EELS from SiO₂. *Microscopy*, 67(S1):i14–i23, 2018.
- [150] R. von Helmolt, J. Wecker, B. Holzapfel, L. Schultz, and K. Samwer. Giant Negative Magnetoresistance in Perovskitelike La_{2/3}Ba_{1/3}MnO Ferromagnetic Films. *Physical Review Letters*, 71(14):2331–2333, 1993.
- [151] P. M. Voyles, J. L. Grazul, and D. A. Muller. Imaging Individual Atoms Inside Crystals with ADF-STEM. *Ultramicroscopy*, 96(3-4):251–273, 2003.
- [152] Willem Walravens, Eduardo Solano, Filip Geenen, Jolien Dendooven, Oleg Gorobtsov, Athmane Tadjine, Nayyera Mahmoud, Patrick Peiwen Ding, Jacob P.C. Ruff, Andrej Singer, Gunther Roelkens, Christophe Delerue, Christophe Detavernier, and Zeger Hens. Setting Carriers Free: Healing Faulty Interfaces Promotes Delocalization and Transport in Nanocrystal Solids. *ACS Nano*, 13(11):12774–12786, 2019.
- [153] Bi Xia Wang, S. Rosenkranz, X. Rui, Junjie Zhang, F. Ye, H. Zheng, R. F. Klie, J. F. Mitchell, and D. Phelan. Antiferromagnetic Defect Structure in LaNiO_{3-δ} Single Crystals. *Physical Review Materials*, 2(6):1–7, 2018.

- [154] Peng Wang, Fucai Zhang, Si Gao, Mian Zhang, and Angus I. Kirkland. Electron Ptychographic Diffractive Imaging of Boron Atoms in LaB_6 Crystals. *Scientific Reports*, 7(1):1–8, 2017.
- [155] Z. L. Wang, J. S. Yin, and Y. D. Jiang. EELS Analysis of Cation Valence States and Oxygen Vacancies in Magnetic Oxides. *Micron*, 31(5):571–580, 2000.
- [156] Kevin Whitham, Jun Yang, Benjamin H. Savitzky, Lena F. Kourkoutis, Frank Wise, and Tobias Hanrath. Charge Transport and Localization in Atomically Coherent Quantum Dot Solids. *Nature Materials*, 15:557–563, 2016.
- [157] Ryan J. Wu, Anudha Mittal, Michael L. Odlyzko, and K. Andre Mkhoyan. Simplifying Electron Beam Channeling in Scanning Transmission Electron Microscopy (STEM). *Microscopy and Microanalysis*, 23(4):794–808, 2017.
- [158] Takafumi Yamamoto, Yoji Kobayashi, Naoaki Hayashi, Cedric Tassel, Takashi Saito, Shoji Yamanaka, Mikio Takano, Kenji Ohoyama, Yuichi Shimakawa, Kazuyoshi Yoshimura, and Hiroshi Kageyama. $(\text{Sr}_{1-x}\text{Ba}_x)\text{FeO}_{1-x}$ ($0.4 \leq x \leq 1$): A New Oxygen-Deficient Perovskite Structure. *Journal of the American Chemical Society*, 134:11444–11454, 2012.
- [159] Zhenyu Yang, James Z. Fan, Andrew H. Proppe, F. Pelayo García De Arquer, David Rossouw, Oleksandr Voznyy, Xinzheng Lan, Min Liu, Grant Walters, Rafael Quintero-Bermudez, Bin Sun, Sjoerd Hoogland, Gianluigi A. Botton, Shana O. Kelley, and Edward H. Sargent. Mixed-Quantum-Dot Solar Cells. *Nature Communications*, 8(1):1325, 2017.
- [160] Andrew B. Yankovich, Benjamin Berkels, W. Dahmen, P. Binev, S. I. Sanchez, S. A. Bradley, Ao Li, Izabela Szlufarska, and Paul M. Voyles. Picometre-Precision Analysis of Scanning Transmission Electron Microscopy Images of Platinum Nanocatalysts. *Nature Communications*, 5(4155):1–7, 2014.
- [161] Amirabbas Yousefi Amin, Niall A. Killilea, Mykhailo Sytnyk, Philipp Maisch, Ka Cheong Tam, Hans Joachim Egelhaaf, Stefan Langner, Tobias Stubhan, Christoph J. Brabec, Tobias Rejek, Marcus Halik, Katharina Poulsen, Jan Niehaus, Anton Köck, and Wolfgang Heiss. Fully Printed Infrared Photodetectors from PbS Nanocrystals with Perovskite Ligands. *ACS Nano*, 13(2):2389–2397, 2019.
- [162] Hwanhui Yun, Abhinav Prakash, Bharat Jalan, Jong Seok Jeong, and

- K. Andre Mkhoyan. STEM Beam Channeling in BaSnO₃/LaAlO₃ Perovskite Bilayers and Visualization of 2D Misfit Dislocation Network. *Ultramicroscopy*, 208:112863, 2020.
- [163] Michael J Zachman, Zhengyuan Tu, Snehashis Choudhury, Lynden A Archer, and Lena F Kourkoutis. Cryo-STEM Mapping of Solid-Liquid Interfaces and Dendrites in Lithium-Metal Batteries. *Nature*, 560:345–349, 2018.
- [164] Steven E. Zeltmann, Alexander Müller, Karen C. Bustillo, Benjamin Savitzky, Lauren Hughes, Andrew M. Minor, and Colin Ophus. Patterned Probes for High Precision 4D-STEM Bragg Measurements. *Ultramicroscopy*, 209:112890, 2020.
- [165] Shengwei Zeng, Chi Sin Tang, Xinmao Yin, Changjian Li, Mengsha Li, Zhen Huang, Junxiong Hu, Wei Liu, Ganesh Ji Omar, Hariom Jani, Zhi Shiuh Lim, Kun Han, Dongyang Wan, Ping Yang, Stephen John Penrycook, Andrew T.S. Wee, and Ariando Ariando. Phase Diagram and Superconducting Dome of Infinite-Layer Nd_{1-x}Sr_xNiO₂ Thin Films. *Physical Review Letters*, 125(14):147003, 2020.
- [166] Hongye Zhang, Zhanwei Liu, Huihui Wen, Huimin Xie, and Chao Liu. Subset Geometric Phase Analysis Method for Deformation Evaluation of HRTEM Images. *Ultramicroscopy*, 171:34–42, 2016.
- [167] Junjie Zhang, Hong Zheng, Yang Ren, and J. F. Mitchell. High-Pressure Floating-Zone Growth of Perovskite Nickelate LaNiO₃ Single Crystals. *Crystal Growth and Design*, 17(5):2730–2735, 2017.
- [168] Pei Zhang, Zhe Wang, J. H. Perepezko, and P. M. Voyles. Elastic and Inelastic Mean Free Paths of 200 keV Electrons in Metallic Glasses. *Ultramicroscopy*, 171:89–95, 2016.
- [169] Yuan Zhao, Theresa E. Feltes, John R. Regalbuto, Randall J. Meyer, and Robert F. Klie. In Situ Electron Energy Loss Spectroscopy Study of Metallic Co and Co Oxides. *Journal of Applied Physics*, 108(6), 2010.
- [170] Hong Zheng, Bi Xia Wang, D. Phelan, Junjie Zhang, Yang Ren, M. J. Krogstad, S. Rosenkranz, R. Osborn, and J. F. Mitchell. Oxygen Inhomogeneity and Reversibility in Single Crystal LaNiO_{3-δ}. *Crystals*, 10(557), 2020.

[171] Yimei Zhu. Cryogenic Electron Microscopy on Strongly Correlated Quantum Materials. *Accounts of Chemical Research*, 54(18):3518–3528, 2021.